AD-A161 136 EFFECTS OF MOUNTAIN RANGES ON MESOSCALE SYSTEMS 1/2
DEVELOPMENT(U) COLORADO STATE UNIV FORT COLLINS DEPT OF
ATMOSPHERIC SCIENCE E R REITER ET AL SEP 85
UNCLASSIFIED AFOSR-TR-85-0924 AFOSR-82-0162 F/G 4/2 NL

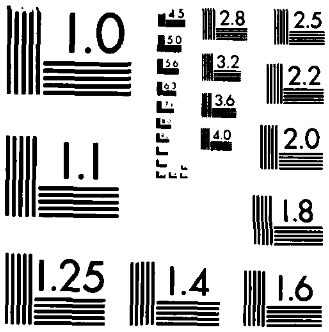

MICROCOPY RESOLUTION TEST CHART
NATIONAL BUREAU OF STANDARDS-1963-A

AFOSR-TR- 85-0924

(2)

AD-A161 136

EFFECTS OF MOUNTAIN RANGES ON MESOSCALE SYSTEMS DEVELOPMENT

Elmar R. Reiter, Principal Investigator

John D. Sheaffer, Co-Investigator

Marjorie A. Klitch and Ray L. McAnelly

UNCLASSIFIED
SECURITY CLASSIFICATION OF THIS PAGE

AD-A161 136

REPORT DOCUMENTATION PAGE

1a. REPORT SECURITY CLASSIFICATION

1b. RESTRICTIVE MARKINGS

2a. SECURITY CLASSIFICATION AUTHORITY UNCLASSIFIED

2b. DECLASSIFICATION/DOWNGRADING SCHEDULE

3. DISTRIBUTION/AVAILABILITY OF REPORT
Approved for public release;
Distribution unlimited

4. PERFORMING ORGANIZATION REPORT NUMBER(S)

5. MONITORING ORGANIZATION REPORT NUMBER(S) AFOSR-TR- 85-0924

6a. NAME OF PERFORMING ORGANIZATION Colorado State University

6b. OFFICE SYMBOL *(If applicable)*

7a. NAME OF MONITORING ORGANIZATION AFOSR

6c. ADDRESS *(City, State and ZIP Code)*
Department of Atmospheric Sciences
Fort Collins, CO 80523

7b. ADDRESS *(City, State and ZIP Code)*
Bldg 410
Bolling AFB, DC 20332-6448

8a. NAME OF FUNDING/SPONSORING ORGANIZATION AFOSR

8b. OFFICE SYMBOL *(If applicable)* NC

9. PROCUREMENT INSTRUMENT IDENTIFICATION NUMBER AFOSR-82-0162

8c. ADDRESS *(City, State and ZIP Code)*
Bldg 410
Bolling AFB, DC 20332-6448

10. SOURCE OF FUNDING NOS.

PROGRAM ELEMENT NO.	PROJECT NO.	TASK NO.	WORK UNIT NO.
61102F	2310	A1	

11. TITLE *(Include Security Classification)* Effects of Mountain Ranges on Mesoscale Systems Development

12. PERSONAL AUTHOR(S) Elmar R. Reiter, John D. Sheaffer, Marjorie A. Klitch and Ray L. McAnelly

13a. TYPE OF REPORT Final Report

13b. TIME COVERED FROM 4/15/82 TO 7/31/85

14. DATE OF REPORT *(Yr., Mo., Day)*

15. PAGE COUNT 191

16. SUPPLEMENTARY NOTATION

17. COSATI CODES

FIELD	GROUP	SUB. GR.

18. SUBJECT TERMS *(Continue on reverse if necessary and identify by block number)*

19. ABSTRACT *(Continue on reverse if necessary and identify by block number)*

Sufficiently large satellite and standard meteorological data banks have been assembled to determine the effects of mountain ranges on mesoscale systems development. Synoptic studies addressed themselves to a "moisture bridge" over Central America often tied to severe weather in the Rocky Mountain area. Heavy flooding events over eastern China have been tied to preferred positions of blocking highs and to vortices developing over the plateau of Tibet. (over

20. DISTRIBUTION/AVAILABILITY OF ABSTRACT
UNCLASSIFIED/UNLIMITED ☐ SAME AS RPT. ☐ DTIC USERS ☐

21. ABSTRACT SECURITY CLASSIFICATION

22a. NAME OF RESPONSIBLE INDIVIDUAL FRANCIS J. WODARCZYK

22b. TELEPHONE NUMBER *(Include Area Code)* 767-4963

22c. OFFICE SYMBOL NC

DD FORM 1473, 83 APR EDITION OF 1 JAN 73 IS OBSOLETE.

SECURITY CLASSIFICATION OF THIS PAGE

Mesoscale convective systems over and to the east of the U.S. Rocky Mountains have been investigated by individual case studies and satellite composite imagery. There appears to be a well-defined sequence of events, whereby first the average precipitation rate maximizes, then the volumetric rain rate, and finally the rain area. A synoptic climatology has been established for the North American summer and winter monsoon regimes and for the rainy season distributions over that continent. Diurnal circulation systems over the Rocky Mountains were studied for the summer monsoon regime only. Recent field measurements in tht context brought to light the existence of a nocturnal low-level jet stream over the western slopes of the Colorado Rockies. This jet appears only from wind measurements made on top of mountain peaks and cannot be detected from standard radiosonde data, nor from valley-based surface observations. Energy balance studies were carried out over Tibet and, by direct measurements under this project, in the Gobi Deser and at two locations in the Rocky Mountains. Results showed, that the atmospheric heat source is only about half as strong as previously believed, mainly due to a reduction in the surface drag coefficient. Numerical modeling efforts have yielded several very successful mesoscale versions, one with a 96-km grid, and a nested version with a 24-km grid. Both versions could predict vortex developments and heavy precipitation from convective systems over complex terrain rather adequately. The models have been constructed so that they can be run on an HP-9020 super-microcomputer. FINAL REPORT, AFOSR-82-0162, EFFECTS OF MOUNTAIN RANGES ON MERSOSCALE SYSTEMS DEVELOPMENT.

EFFECTS OF MOUNTAIN RANGES ON MESOSCALE SYSTEMS DEVELOPMENT

Final Scientific Report

15 April 1982 to 31 July 1985

Air Force Office of Scientific Research

Grant No. 82-0162

Elmar R. Reiter, Principal Investigator

John D. Sheaffer, Co-Investigator

Marjorie A. Klitch and Ray L. McAnelly

Department of Atmospheric Science

Colorado State University

Fort Collins, CO 80523

September 1985

Approved for public release,
distribution unlimited

EFFECTS OF MOUNTAIN RANGES ON MESOSCALE SYSTEMS DEVELOPMENT

Abstract

Sufficiently large satellite and standard meteorological data banks have been assembled to let us carry out the proposed research objectives. Synoptic studies addressed themselves to a "moisture bridge" over Central America which often is tied to severe weather in the Rocky Mountain area. Heavy flooding events over eastern China have been tied to preferred positions of blocking highs and to vortices developing over the Plateau of Tibet. Mesoscale convective systems over, and to the east of, the U.S. Rocky Mountains have been investigated by individual case studies as well as by satellite composite imagery. There appears to be a well-defined sequence of events, whereby first the average precipitation rate maximizes, then the volumetric rain rate, and finally the rain area.

A synoptic climatology has been established for the North American summer and winter monsoon regimes and for the rainy season distributions over that continent. Diurnal circulation systems over the Rocky Mountains were studied for the summer monsoon regime only. Recent field measurements in that context brought to light the existence of a nocturnal low-level jet stream over the western slopes of the Colorado Rockies. This jet appears only from wind measurements made on top of mountain peaks and cannot be detected from standard radiosonde data, nor from valley-based surface observations.

Energy balance studies were carried out over Tibet and, by direct measurements under this project, in the Gobi Desert and at two locations in the Rocky Mountains. Results showed, that the atmospheric heat

source is only about half as strong as previously believed, mainly due to a reduction in the surface drag coefficient. Such a reduction could be verified from our own measurements.

Numerical modeling efforts have yielded several very successful mesoscale versions, one with a 96-km grid and a nested version with a 24-km grid. Both versions could predict vortex developments and heavy precipitation from convective systems over complex terrain rather adequately. The models have been constructed so that they can be run on an HP-9020 super-microcomputer.

EFFECTS OF MOUNTAIN RANGES ON MESOSCALE SYSTEMS DEVELOPMENT

1. Research Objectives

In the original proposal document the following four research phases were identified:

(1) Assembly of the data bank for spring and summer of surface and upper air data for the region of the North American continent between 90°W and 115°W and 20°N and 50°N, and for regions of the Tibetan Plateau and its surroundings for as many years as feasible. Collection of satellite (IR and visible channel) data for appropriate time periods of concern will proceed at the same time.

(2) Synoptic studies of severe weather and heavy, extensive convective precipitation events.

(3) Establishment of a synoptic climatology of the atmospheric structure associated with the initiation and development of weather events including heavy, extensive convective rainfall over the two different regions.

(4) Development of numerical models to simulate the initiation and development of mesoscale convective complexes.

A fifth objective was added during the second grant year after a supplementary grant (No. AFOSR-82-0162A) was received to allow the acquisition of field instrumentation.

(5) Measurements of surface energy fluxes and heat budgets in complex terrain in the Rocky Mountains and in China, for the purpose of the improvement of parameterizations of such fluxes used in numerical models.

The following comprehensive report addresses itself briefly to each of these topic areas.

2. Data Bank Assembly

This was essentially completed by the end of the second grant year and a full status report is contained in our Annual Report of May 1984 (Reiter et al., 1984). These data, or at least subsets thereof, have been used extensively in our research. They are comprised of:

(1) The FGGE "Level II-b" (raw) data for the period April to September 1979.

(2) Nimbus 7 AVHRR data for the period May to August 1979.

(3) Forty years of monthly precipitation and air temperature data over the U.S.A.

(4) Thirty years of monthly snowfall data from 30 stations.

(5) NOAA/NESS northern hemisphere digitized snow and ice cover data on a weekly basis for the period 1966-1980.

(6) Global gridded (2.5 degree grid spacing) upper air data for the period May-August 1979.

(7) Enhancement visible and infrared GOES East and West Satellite images over North America, 1977 through 1982, hand-digitized for June to August 1981.

(8) GOES West PROFS data set (visible and IR), 5 image pairs per day, July, August 1982.

(9) Visible and IR images from Japanese Geostationary Meteorological Satellite, June of 1979 and July 1980 for the Tibetan region.

3. Synoptic Studies

(1) Moisture Bridge over Central America

From the inspection of satellite images and satellite film loops it became evident that quite often a "moisture bridge" of intense convective cloudiness extends from the Amazon Basin through Central America to the Rocky Mountains of Colorado. When this bridge is interrupted over Mexico, drought conditions appear to prevail there and the monsoon flow of moist air into the western United States also suffers. From film loops it appeared that, under moisture bridge conditions, the anvils of convective clouds traveled with a westerly flow in the upper troposphere throughout the length of this bridge, indicating the presence of an upper-level westerly wind regime at low latitudes of both hemispheres. Such conditions are conducive for the propagation of westerly Rossby wave perturbations from one to the other hemisphere (Reiter, 1983; Webster and Holton, 1982), a fact which is of concern to global weather forecasting.

From satellite data we obtained hints that perturbations, causing intensification of convective buildups, traveled in a meridional direction along this moisture bridge and were superimposed upon the dominant diurnal variation of cloudiness. There were also indications from surface wind and 850-mb data analyses, enhanced by surface temperature and pressure data (see Tang and Reiter, 1984), that the trade wind and sea breeze regimes in Central America are strongly affected by the convective activity over the Cordillera, possibly by feedback mechanisms involving the release of latent heat.

In order to substantiate these preliminary findings we expended considerable time and effort to obtain a suitable base of surface and upper-air data for Central America. However, we failed in this effort and had to abandon this line of research without publication of final results. We suggest, however, that a closer investigation of the circumstances under which this moisture bridge develops would be warranted because this bridge may have a considerable effect on severe weather over the western United States during summer monsoon conditions. Satellite data analyses by Klitch (Appendix A) also provide indications of the presence of such a bridge over Mexico. Field observations of winds at the top of Mt. Werner, Colorado (Reiter, Sheaffer and Smith, 1985), indicate the frequent appearance of a nighttime low-level jet stream, blowing from the south over the western slopes of the Rocky Mountains, which might be involved in the moisture transport suggested by the appearance of this bridge of convective cloudiness.

(2) Severe Weather Conditions over Eastern China

China and Taiwan frequently suffer from excessive rainfall leading to flooding catastrophes. Ding and Reiter (1982) compiled a calendar of the most excessive of these cases. The most severe events (1672 mm in 24 hours and 2749 mm in three days top the list) appear to be commonly associated with typhoon passages or landfalls. However, the passage of westerly vortices, many of them originating over the Plateau of Tibet, also plays a prominant role in flooding events along the main river systems of eastern China. The Meiyu season is known for heavy precipitation in the Yangzi valley. We have modelled successfully several cases of vortex development over Tibet, and associated heavy rainfall episodes along the eastern slopes of the Plateau, as will be described later. Ding and Reiter (1982) pointed out that large-scale circulation pattern anomalies, such as blocking highs over the Sea of Okhotsk and over Lake Baikal and a southward shift of westerlies, allowing synoptic perturbations to pass over the Tibetan Plateau, are conducive for prolonged and heavy rainfall over portions of eastern China. The impact of synoptic perturbations on the vortex development over Tibet suggested by Ding and Reiter was later confirmed by modeling studies carried out by Shen et al. (1985a).

Even though the circumstances leading to the formation of the Meiyu front and to severe weather development over eastern China are somewhat different from those over the United States to the east of the Rocky Mountains (East Asian weather is controlled by a more stable monsoon regime than weather over the western United States), the incorporation of Chinese data in our research work has led us to a much better understanding of some of the processes by which high plateaus and mountain ranges influence the development of severe weather patterns than could have been achieved by using exclusively North American data.

(3) Mesoscale Convective Systems Development East of the Rocky Mountains

Results from these studies, carried out by McAnelly, have not yet been published in the open literature. They are included as Appendix B, describing an investigation of the life cycle of Mesoscale Convective Complexes (MCCs)

a. Study of the August 1977 Episode

Investigation of a series of mesoscale convective complexes (MCCs) that recurred daily over the central United States throughout an eight day episode in August 1977 yielded a conceptual model of MCC evolution. The 1984 annual report (Reiter et al., 1984) discusses evolutionary characteristics, differences between mountain-originated ("western") and plains-originated ("eastern") systems, and common rainfall characteristics, which are briefly described below.

Pre-MCC convection is organized into discrete meso-β scale (20-200 km, <6 h) convective clusters which interact through confluence and mergers to produce intense MCC growth at the intersection of meso-α scale (200-2000 km, >6 h) discontinuities. Embedded within the unified meso-α anvil cloud during the mature phase, these meso-β clusters diverge upon decay of the MCC.

"Western" systems formed from north/south strings of convective clusters, enhanced by diurnally forced upslope flow, whereas "eastern" systems grew rapidly from only one or two vigorous meso-β clusters. "Eastern" systems were more stationary, tending to regenerate on the southwestern flank; "western" systems were driven eastward by the diurnally reversing plateau circulation and a west to east moisture gradient.

Precipitation rates were greatest early, during the intense growth phase of the MCC, and then steadily decreased. As precipitation rates decreased, the precipitation area increased, peaking one to two hours after the maximum MCC cloud shield area occured. Volumetric rain rates were greatest after the precipitation rate had begun to decrease, but before the precipitation area peaked. The intense early convection seems to force the development of an organized meso-α circulation within a few hours.

A more detailed discussion of the results of this research (supported in part by other funding) appears in Appendix B, a paper conditionally accepted by Monthly Weather Review (McAnelly and Cotton, 1985a), now under revision.

b. Composite Study of MCC Precipitation

Albeit enlightening, analyses of the August 1977 episode of MCCs may not be representative of MCCs that form under different synoptic conditions, or at different times during the convective season (McAnelly and Cotton, 1985a). Therefore, an objective analysis of seven years' digital hourly precipitation data was recently undertaken to derive more reliable MCC precipitation information that could improve forecasting, moisture and energy budget estimates, and numerical mesoscale model initialization and verification.

A brief description of the precipitation compositing analysis approach and preliminary results is included in Appendix C. The results confirm the conclusions drawn from the 1977 analysis: A well-defined sequence of maxima in average precipitation rate, then volumetric rain rate, then precipitating area correlates well with the satellite defined life cycle of MCCs. The results of this ongoing analysis will be presented at the Sixth Hydrometeorological Conference in Indianapolis in October 1985; a preprint of this conference paper (McAnelly and Cotton, 1985b) is included as Appendix D.

c. Composite Upper Air Study of MCCs

A compositing approach, similar to that taken with the precipitation study above, has recently been applied to upper air data using the data analysis/assimilation package of CSUs Regional Atmospheric Modeling System (RAMS)(Cotton et al. 1984) developed under separate funding. This study, outlined in Appendix C, improves on the composite MCC research pioneered by Maddox (1983) which defined a coarse life cycle: the genesis stage, the mature but decaying stage, and the conditions remaining the following day. Although valuable insights arose from that study, the 12-hour rawinsonde network could not adequately resolve the life cycle from so few systems.

Compositing synoptic observations for a large number of MCCs allowed better temporal resolution of the MCC life cycle. A high amplitude mesoscale anticyclone in the upper troposphere, identified by Maddox (1983) at his decaying mature stage, was shown in this analysis to evolve coherently to its maximum intensity at that stage. The vorticity tendency in the low to middle troposphere was reversed in sign (cyclonic tendency) and smaller in magnitude than in the upper troposphere. Moreover, the cyclonic vorticity maximum appeared earlier in the life cycle at lower tropospheric levels, than at progressively higher levels with time up through the middle troposphere.

Similar trends were reflected in the divergence tendencies at all levels. For instance, a convergence maximum developed early in the lower troposphere and progresses coherently upward through the middle troposphere after the MCC maximum size. This progression probably demonstrates the transformation from a convectively forced system driven by buoyant energy released from the boundary layer to a meso-α scale system driven by a deep layer of low- to midlevel convergence which sustains the large lightly precipitating anvil.

The results from the upper air and precipitation compositing studies of MCCs discussed in Sections 3.3 b and c are preliminary and in part supported by funding from another ongoing research project. The upper air MCC compositing study is part of Ming-Sen ("Jack") Lin's Ph.D. dissertation research. Once completed, the MCC precipitation compositing study (by Ray McAnelly) should appear as a refereed journal article.

4. Synoptic Climatology of Severe Weather Events

(1) Monsoons of the Northern Hemisphere

Tang and Reiter (1984) published a comprehensive study of the effects of the Tibetan Plateau and the Western Plateau of North America on the development of summer and winter monsoon systems over both regions. Although there are marked similarities between both systems, the dissimilarities have been stressed in their report as well. The contrast between an ocean or a continent being located upwind of the plateau region, as well as the shape of the orographic barrier are responsible for most of these differences. By using surface pressure and temperature data to enhance the 850-mb geopotential height field over the Rocky Mountains Tang and Reiter were able to show the existence of several quasi-permanent features in the monsoon-related atmospheric structure. As Reiter (1982) has shown, such features tend to be correlated with topographic details. The heat low over the Mojave Desert appears prominently at 850 mb during most of the year. Unfortunately, with the present radiosonde network this heat low is poorly defined. This fact makes it difficult to resolve some of the moisture and pollution transport processes from the southwestern United States into the Rocky Mountain region of Colorado.

Another prominent feature of the summer monsoon circulation seems to be an anticyclonic shear line which runs approximately in a west-east direction over Oregon, southern Idaho and southern Wyoming. This shear line, as a climatological feature, delimits the average northern extent of monsoon-related convective activity in the Rocky Mountain-Great Basin region, as can be seen from satellite composite images.

Tang and Reiter (1984) also were able to show that the rather complicated patterns of rainy and dry seasons on the North American Continent are strongly affected by the western plateau and its monsoonal circulation systems.

(2) Diurnal Circulation Systems

Reiter and Tang (1984) have shown that the summer monsoon season is characterized by a rather prominent diurnal circulation system over the western plateau of the United States. During the night high pressure cells tend to build over the main mountain regions, mainly over Colorado, Arizona and New Mexico, as evident from 850-mb maps enhanced by surface observations. During the day these anticyclonic systems are replaced by heat lows. The two authors were also able to show that the "plateau circulation system" which evolves from these diurnal pressure changes in the planetary boundary layer extends almost to the Mississippi valley, incorporates the Texas low-level jet stream and helps to explain why thunderstorm frequency peaks over most of the Rocky Mountain region in the early afternoon, but over the plains to the east maximizes near, or past, midnight.

(3) Rocky Mountain Low-Level Jet Stream

During a field measurement program carried out in summer of 1984 abrupt changes of wind direction were encountered on top of Mount Werner near Steamboat Springs, Colorado, to the northwest of the high mountains in Rocky Mountain National Park (Reiter et al., 1985). During the day winds tend to blow from the west at moderate speed, following the direction of the Yampa River Valley. In the evening the wind direction quickly shifts to southeast and, during the course of the night, to south. Wind speeds at night, on the average, are higher than during the day, and gusts in excess of 20 m/sec measured 4 m above ground are frequent. We suspect that these winds are the manifestation of a nocturnal low-level jet stream in the planetary boundary layer which is forced by the outflow from the nocturnal anticyclonic cells that develop over the high mountain ranges of the National Park area. This "Rocky Mountain Low-Level Jet" would have to be part of the summer monsoon circulation and provides a first glimpse of boundary layer flow conditions over complex terrain. The existence of these winds could not be substantiated from the regular radiosonde network (Denver and Grand Junction are the closest soundings) because existing stations are in the wrong places and observe at the wrong time of day when these wind systems tend to reverse. Neither do these winds appear from regular surface observations which are valley biased.

The Rocky Mountain Low-Level Jet, if it indeed exists, has several important implications. It appears to be driven by the surface and PBL energy budget which we have made efforts to measure and to model (see subsequent sections of this report). If it is as widespread and frequent a phenomenon as we suspect, this flow could carry air pollution from the copper smelter operations in Arizona and Mexico very efficiently and rather rapidly (much more so than computed from standard meteorological data) into the convective precipitation regions of the Continental Divide where acid rain problems already have been noted. This flow also could be instrumental in providing a direct moisture "pipeline" from the Gulf of California into the severe weather systems over the Rocky Mountains. These systems often have a tendency to move eastward, producing large mesoscale convective systems. Last, but not least, a nocturnal low-level jet at mountain peak elevations could be hazardous, <u>especially to helicopter operations and therefore should be viewed with concern</u>.

In order to investigate this phenomenon more closely we have undertaken to instrument about 20 mountain peaks in western Colorado and northern New Mexico, in collaboration with the Los Alamos National Laboratory and with the U.S. Forest Service. We hope to obtain detailed wind and temperature data, averaged over 15-minute intervals, for most of August 1985. Several of these stations will also measure the surface energy budget. In these efforts we are greatly assisted by the management of local ski resorts who provided us with access permission and with help in erecting the stations and maintaining security. (Unfortunately, the instruments at one station were eaten by a stray herd of cattle).

(4) Energy Balance over Plateau Regions

Chen et al. (1985) and Feng et al. (1985) calculated the daily atmospheric sensible and latent heat budget over the Tibetan Plateau from the middle of May to the end of August 1979, using Nimbus-7 data supplied by NASA and Chinese radiation and surface data (see also Reiter et al., 1985). The Chinese raw data have not yet been released publicly, but had been analyzed by the two Chinese coauthors who were able to draw upon the analysis results. The main reason for the "secrecy" surrounding these data is, that a very large amount of money and physical effort went into the process of obtaining them, and the Chinese authorities, understandably, would like to give first priority to Chinese scientists to "milk" these data for their information contents before releasing them for general consumption. We had to agree with this philosophy because if does not differ much from our own with respect to field data obtained during special programs. Thus, we could present, for the first time, highly interesting analysis results but we have no access, nor can we provide access at this time, to the invaluable original data which went into this analysis work.

The main conclusion to be drawn from the two papers quoted above is that the atmospheric heat source determined "directly" from local energy budget calculations appears to be only half as large over Tibet than that obtained from previous "indirect" estimates which relied mainly on large-scale budgets involving horizontal advection and mass continuity considerations. One of the reasons for these strongly reduced values comes from new estimates of the drag coefficient made at several Tibetan stations, which turns out to be of the order of 3 to 4×10^{-3} instead of 8×10^{-3} suggested by Cressman and since then widely used in numerical modeling. Cressman's value apparently intends to "fudge" some of the form drag effects of the terrain on momentum transport. We seriously have to question, however, whether this approach of using a "universal" (albeit altitude dependent) drag coefficient for heat, moisture and momentum fluxes in some of the currently available models is appropriate. We have successfully experimented with a reduced drag coefficient in a mesoscale model applied over Tibet and over the western United States (Shen et al., 1985a,b) and with a different parameterization of frictional effects on momentum transport, involving mesoscale terrain roughness (D. Tucker, together with Reiter, Ph.D. research work in progress). Our own field measurements in the Gobi Desert and at two sites in the Rocky Mountains, one of them a mountain peak location, confirm the Chinese estimates of coefficients considerable lower than heretofore assumed.

We consider the question of drag coefficient estimates over complex terrain to be highly important for numerical modeling and tend to pursue this problem during present and future field measurement programs.

Preliminary work on a five-year (1976-1980) climatology of the summertime surface energy balance over the western U.S. plateau was described by Reiter et al. (1984). This climatology was obtained using a detailed model of the land surface energy balance (Reiter et al., 1983) which computed surface heat fluxes from hourly station observations of wind, temperature, humidity, cloud cover and precipitation. Although this climatology was useful for diagnosing the main spatial features of hour-to-hour, day-to-day and interannual variations of the plateau heat balance, the model did not explicitly consider variations in vegetation, soil type or aspect. New data obtained from our field studies (Reiter et al., 1985) have already been useful for improving the parameterization of this energy balance model for point measurements in a variety of mountain and plains environments. In our ongoing studies these refinements will allow the computation of a detailed and more reliable energy balance climatology for the region which will be useful as benchmark data in both modeling and climate variation studies.

(5) Climatology of Convective Cloud Development over Mountains

(a) Tibet

A satellite compositing study over Tibet and environs, using microfilm imagery from the Japanese Geostationary Satellite GMS, demonstrated the diurnal evolution of convection, which is largely controlled by the diurnal plateau wind circulation (Reiter and Tang, 1984). A more detailed discussion of the investigation was presented in the 1984 annual report (Reiter et al., 1984). Briefly, June 1979 and July 1980 images were composited for several times of day and varying meteorological conditions. The development of convective cloudiness over the eastern plateau was similar to patterns observed over the Rocky Mountains (Klitch, 1984). East of the plateau over inland China, a midnight cloudiness maximum coincided with observed nocturnal thunderstorm and precipitation maxima. Regions of high cloud frequencies over the plateau matched areas where 10-year mean 100 mb contours (from Kuo and Qian, 1981) showed low pressure centers, while a relatively clear region appeared in a mean belt of high pressure around the plateau.

These composites also illustrated the Chinese and Indian summer monsoons. Composites for days representative of premonsoon, transitional, and onset conditions demonstrated how cloudiness maxima migrate with the monsoon. In addition, the complementary relationship between the Chinese and Indian monsoons was revealed: when convection was suppressed over the eastern plateau, the Indian monsoon was active; conversely, when widespread convective cloudiness occurred over China, low cloud frequencies over India confirmed the "break monsoon" there.

Because we had only two months of imagery and expected composites from microfilm to be of lesser quality than those from either larger hard copy photos or digital data, this compositing study was quite successful in supporting and reinforcing our other more analytical results.

(b) North America

As described in the 1984 annual report (Reiter et al., 1984) hourly GOES satellite images for summer 1981 were manually digitized into fields of tenths coverage for cloud tops colder than -32°C and colder than -53°C. After the tedious process of manual digitization and input, these data have finally been composited and analyzed on our HP9000. The results clearly depict the progression of common patterns of convective development with their strong diurnal character in the Rocky Mountain Region (a more detailed discussion of these results, and maps of composite cloud frequencies are presented in Appendix A. These patterns concur with our previous satellite compositing studies; in addition they cover a broader region, and trace the evolution of convective patterns over the entire day, rather than at selected daytime hours, more completely defining the diurnal cycle and moisture transport paths. Monthly patterns concur remarkably with observed precipitation anomalies.

The most interesting result from these hourly composites was the appearance of the diurnally modulated "moisture bridge" over the Mexican Sierra Madre Occidental (Fig. 26 in Appendix A)(Reiter et al., 1983). Its strong persistence during July suggests it may have a large role in supplying moisture, and thereby upper air instability, over the mountains which could enable mountain induced convection to strengthen into intense storms.

6. Numerical Modeling

(1) Tibetan Studies

Our original attempts to model the development of mesoscale vortices and convective precipitation systems over, and to the east of, the Tibetan Plateau relied heavily on the numerical procedures developed by Anthes and Warner (1978). We soon became aware, however, that the data requirements to initialize this model could not be met over Tibet, mainly because "significant point" data from radiosonde observations were not available to us and the NMC objective analyses over that region leave much to be desired. Even though the essential aspects of atmospheric dynamics and of physical processes were retained from the Anthes-Warner model we have made a number of significant changes in some of the computational routines and parameterizations. These changes render the model rather robust, produce excellent results even with relatively low vertical resolution (6 layers) and allow the full use of observed fields of geopotential height, temperature and winds, assuring the balance between these fields by appropriate interpolation procedures between p- and sigma-coordinates (Shen et al., 1985c,d). As a consequence of our simplifications we are able to run the model on an HP-9020 microcomputer. The latest model version (L. Teixeira, with Reiter and Bresch, Ph.D. dissertation work in progress) requires 2.5 hours of microcomputer time to produce a 24-hour forecast over a domain which almost covers the United States or most of China (41x31 grid points with a grid distance of approximately 96 km). This model version also uses a significantly improved subgrid-scale precipitation parameterization.

A number of interesting experiments have been carried out with this model. We studied the development of mesoscale vortices over Tibet before and after the burst of the summer monsoon season. The model accurately described the different vortex formations, life histories and movements under differing synoptic forcing (Shen et al., 1985a). By removing certain processes from the model we were able to demonstrate the effects of sensible heating, large-scale heating by grid-scale precipitation, subgrid-scale convective heating, and topography on vortex development. Special attention was given to the effects of sensible heating of the atmosphere from the earth's surface (Shen et al., 1985e). These effects depend strongly on the synoptic condition, especially on the position of the jet stream, and on topography, but less strongly on the kind of parameterization that is used to arrive at values of the surface heat flux. In conjunction with topography, sensible heating tends to enhance the blocking effects of plateaus against cold-air invasions.

(2) U.S. Studies

Two major studies in this area have been initiated during the last grant year and are still in progress, but results have not yet been published. Teixeira's dissertation work has proceeded well by drastically improving the parameterization of subgrid-scale precipitation. A case study of severe mesoscale convective systems development east of the Rocky Mountains is in progress which succeeded in modeling the associated precipitation events highly satisfactorily. Additional case studies will be conducted to test the sensitivity and also the reliability of these parametric approaches.

Tucker's dissertation work involves the development of a nested grid model with 24 km grid distance in the subdomain. The intent of this work is to model the Big Thompson Flood of 1976 which produced in excess of 11 inches of rain in less than 24 hours in the Estes Park area, not far from Ft. Collins, and claimed over 130 lives in a flash flood. In the present model configuration the nested grid, which contains the appropriate topographic details, computes convective precipitation explicitly, using the larger-grid wind fields in the lowest model layer to impose the synoptic development on the nested grid domain and modifying the flow in that domain according to topographic forcing, then feeding moisture and mass flux convergences back into the larger grid. Thus, the two grids are interactive, both relying on a sigma-coordinate system, but only the lowest layer carries through the required computation in the fine-mesh grid. This approach realizes considerable savings in computer time and allows us to run this model on the HP-9020. Model initialization is carried out by using objectively analyzed fields of meteorological variables. A further innovation has been introduced by accounting for frictional effects in computing a terrain roughness which is a stability-dependent function of the standard deviation of terrain heights evaluated from a grid with 1 km mesh width. The model reproduced astoundingly well the Estes Park precipitation disaster and gave appropriate negative results in a "dry" synoptic case over the same model domain. It could also be shown from this study that the detailed topography, indeed, was the major factor in concentrating the convective precipitation development. The mesoscale model alone, without the nested-grid enhancement, was unable to reproduce this rather localized flood disaster.

7. Field Measurement Programs

(1) Gobi Experiment

During April 1984, and again during June/July 1984 measurements of the surface energy budget were carried out near Zhangye on the southern edge of the Gobi Desert where it abuts the northern edge of the Tibetan Plateau of Qinghai Province (Reiter et al., 1985). The instruments for this program were acquired through the current Air Force grant. A number of interesting results were obtained:

The diurnal wind variations differed drastically between spring and summer. In both seasons the heating effects of the nearby plateau became evident, but the controlling synoptic systems were different. Only in summer a change between daytime heat-low and nocturnal anticyclonic conditions in the planetary boundary layer of the plateau could be deduced.

Latent heat fluxes contributed significantly to the surface energy budget during summer. The radiation budget during that season was strongly affected by rather high relative humidities which we attributed to widespread irrigation in the close by oasis of Zhangye. The albedo in the near-infrared portion of the solar spectrum was about twice as high as in the visible part of the spectrum, as should be expected over dry soil. An approximate value of 2×10^{-3} was obtained for the drag coefficient at that measurement site.

The instruments remained in China and, hopefully, will be used in conjunction with a Tibet measurement program scheduled for June/July 1986.

(2) Pingree Park Measurements

During late winter and spring 1984 surface energy budget measurements were carried out in a forest clearing at Pingree Park, 60 km west of Ft. Collins, but east of the Continental Divide at 2750 m above m.s.l. (Reiter et al., 1985). The project obtained exceptionally good data during a period when the snow cover at the site disappeared rapidly. As long as snow was on the ground the sensible heat flux between air and ground remained slightly negative with little diurnal variation. Most of the energy flux to the atmosphere was carried by latent heat with strong diurnal variability. After the snow melted the sensible heat flux to the atmosphere assumed "climatological" values within about three days while the latent heat flux diminished as the top layer of the soil dried out. This rapid adjustment of heat fluxes after the melting of the snow cover casts some doubt on the "long memory" effects of snow cover by local processes on general circulation patterns. If such memory effects exist, as suggested by the negative correlation between Tibetan snow cover and precipitation during the subsequent Indian summer monsoon, they must be due to large-scale teleconnections rather than to local heat budget variations.

Albedo values in the near-infrared were nearly 1/3 lower with snow than the visible-radiation albedo, however they were twice as high as the visible albedo with the snow removed.

(3) Mount Werner Measurements

The significant diurnal variation of the wind regime on this mountain peak near Steamboat Springs (3200 m above m.s.l.) has already been described earlier (see also Reiter et al., 1985). The surface energy budgets measured at this site agreed well with the observed wind reversal. A drag coefficient of 3×10^{-3} was estimated for this mountaintop site. Albedo values in the visible spectrum range were of the order of 0.05 whereas in the near-infrared portion of the spectrum they attained values of about 0.25 to 0.30 during the noon hours, with much higher values prevailing mornings and evenings.

References

Anthes, R.A. and T.T. Warner, 1978: Development of hydrodynamic models suitable for air pollution and other mesometeorological studies. Mon. Wea. Rev., 106, 1045-1078.

Chen, Longxun, Elmar R. Reiter and Zhiqiang Feng, 1985: The atmospheric heat source over the Tibetan Plateau from May to August 1979. Accepted for publication in Mon. Wea. Rev.

Cotton, William R., Edward E. Hindman, Gregory Tripoli, Ray L. McAnelly, C. Chen, C. Tremback, D. Flatau, and K. Knupp, 1984: Model cloud relationships. Final Report, 26 Nov. 1981-30 Sept. 1983. Fl 9628-82-K-0003 Air Force Geophysics Laboratory, Air Force Systems Command, United States Air Force, Hanscom AFB, Massachusetts (AFGL-TR-84-0028).

Ding, Yi-Hui and Elmar R. Reiter, 1982: A relationship beteween planetary waves and persistent rain- and thunderstorms in China. Arch. Met. Geoph. Biokl , Ser. B, 31, 221-252.

Feng, Zhiqiang, Elmar R. Reiter and Longxun Chen, 1985: The atmospheric heat budget over the western part of the Tibetan Plateau during Monex, 1979. Submitted for publication to Advances in Atmospheric Science, China Ocean Press, Beijing, People's Republic of China.

Klitch, Marjorie A., 1984: Analysis of convection over the Tibetan Plateau using composite satellite imagery. Third Conference on Mountain Meteorology, Amer. Meteorol. Soc., October 16-19, 1984. Portland OR. 3 p.

Kuo, H.L. and Y.F. Qian, 1981: Influence of the Tibetan Plateau on cumulative and diurnal changes of weather and climate in summer. Mon. Wea. Rev., 190(11):2337-2356.

Maddox, R.A., 1983: Large-scale meteorological conditions associated with midlatitude, mesoscale convective complex. Mon. Wea. Rev., 111, 1475-1493.

McAnelly, Ray L. and William R. Cotton, 1985a: Meso-β-scale characteristics of the meso-α-scale convective complex. To appear in Mon. Wea. Rev.

McAnelly, Ray L. and William R. Cotton, 1985b: The precipitation life cycle of mesoscale convective complexes. Preprints, Sixth Conf. of Hydrometeorology, Amer. Meteor. Soc., 28-31 October, 1985, Indianapolis, Indiana, 8 p.

Reiter, Elmar R., 1982: Typical low-tropospheric pressure distributions over and around the Plateau of Tibet. Arch. Met. Geoph. Biocl., Ser. A, 31, 323-327.

Reiter, Elmar R., 1983: Teleconnections with tropical precipitation surges. J. Atmos. Sci., 40(7), 1631-1647.

Reiter, Elmar R., John D. Sheaffer, Donna F. Tucker, Ray L. McAnelly, Marjorie A. Klitch, William L. Cotton and Maocang Tang, 1983: Effects of mountain ranges on mesoscale systems development. Annual Report to U.S. Air Force Office of Scientific Research, Grant No. AFOSR 82-0162, May 1983.

Reiter, Elmar R. and Maocang Tang, 1984: Plateau effects on diurnal circulation patterns. Mon. Wea. Rev., 112(4):638-651.

Reiter, Elmar R., John D. Sheaffer, Marjorie A. Klitch, Ray L. McAnelly, Shen Rujin and Donna F. Tucker, 1984: Effects of mountain ranges on mesoscale systems development. Annual Report to U.S. Air Force Office of Scientific Research, Grant No. AFOSR 82-0162. May 1984.

Reiter, Elmar R. and Maocang Tang, 1984: Plateau effects on diurnal circulation patterns. Mon. Wea. Rev., 112(4):638-651.

Reiter, Elmar R., John D. Sheaffer and Eric A. Smith, 1985: Surface energy fluxes in complex terrain. Panel Reivew of Data Analysis, Modeling, and Theoretical Research in the NASA Global Scale Atmospheric Processes Research Program, Columbia, MD, 8-12 July 1985.

Shen, Rujin, Elmar R. Reiter and James F. Bresch, 1985a: Numerical simulation of the development of vortices over the Qinghai-Xizang (Tibet) Plateau. Accepted for publication in Arch. Met. Geophy. Biocl.

Shen, Rujin, Elmar R. Reiter, and James F. Bresch, 1985b: A simplified hydrodynamic mesoscale model suitable for use over high plateau meteorological variables. Accepted for publication in Arch. Meteor. Geophy. Biocl.

Shen, Rujin, Elmar R. Reiter and James F. Bresch, 1985c: On vertical interpolation of meteorological variables. Accepted for publication in Mon. Wea. Rev.

Shen, Rujin, Elmar R. Reiter, James F. Bresch, and Shuhua Zhang, 1985d: On temperature initialization in primitive equation forecast models. Submitted to Mon. Wea. Rev.

Shen, Rujin, Elmar R. Reiter and James F. Bresch, 1985e: Some aspects of the effect of sensible heating on development of summer weather systems over the Tibetan Plateau. Submitted to Mon. Wea. Rev.

Tang, Maocang and Elmar R. Reiter, 1984: Plateau monsoons of the northern hemisphere: A comparison between North America and Tibet. Mon. Wea. Rev., 112(4), 617-637.

Webster, P.J. and J.R. Holton, 1982: Cross-equatorial response to middle-latitude forcing in a zonally varying basic state. *J. Atmos. Sci.*, *39*, 722-733.

APPENDIX A

A SATELLITE CLIMATOLOGY OF INTENSE CONVECTIVE STORMS FROM MANUALLY DIGITIZED HOURLY CLOUD COVER FIELDS

by

Marjorie A. Klitch

A SATELLITE CLIMATOLOGY OF INTENSE CONVECTIVE STORMS FROM MANUALLY DIGITIZED HOURLY CLOUD COVER FIELDS

1. Introduction

To be useful in a climatological study, satellite data must be reduced from enormous bit streams to a compact, readily interpretable form. Several methods of compositing satellite data have been used to examine the influence of the Rocky Mountains on the diurnal convective cycle (see Klitch et al., 1985). Because the acquisition and manipulation of digital satellite data for a compositing study can be costly, a different approach was employed in this investigation and is described below.

The purpose of this study was to define common patterns of mesoscale convective development in the western United States, including areas with frequent initiation and development of storms, and their subsequent tracks, and to test the efficacy of this method of reducing and analysing satellite data. Although the results discussed below complement those within this and other research projects, we intend to complete this climatology by performing a principal component (eigenvector) analysis, funded by a separate AFOSR Contract F49620-85-C-0079. Upon completion of this additional analysis this article, in updated form, will be submitted to a refereed journal for publication, probably Meteorology and Atmospheric Physics (formerly Archives of Meterology, Geophysics and Bioclimatology).

2. Satellite Data and Reduction Method

Hourly infrared laserfax satellite imagery, enhanced with the MB scheme (GOES Users Guide, 1983), from both GOES-West and GOES-East were available for June through August 1981. These photos were manually digitized by overlaying a 1° x 1° latitude/longitude grid on each image and visually estimating the fractions (in tenths) of each grid cell between 90° and 125° E longitude and 25° to 50° N latitude with cloud top temperatures below -32°C and below -53°C (easily discernible steps in the gray shade contours of the MB enhancement curve).

After the satellite images were digitized into 35 x 25 arrays, these reduced data fields were manually entered as data files* into a VAX 11-780, checked, and transferred via magnetic tape to our research group's HP9000. Because the August 1981 data set had many gaps (photos incomplete or unavailable), only the June and July 1981 cloud coverage fields were analyzed in this investigation. GOES-West had a more direct view of the region, so its xx15** images were usually used; when xx15 photos were not available, digitized fields for GOES-East's xx00 and xx30 photos were averaged to fill these occasional gaps. Also, because GOES-East's view of the region between 120° and 125° E is at too oblique an angle to reliably estimate cloud coverage, this region has not been included in plots of average cloud coverage.

Composite fields of cloud cover colder than -32°C and -53°C were computed for each hour and for each month by averaging the daily fields. "Overall averages" were created by averaging all days at all times for each month. Contour plots of these average fields are presented and discussed in the following section.

---

*Some of these data were on punched cards and were merged with the hand entered data files upon entry to the VAX.

**Both GOES satellites produce images every half hour: GOES-East on the hour (xx00) and half hour (xx30); GOES-West at fifteen minutes past (xx15) and forty-five minutes past (xx45) the hour.

3. Results

Due to the multidimensionality of the data set, the hourly averaged cloud cover fields can be analysed and interpreted in several ways. This discussion contemplates the following:

- How do the diurnal and orographic forcing of the convective cycle vary over the domain?
- Where and when does the deep (i.e., cloud tops -32°C or colder) convection occur first? Where is it most frequent? What path or pattern of progression does it generally take?
- How does June differ from July? Does the reported precipitation correspond to the computed cloud coverage patterns?
- How do these results support or confirm those from other research efforts?

A. Spatial Variations

The timing and intensity of the diurnal convective cycle vary with location. Evolution of average hourly cloud cover at different locations indicates that locations closer to the mountains have a more pronounced diurnal signal. Tables I and II show the average hourly cloud cover for the two temperature thresholds for June and July respectively, for three regions in the domain. Cloud coverage reaches its peak values over mountain areas first, but areas further east have greater peak cloud coverage values, probably due to greater moisture availability at lower altitudes. Other details of the spatial variation of diurnal convective development are discussed below.

B. Timing and Development Patterns

The maps of hourly average cloud coverage fields for June and July, presented in Figs. 1a-24d, have contour intervals of 10 percent for the

-32°C fields and 5 percent for the -53°C; thus, finer scale details are not shown. Convection usually begins over the mountains by 11 a.m. local time when remnants from the previous day's activity are still decaying over the eastern plains of Minnesota, Iowa, and Missouri (Fig. 17). As cloud coverage over the mountains and foothills grows, it diminishes over the plains in agreement with the existence of a diurnal plateau circulation system (Reiter and Tang, 1984). At 0015 GMT (a few hours earlier in July), when cloud coverage values peak in the mountains, several areas where orographically induced convection frequently originates are apparent (Fig. 14): the Cheyenne Ridge (eastern CO/WY border), the Palmer Divide (east central CO), and the Raton Mesa (eastern CO/NM border). As has been noted in other studies over the Rocky Mountains for other years (Klitch and Vonder Haar, 1982; Weaver and Kelly, 1982; and Philip, 1979), after reaching its peak over the mountains, maximum cloud frequencies move eastward and also a little northward.

Two other diurnally modulated centers of high convective cloud coverage are over north central Mexico and along the east Texas gulf coast. The latter seems to be influenced by land/sea temperature differences (sea breeze), as it reaches maximum extent in the late afternoon around 2315 GMT (Fig. 12) and is practically nonexistent a few hours after dark at 0515 GMT (Fig. 18).

Although gulf moisture can sometimes contribute to high plains convective storms, the Mexican center of high convective cloud frequencies is of more importance in unraveling the intricacies of mountain forcing. Recently in studies of satellite imagery from other years, the existence of this "moisture bridge" has been confirmed and investigated

(Reiter et al., 1983). In these hourly composites it seems to have a maximum intensity at 0015 GMT (1715 MST) and migrate west and north, where it is weakest around 1515 GMT (0815 MST). The ability of the Mexican Sierra Madre to help force tropical moisture high into the atmosphere may be instrumental in guiding the upper air instabilities that lead to mountain induced storms on the high plains. Our impending principal component analysis should help define the behavior of this phenomenon more clearly. Having a significantly longer and denser data set than Tucker did (in Reiter et al., 1983) should improve the detail and significance of the results.

C. June vs. July

Although the evolution of the average cloud coverage fields described above for June and July 1981 is similar, the obvious differences merit discussion. Climatologically the differences between convective activity in June and July should be small; insolation is more intense in June, but ambient air (and soil) temperatures are warmer in July. In Figs. 1-24, convection seems to begin a little sooner and grow a little stronger over the mountains in July. However, in 1982 the atmosphere underwent changes between June and July that resulted in remarkably different precipitation patterns. Figures 25c and 26c show the precipitation as a percentage of normal for June and July 1981, published in Weatherwise (Ludlam, 1981a; Ludlam, 1981b). When the hourly average cloud coverage fields for each month are averaged together to yield an "overall average" (Figs. 25a and b, and 26a and b) they compare quite favorably with the observed precipitation. Thus, with observed precipitation considerably above normal in the mountain west during July, available moisture was greater and convective clouds could form sooner and grow larger and deeper than in June.

Table I. Diurnal evolution of average cloud coverage in percent over 1° square for June 1981, colder than -32°C and colder than -53°.

		Mountain		Foothills		Plains	
		(39.5, 105.5)		(40.5, 104.5)		(38.5, 92.5)	
MST	(GMT)	-32	-53	-32	-53	-32	-53
1715	(0015)	20.3	4.5	24.1	5.9	15.5	4.1
1815	(0115)	16.7	3.7	28.0	3.7	18.3	5.7
1915	(0215)	11.0	1.7	28.3	5.2	17.9	3.8
2015	(0315)	12.4	1.0	22.1	5.5	21.4	9.7
2115	(0415)	11.0	0.3	18.6	5.5	23.8	15.2
2215	(0515)	5.5	(0)	14.5	2.1	30.7	17.2
2315	(0615)	4.1	0.3	4.8	1.0	31.0	16.9
0015	(0715)	3.1	0.3	7.9	0.3	26.2	15.2
0115	(0815)	4.1	0.3	6.9	0.7	21.4	10.3
0215	(0915)	(1.4)	(0)	8.6	1.4	26.6	12.1
0315	(1015)	2.8	0	6.6	1.4	27.2	14.5
0415	(1115)	1.7	0.3	4.5	1.4	24.5	15.9
0515	(1215)	2.8	0.3	2.4	(0)	26.6	16.6
0615	(1315)	3.8	0.7	(1.7)	0	25.5	12.1
0715	(1415)	5.2	0.3	1.7	0	22.1	12.4
0815	(1515)	5.5	0.3	3.4	0	26.2	13.8
0915	(1615)	5.5	0.3	3.4	0	21.6	13.8
1015	(1715)	3.8	(0)	4.5	0	16.2	13.8
1115	(1815)	3.1	0	3.8	0.3	16.6	11.4

Table I. (continued)

		Mountain		Foothills		Plains	
		(39.5, 105.5)		(40.5, 104.5)		(38.5, 92.5)	
MST	(GMT)	-32	-53	-32	-53	-32	-53
1215	(1915)	4.1	0	5.5	0	14.8	5.2
1315	(2015)	11.7	0	8.3	0.3	14.5	3.8
1415	(2115)	13.4	0.3	12.1	1.4	(12.1)	2.8
1515	(2215)	15.9	3.1	20.0	3.4	15.2	(2.4)
1615	(2315)	16.6	3.1	21.4	5.2	16.2	3.4

_____ = maximum

(   ) = minimum

Table II. Diurnal evolution of average cloud coverage in percent over 1° square for July 1981, colder than -32°C and colder than -53°.

		Mountain		Foothills		Plains	
		(39.5, 105.5)		(40.5, 104.5)		(38.5, 92.5)	
MST	(GMT)	-32	-53	-32	-53	-32	-53
1715	(0015)	14.8	4.8	11.1	4.2	9.4	3.9
1815	(0115)	15.2	4.5	15.2	4.5	11.9	6.5
1915	(0215)	12.6	3.2	13.9	4.8	13.2	8.7
2015	(0315)	10.0	2.6	11.9	4.8	14.2	9.4
2115	(0415)	7.4	(0)	11.0	5.5	11.9	6.8
2215	(0515)	3.5	0	10.3	4.8	10.3	6.1
2315	(0615)	2.3	0	8.7	5.2	11.0	7.4
0015	(0715)	1.3	0	6.1	0.6	8.7	4.8
0115	(0815)	1.9	0	2.6	(0)	11.0	9.0
0215	(0915)	1.9	0	1.9	0	13.9	5.8
0315	(1015)	0.3	0	1.0	0	15.2	4.8
0415	(1115)	0.6	0	1.3	0	19.4	3.9
0515	(1215)	0.3	0	0.3	0	16.8	4.2
0615	(1315)	1.6	0	1.3	0	21.0	4.2
0715	(1415)	0.3	0	1.6	0	8.4	1.6
0815	(1515)	0.3	0	0.6	0	6.1	0.3
0915	(1615)	(0)	0	(0)	0	4.2	(0)
1015	(1715)	1.6	0	0.3	0	(3.2)	0
1115	(1815)	3.2	0	0.3	0	6.1	0

Table II. (continued)

		Mountain		Foothills		Plains	
		(39.5, 105.5)		(40.5, 104.5)		(38.5, 92.5)	
MST	(GMT)	-32	-53	-32	-53	-32	-53
1215	(1915)	6.5	0.3	1.0	0	6.5	0
1315	(2015)	11.6	0.6	0.6	0	4.2	0
1415	(2115)	13.9	2.3	3.5	0	7.1	0.3
1515	(2215)	$\underline{15.2}$	2.9	4.2	0.3	7.7	0.6
1615	(2315)	18.1	4.5	10.6	2.3	8.7	1.6

_____ = maximum

(   ) = minimum

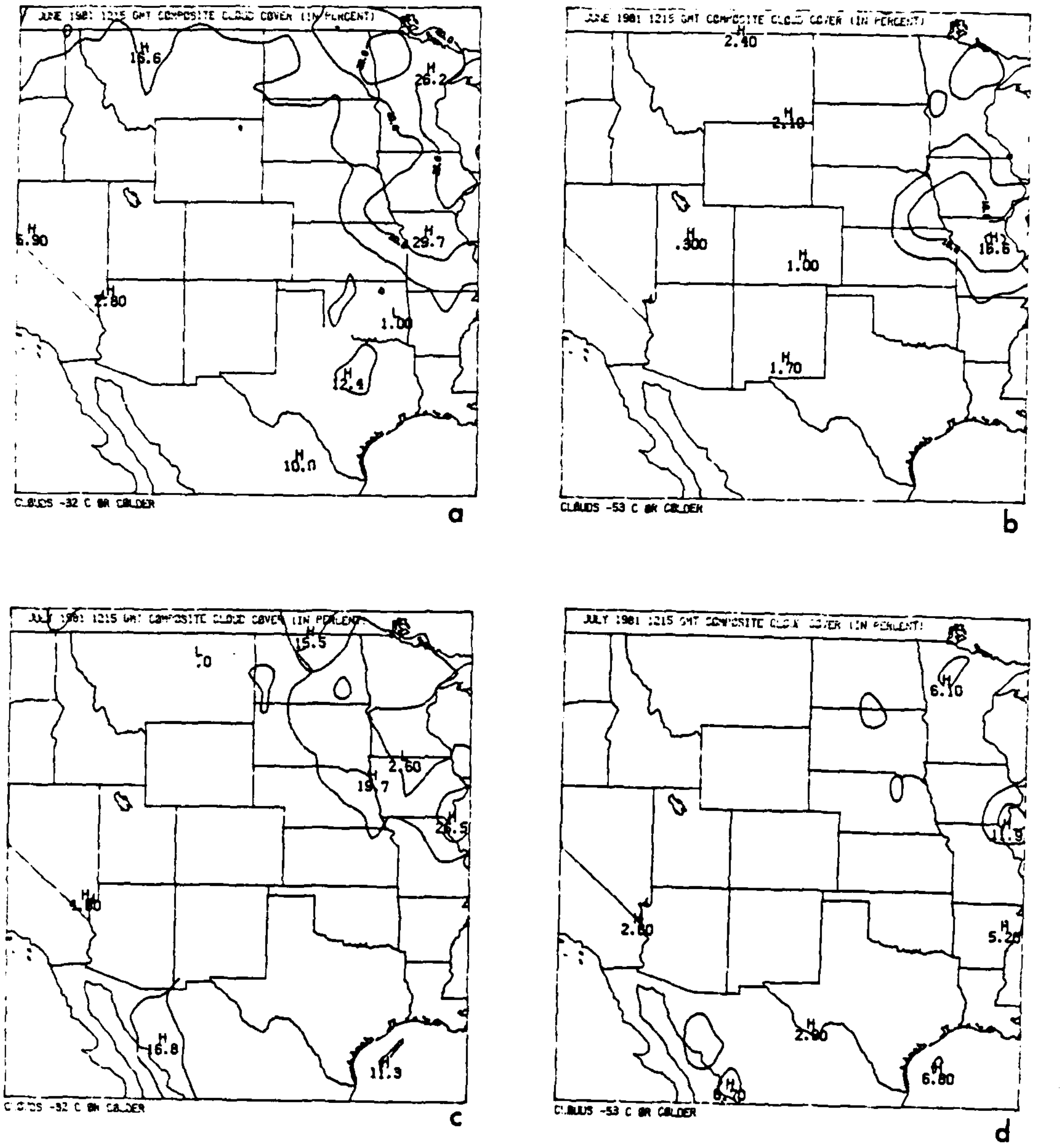

Figure 1 Average cloud cover over a 1° x 1° area in percent at 0515 MST (1215 GMT): a) June 1981, colder than -32°C; b) June 1981, colder than -53°C; c) July 1981, colder than -32°C; d) July 1981, colder than -53°C.

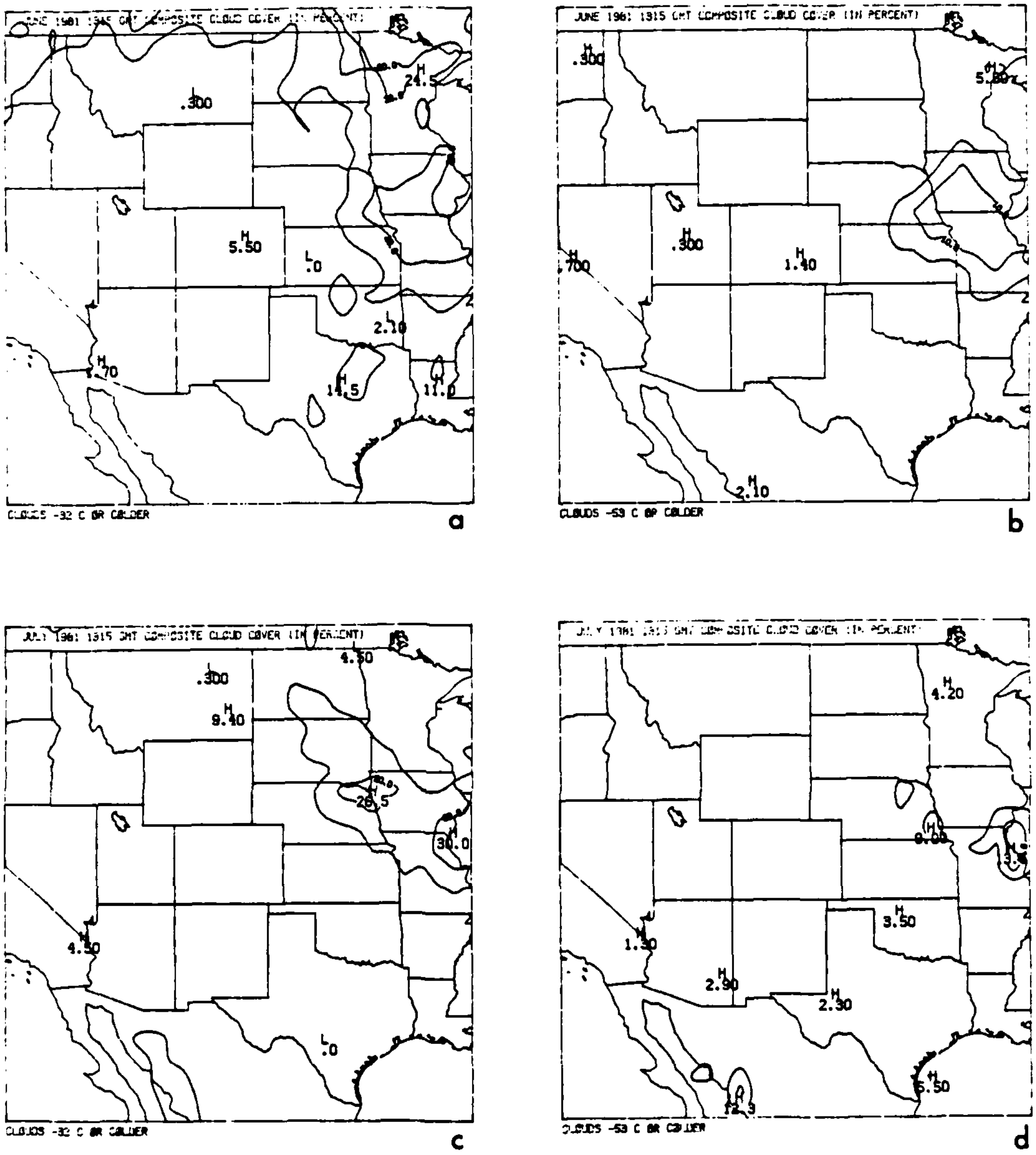

Figure 2 Average cloud cover over a 1° x 1° area in percent at 0615 MST (1315 GMT): a) June 1981, colder than -32°C; b) June 1981, colder than -53°C; c) July 1981, colder than -32°C; d) July 1981, colder than -53°C.

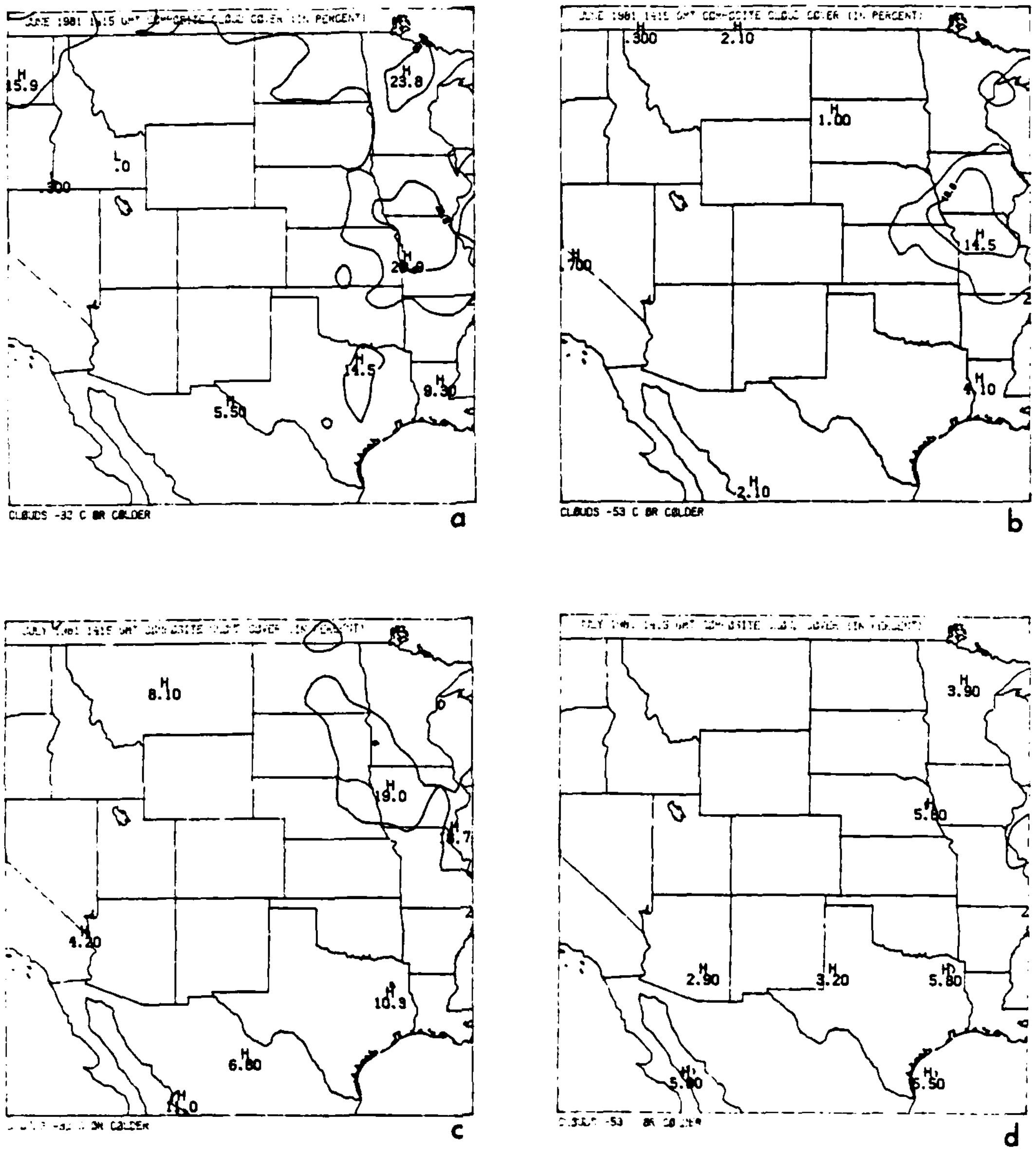

Figure 3 Average cloud cover over a 1° x 1° area in percent at 0715 MST (1415 GMT): a) June 1981, colder than -32°C; b) June 1981, colder than -53°C; c) July 1981, colder than -32°C; d) July 1981, colder than -53°C.

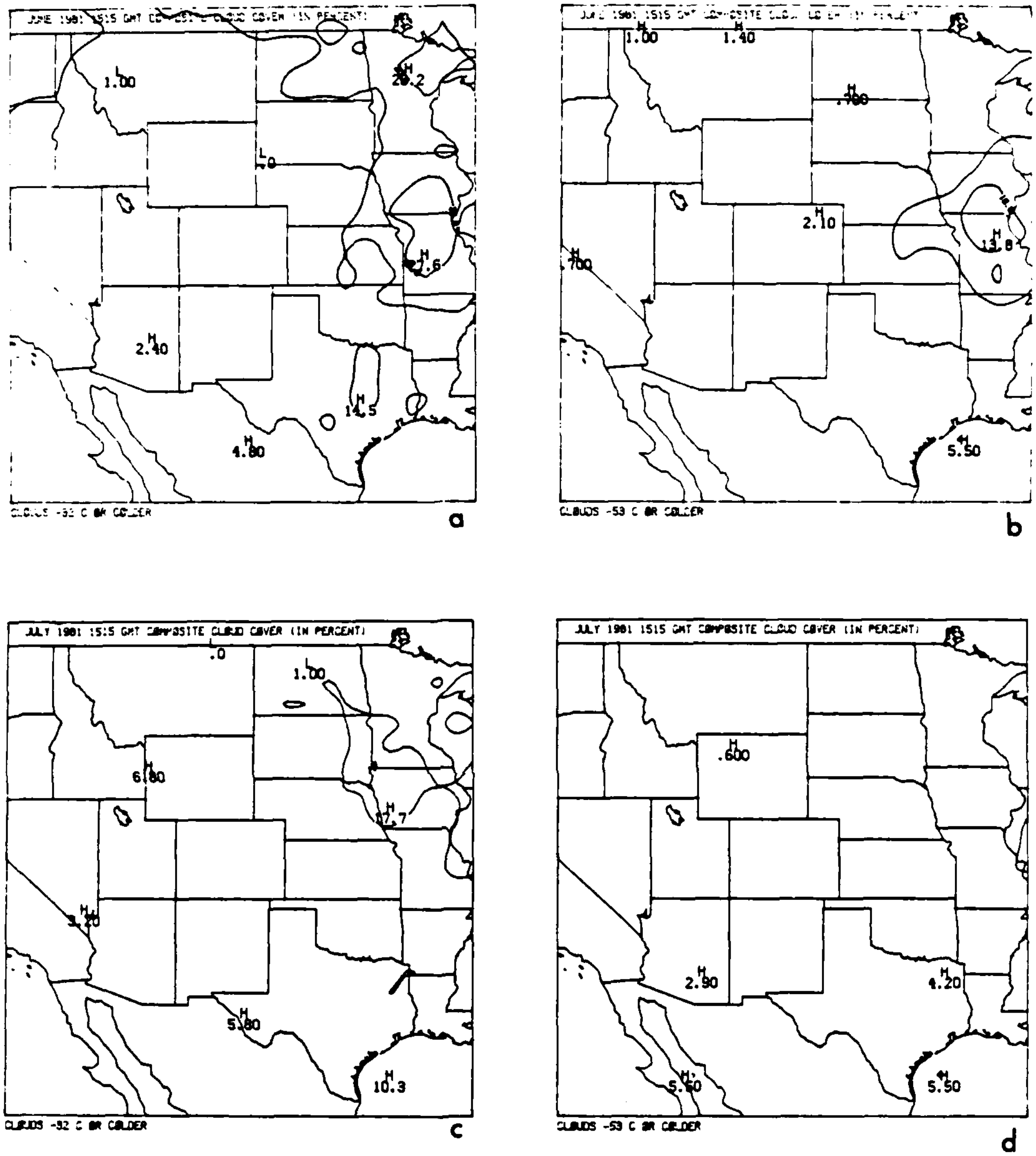

Figure 4 Average cloud cover over a 1° x 1° area in percent at 0815 MST (1515 GMT): a) June 1981, colder than -32°C; b) June 1981, colder than -53°C; c) July 1981, colder than -32°C; d) July 1981, colder than -53°C.

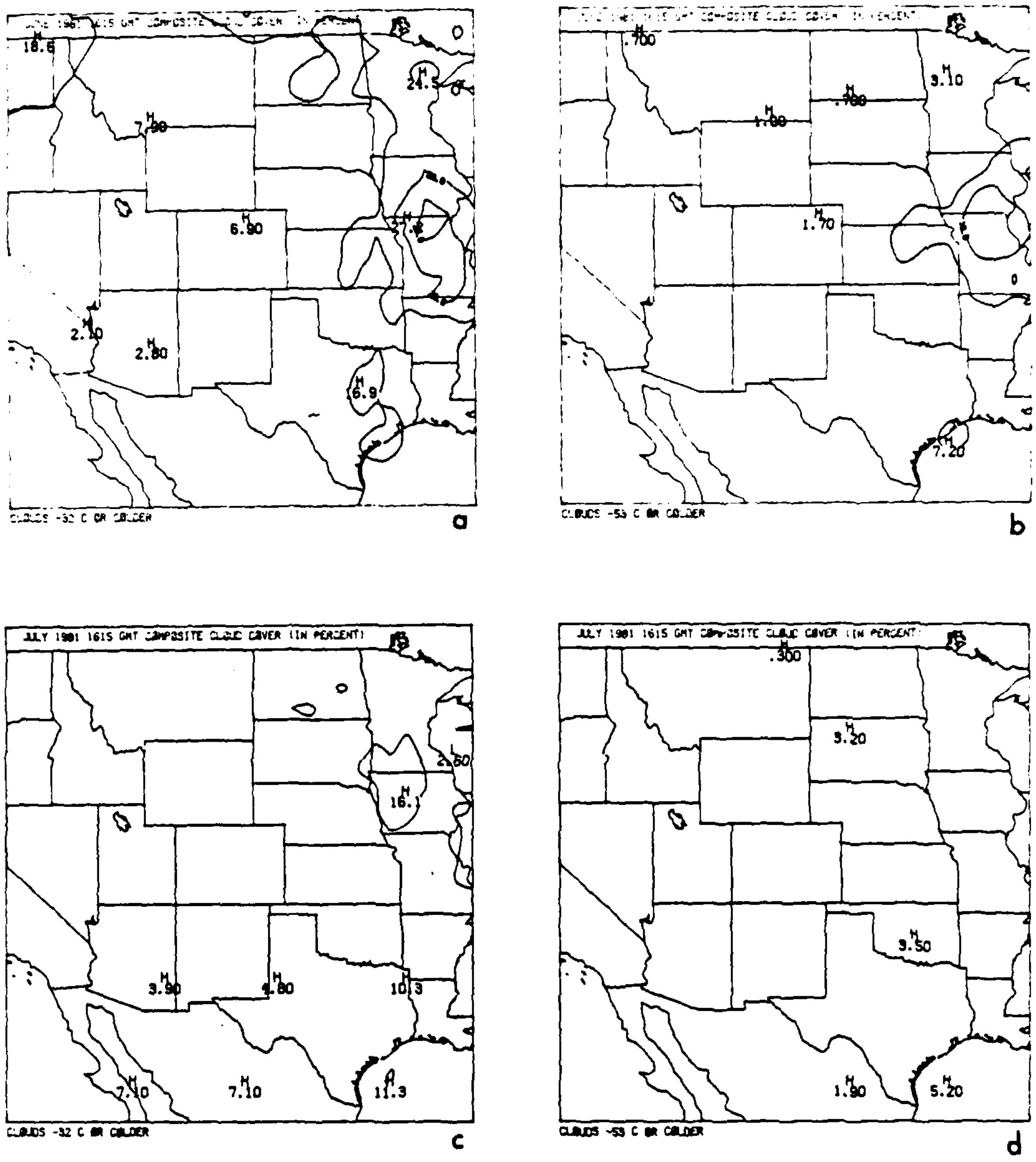

Figure 5 Average cloud cover over a 1° x 1° area in percent at 0915 MST (1615 GMT): a) June 1981, colder than -32°C; b) June 1981, colder than -53°C; c) July 1981, colder than -32°C; d) July 1981, colder than -53°C.

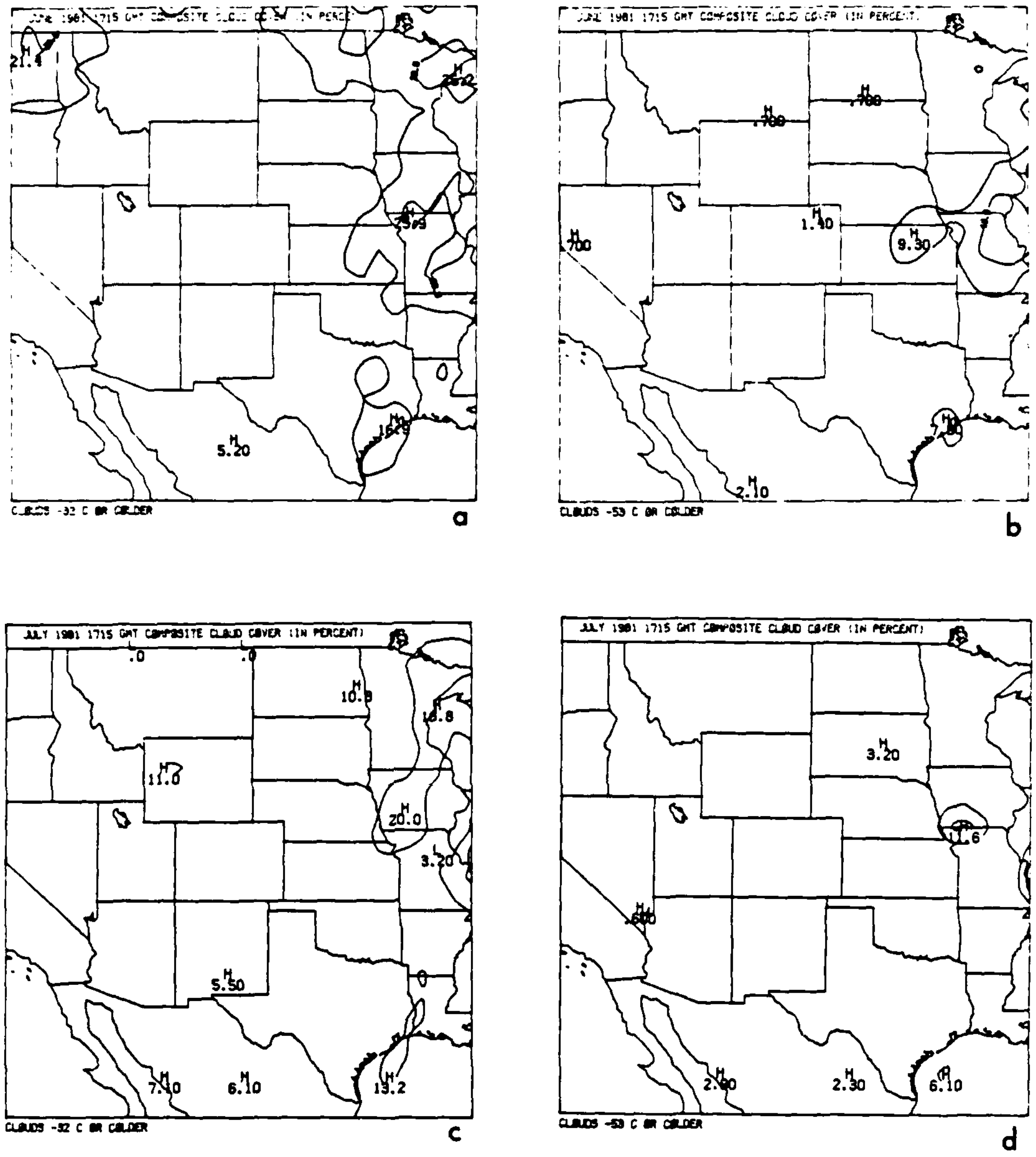

Figure 6 Average cloud cover over a 1° x 1° area in percent at 1015 MST (1715 GMT): a) June 1981, colder than -32°C; b) June 1981, colder than -53°C; c) July 1981, colder than -32°C; d) July 1981, colder than -53°C.

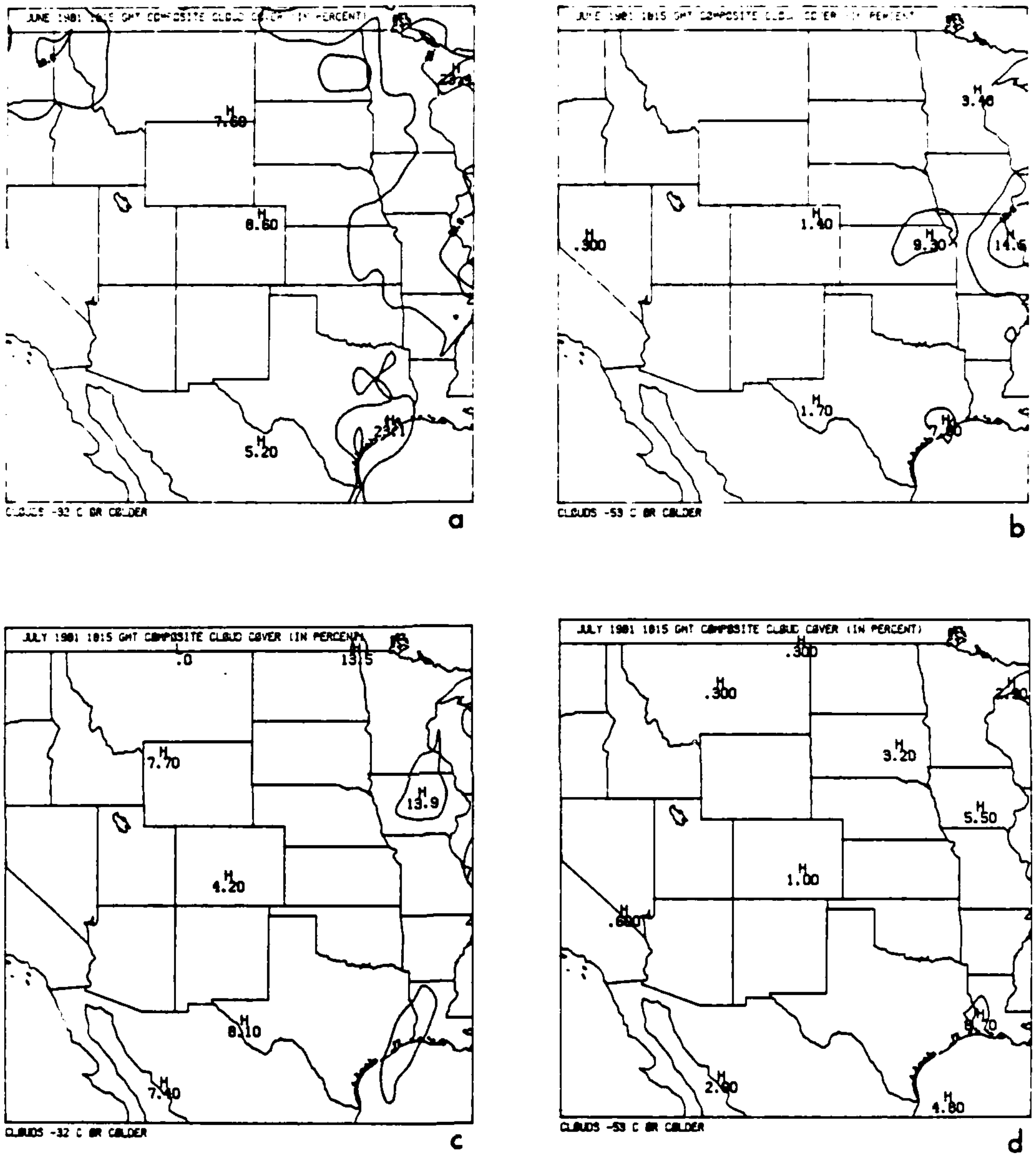

Figure 7 Average cloud cover over a 1° x 1° area in percent at 1115 MST (1815 GMT): a) June 1981, colder than -32°C; b) June 1981, colder than -53°C; c) July 1981, colder than -32°C; d) July 1981, colder than -53°C.

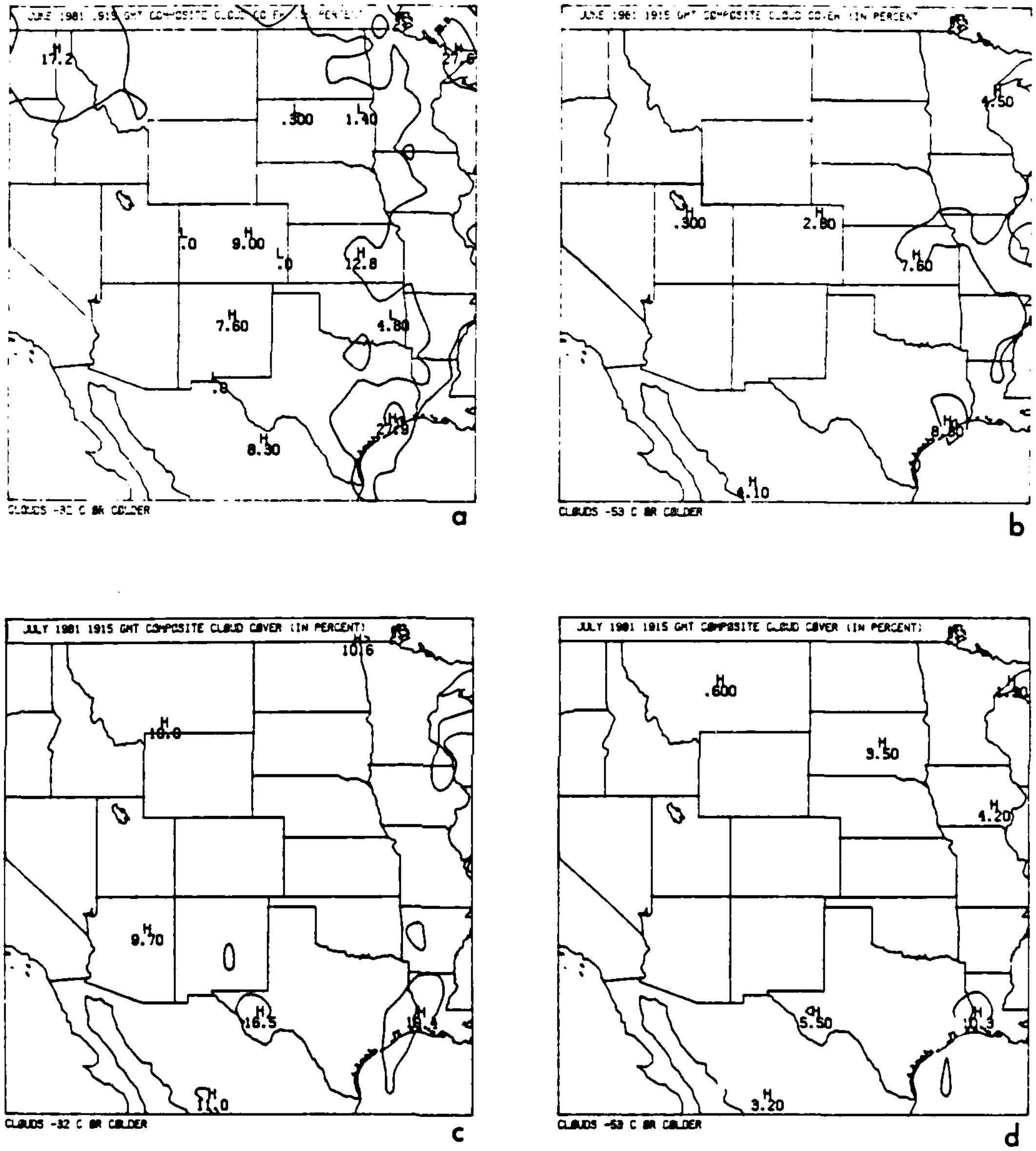

Figure 8 Average cloud cover over a 1° x 1° area in percent at 1215 MST (1915 GMT): a) June 1981, colder than -32°C; b) June 1981, colder than -53°C; c) July 1981, colder than -32°C; d) July 1981, colder than -53°C.

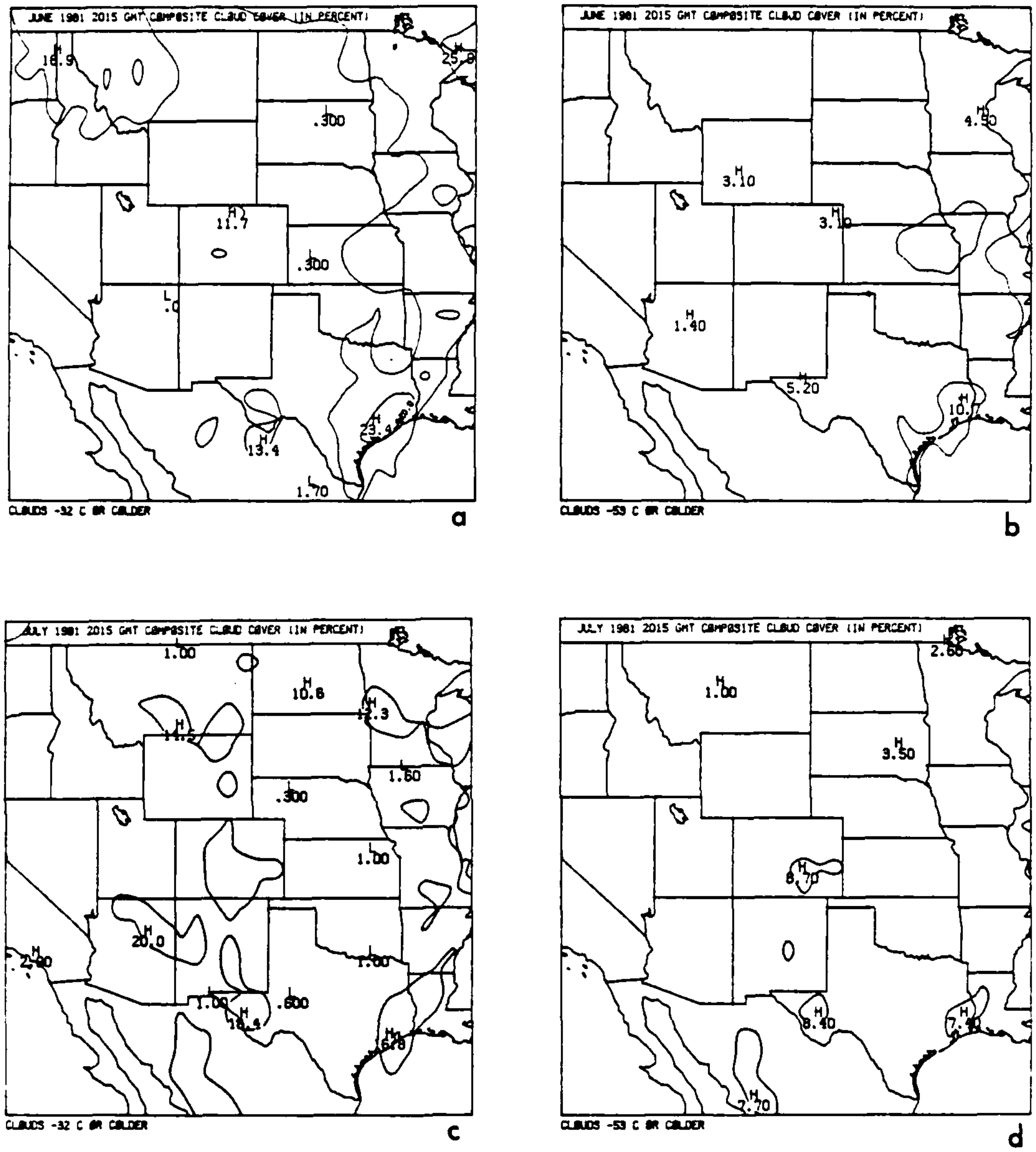

Figure 9 Average cloud cover over a 1° x 1° area in percent at 1315 MST (2015 GMT): a) June 1981, colder than -32°C; b) June 1981, colder than -53°C; c) July 1981, colder than -32°C; d) July 1981, colder than -53°C.

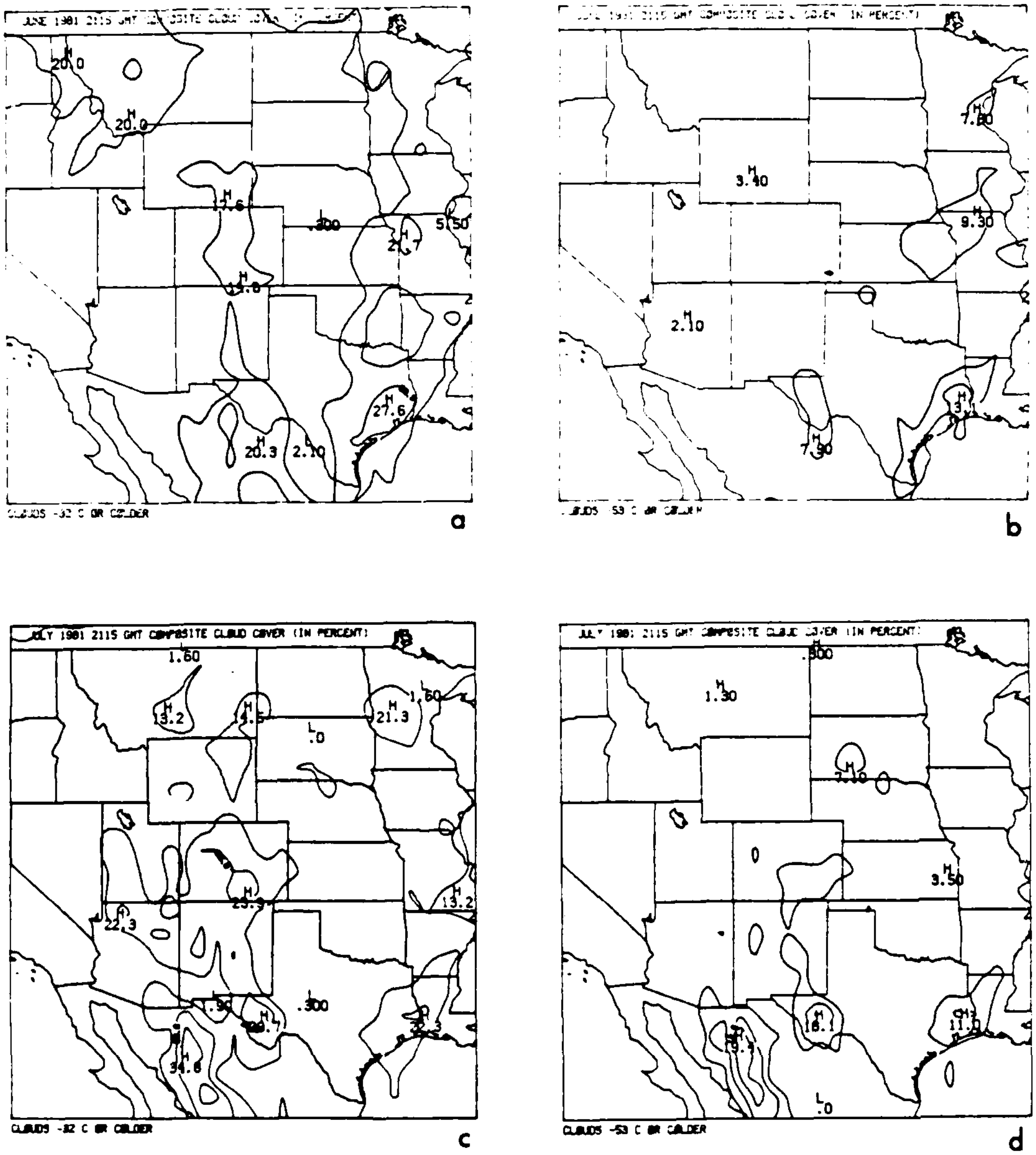

Figure 10 Average cloud cover over a 1° x 1° area in percent at 1415 MST (2115 GMT): a) June 1981, colder than -32°C; b) June 1981, colder than -53°C; c) July 1981, colder than -32°C; d) July 1981, colder than -53°C.

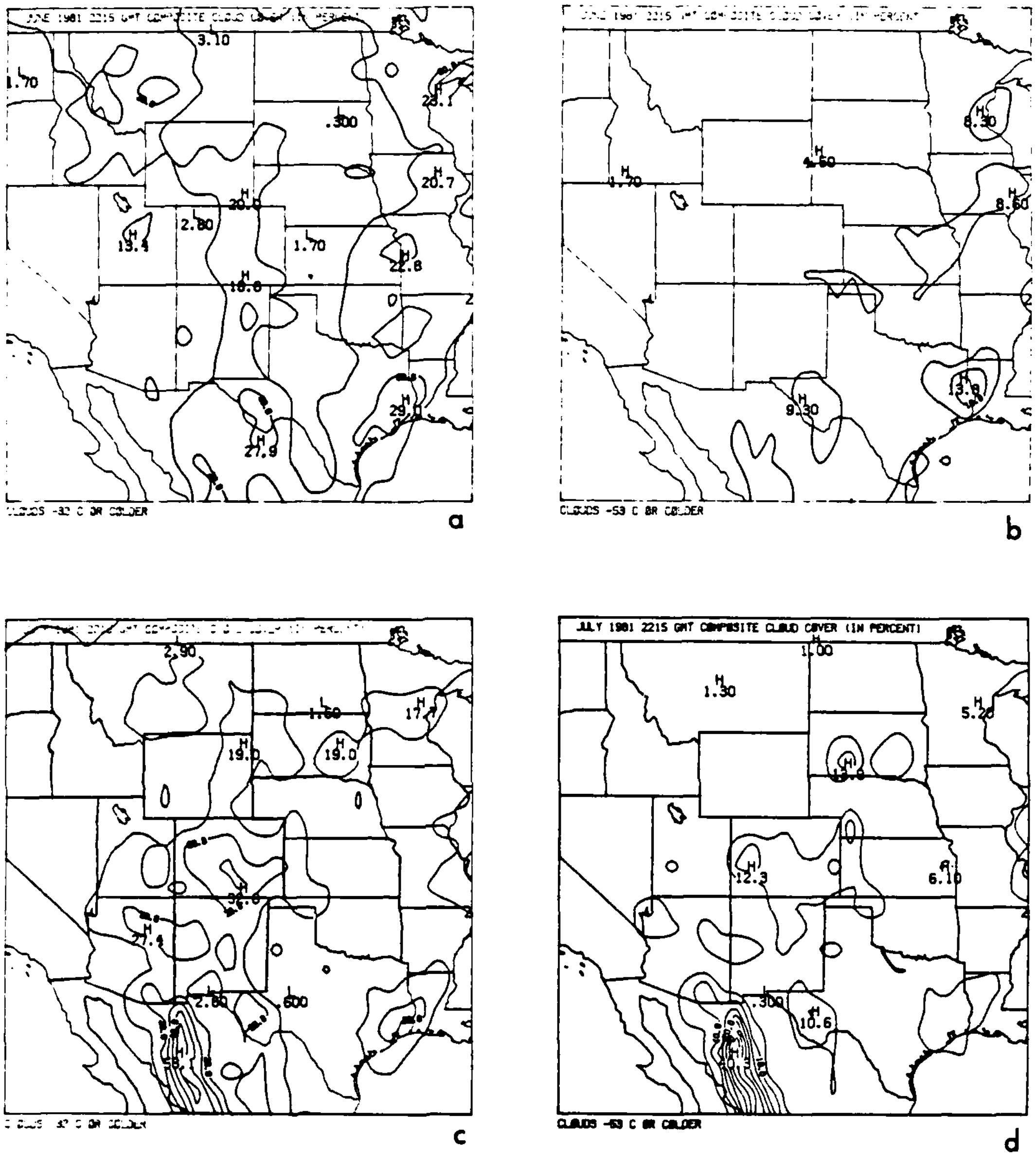

Figure 11 Average cloud cover over a 1° x 1° area in percent at 1515 MST (2215 GMT): a) June 1981, colder than -32°C; b) June 1981, colder than -53°C; c) July 1981, colder than -32°C; d) July 1981, colder than -53°C.

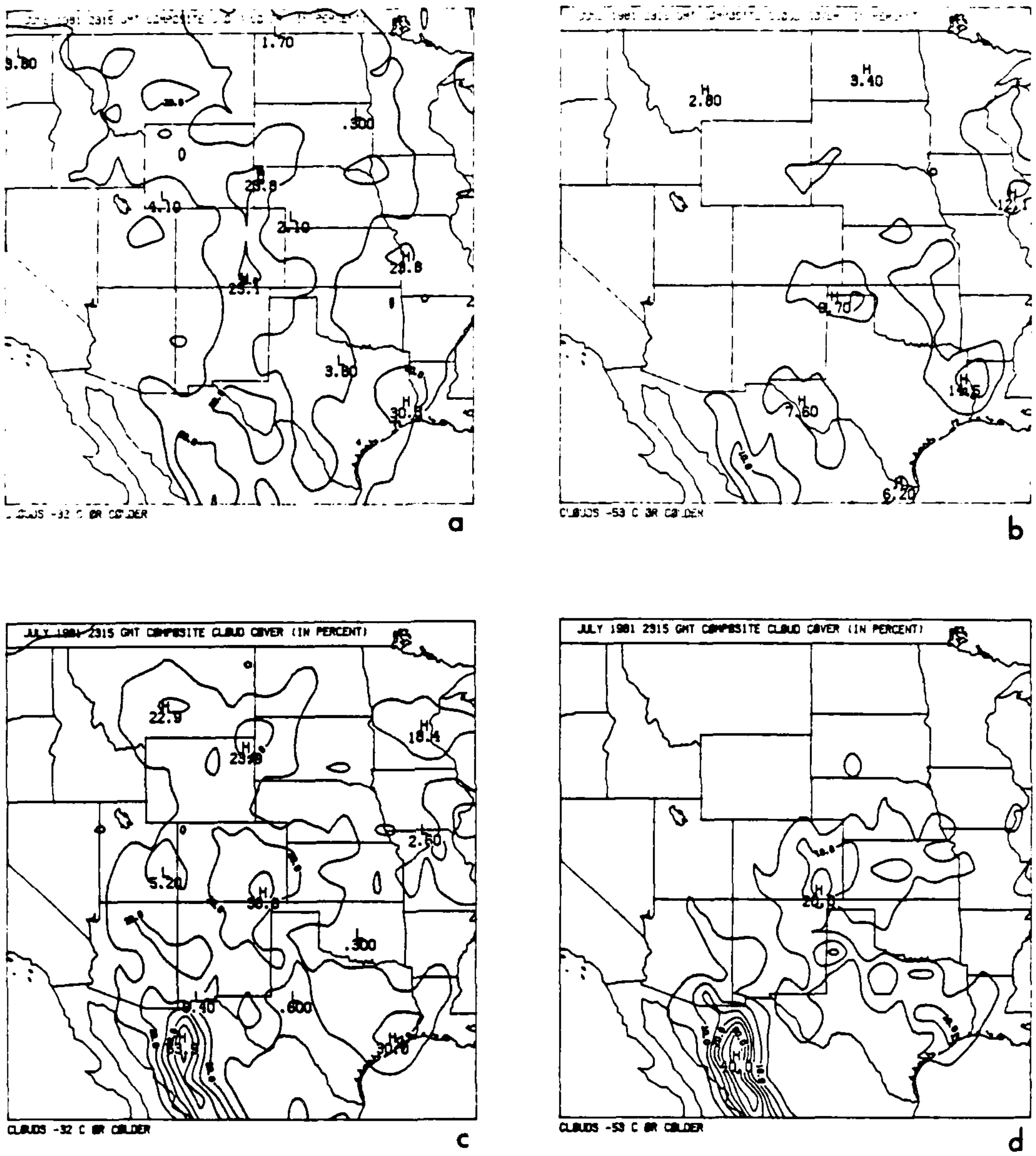

Figure 12 Average cloud cover over a 1° x 1° area in percent at 1615 MST (2315 GMT): a) June 1981, colder than -32°C; b) June 1981, colder than -53°C; c) July 1981, colder than -32°C; d) July 1981, colder than -53°C.

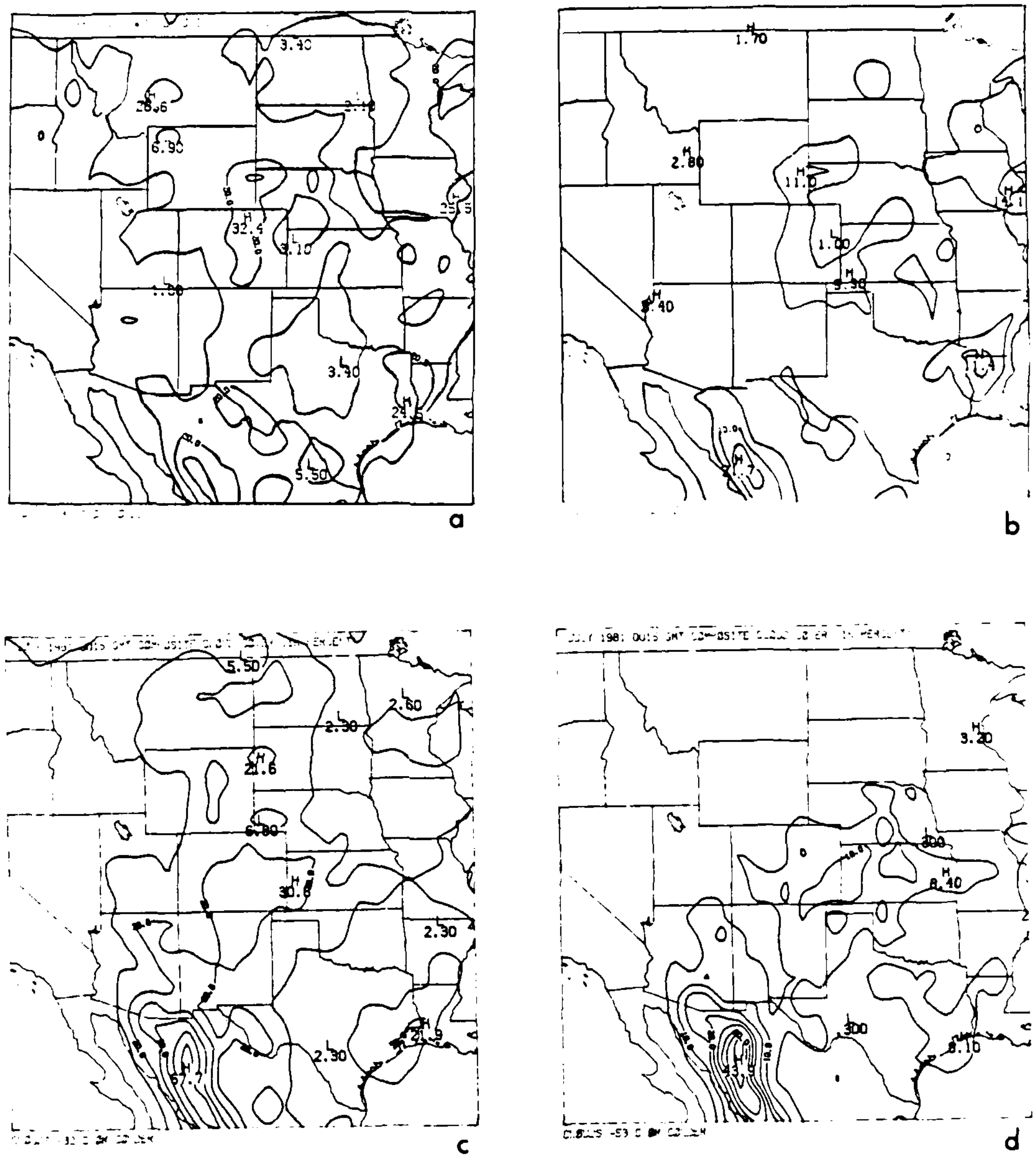

Figure 13 Average cloud cover over a 1° x 1° area in percent at 1715 MST (0015 GMT): a) June 1981, colder than -32°C; b) June 1981, colder than -53°C; c) July 1981, colder than -32°C; d) July 1981, colder than -53°C.

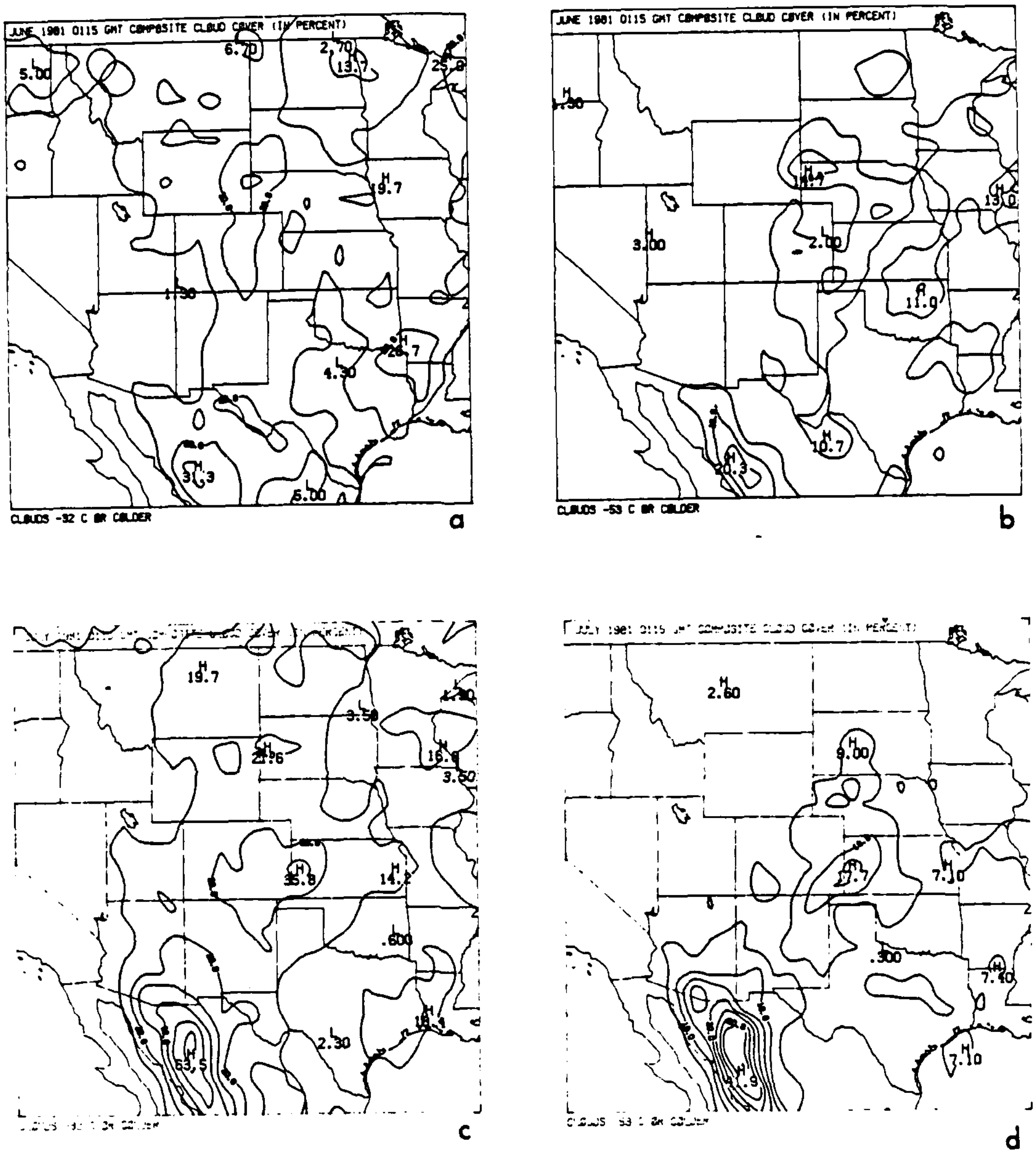

Figure 14 Average cloud cover over a 1° x 1° area in percent at 1815 MST (0115 GMT): a) June 1981, colder than -32°C; b) June 1981, colder than -53°C; c) July 1981, colder than -32°C; d) July 1981, colder than -53°C.

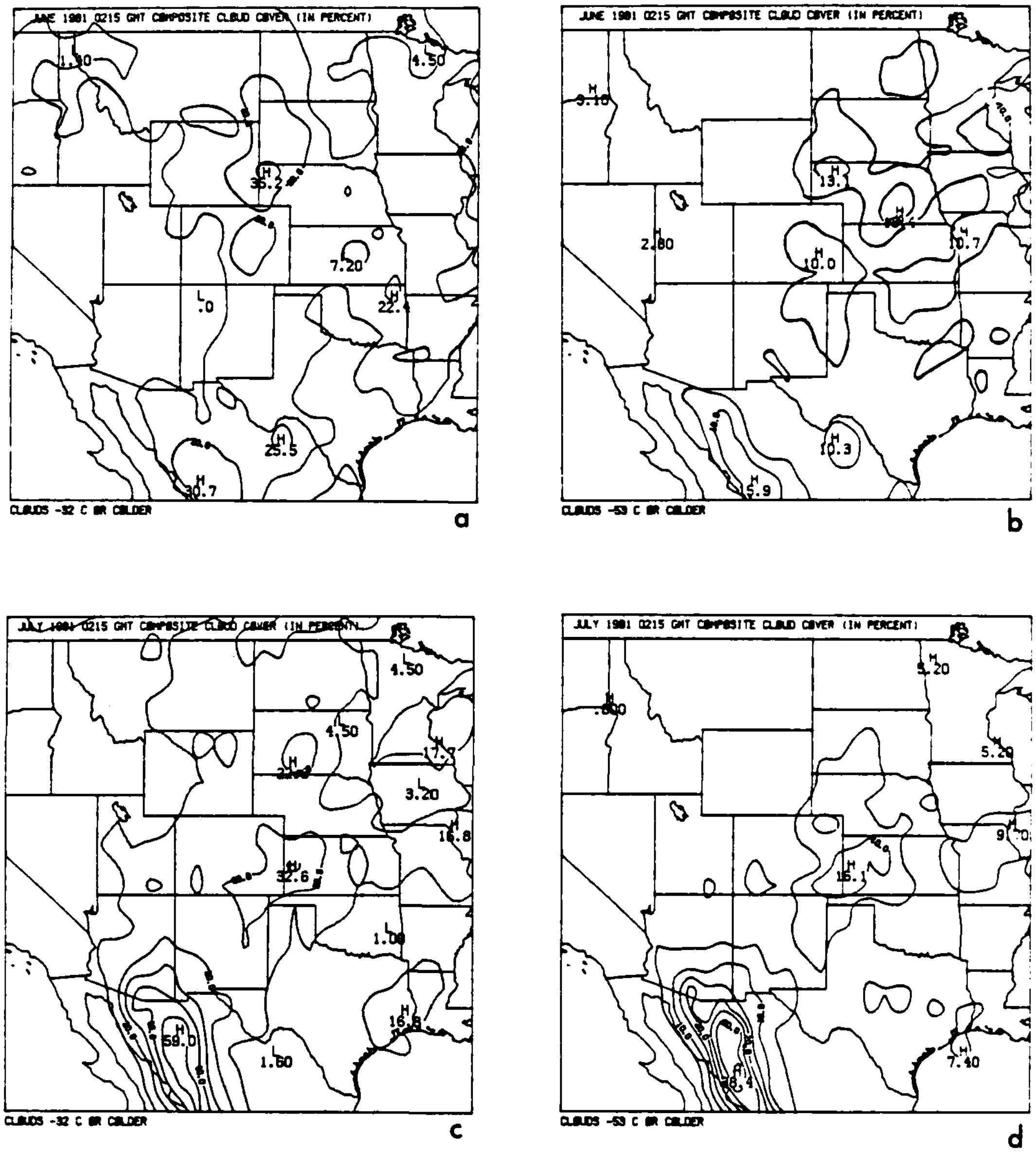

Figure 15 Average cloud cover over a 1° x 1° area in percent at 1915 MST (0215 GMT): a) June 1981, colder than -32°C; b) June 1981, colder than -53°C; c) July 1981, colder than -32°C; d) July 1981, colder than -53°C.

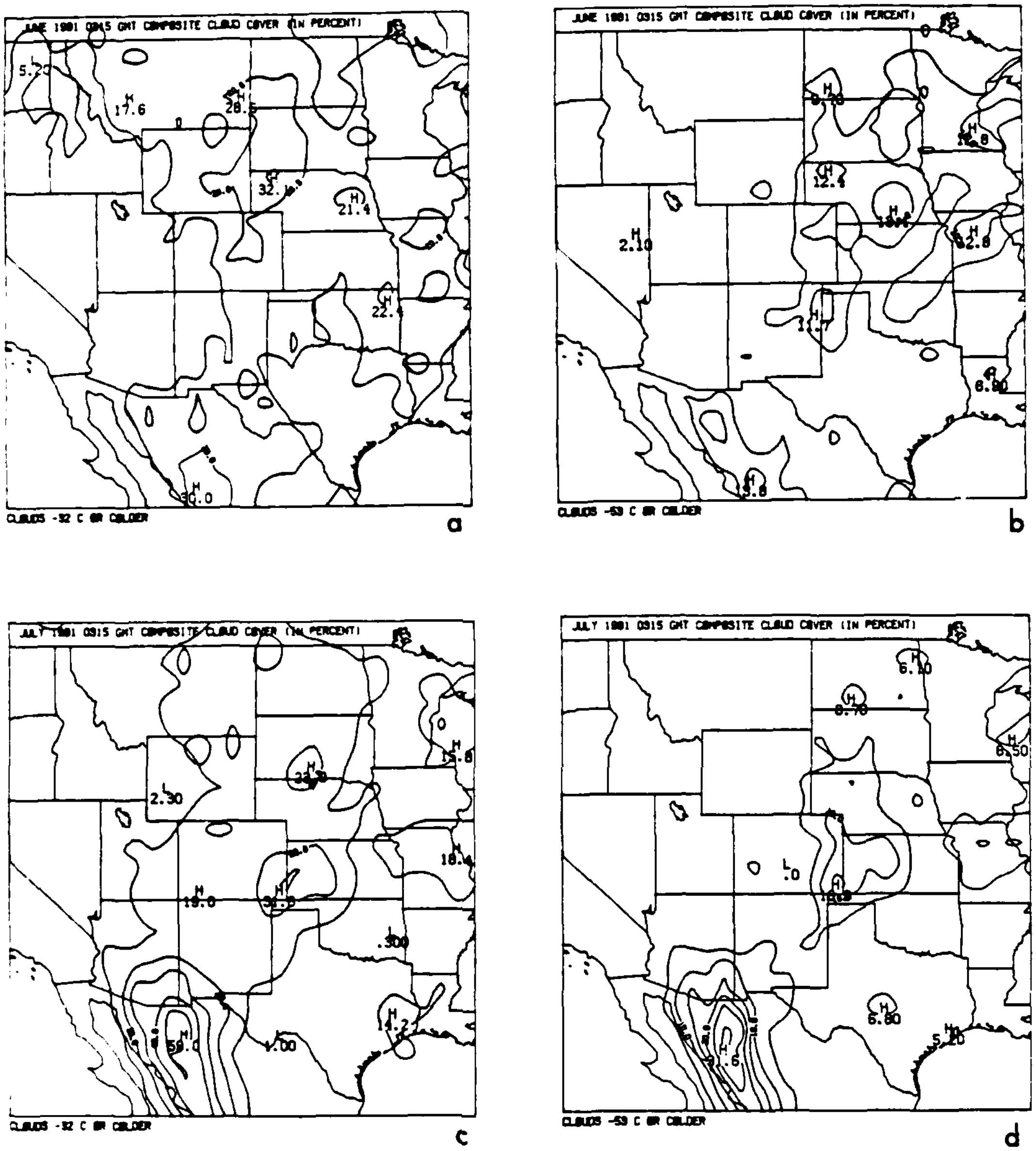

Figure 16 Average cloud cover over a 1° x 1° area in percent at 2015 MST (0315 GMT): a) June 1981, colder than -32°C; b) June 1981, colder than -53°C; c) July 1981, colder than -32°C; d) July 1981, colder than -53°C.

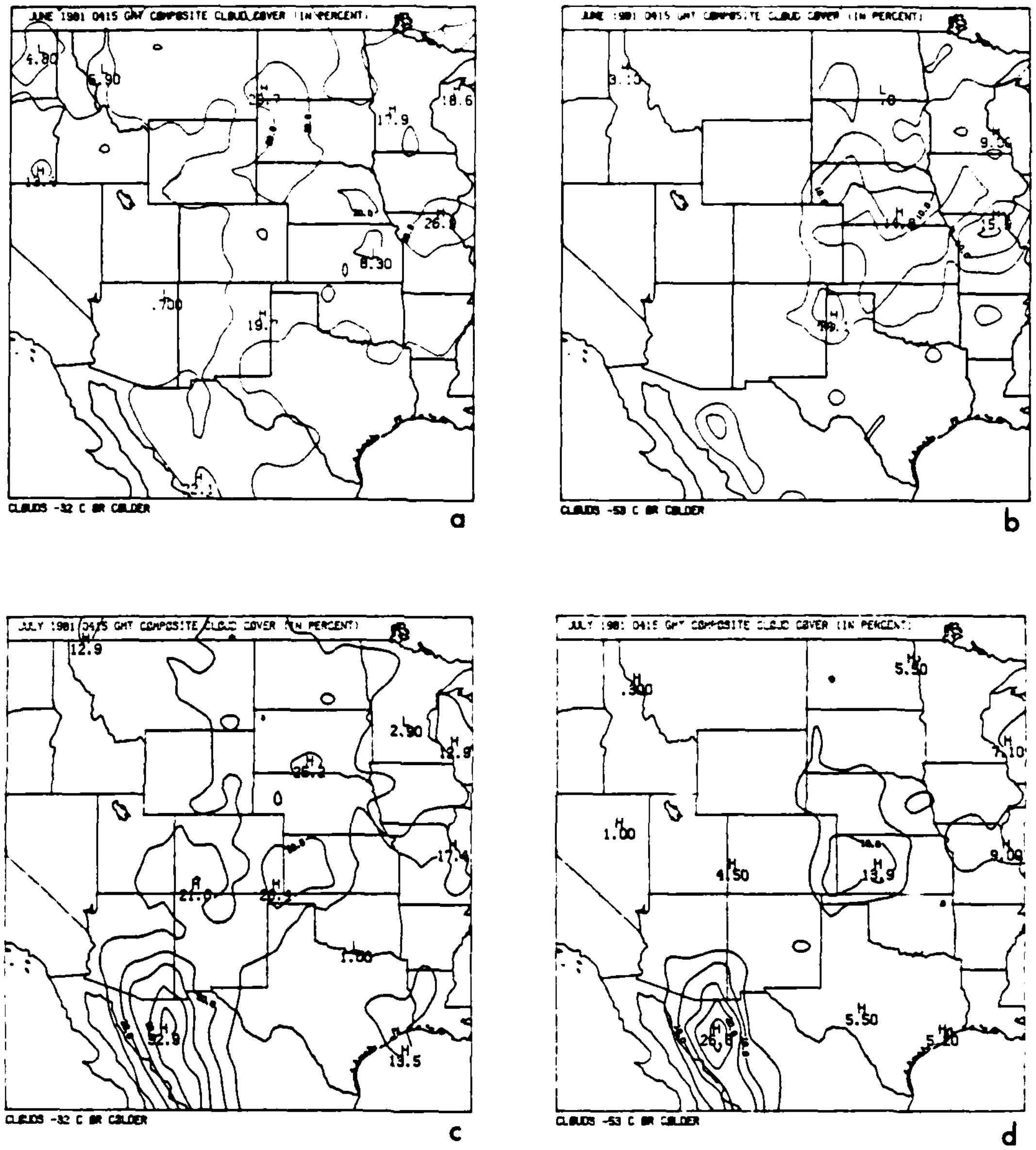

Figure 17 Average cloud cover over a 1° x 1° area in percent at 2115 MST (0415 GMT): a) June 1981, colder than -32°C; b) June 1981, colder than -53°C; c) July 1981, colder than -32°C; d) July 1981, colder than -53°C.

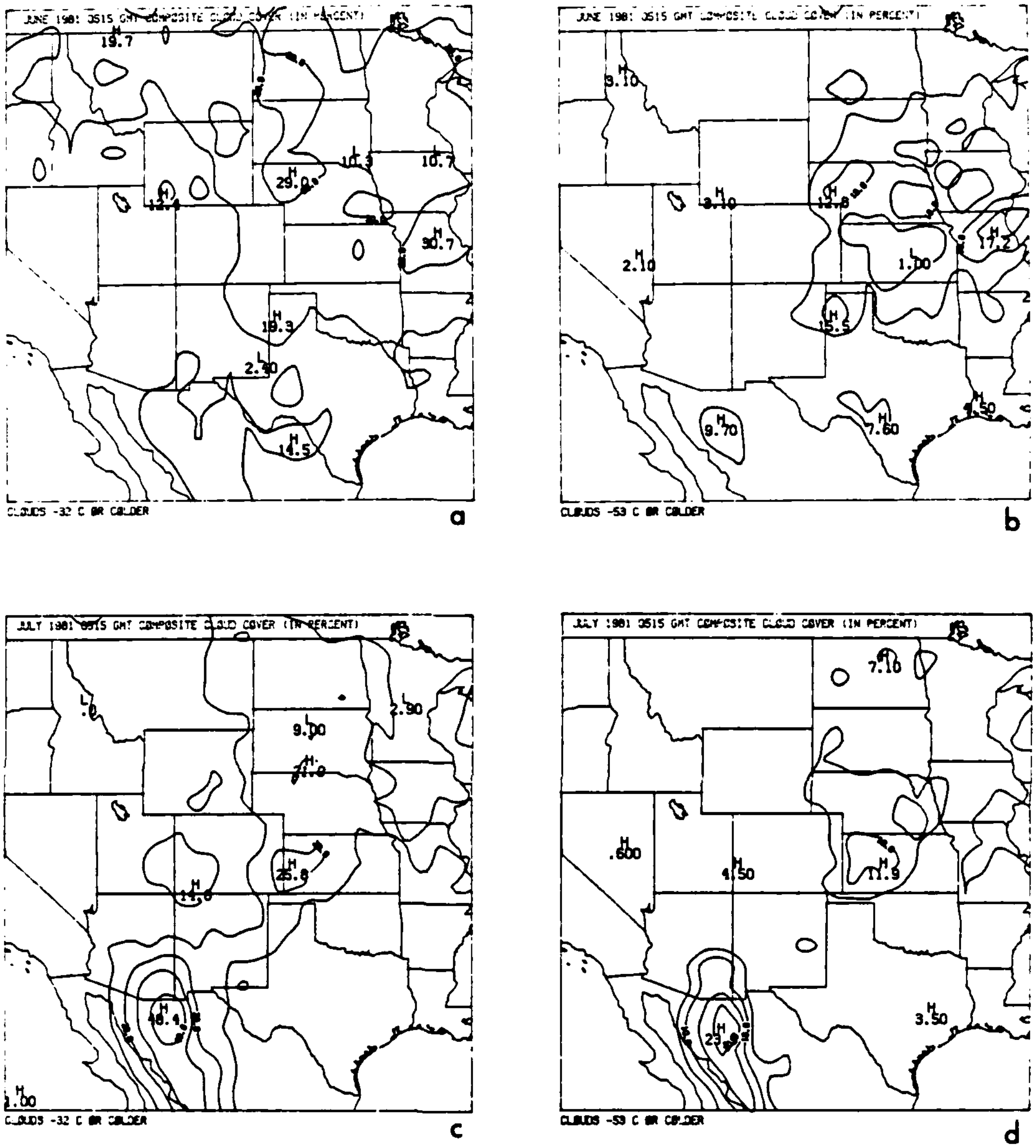

Figure 18 Average cloud cover over a 1° x 1° area in percent at 2215 MST (0515 GMT): a) June 1981, colder than -32°C; b) June 1981, colder than -53°C; c) July 1981, colder than -32°C; d) July 1981, colder than -53°C.

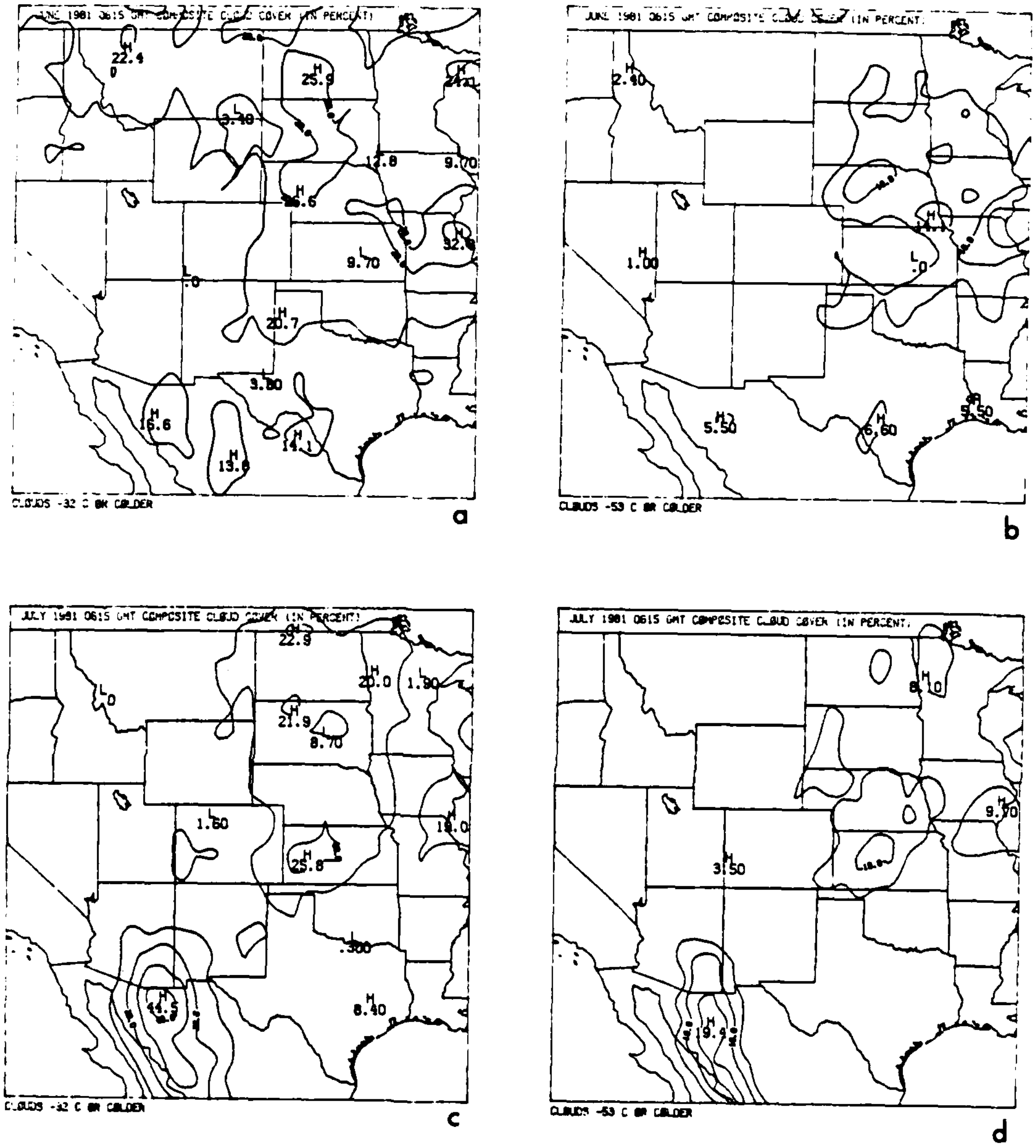

Figure 19 Average cloud cover over a 1° x 1° area in percent at 2315 MST (0615 GMT): a) June 1981, colder than -32°C; b) June 1981, colder than -53°C; c) July 1981, colder than -32°C; d) July 1981, colder than -53°C.

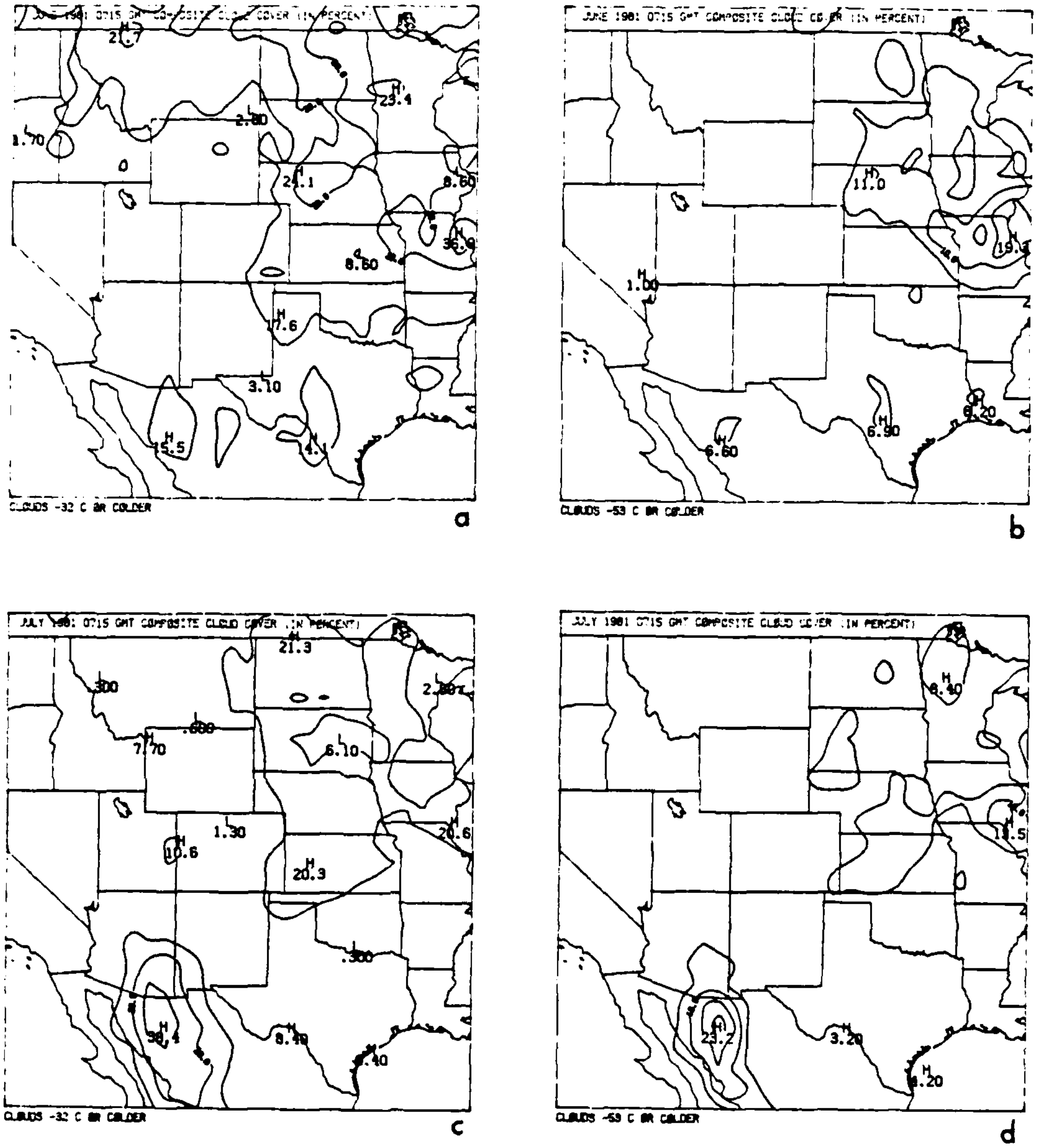

Figure 20 Average cloud cover over a 1° x 1° area in percent at 0015 MST (0715 GMT): a) June 1981, colder than -32°C; b) June 1981, colder than -53°C; c) July 1981, colder than -32°C; d) July 1981, colder than -53°C.

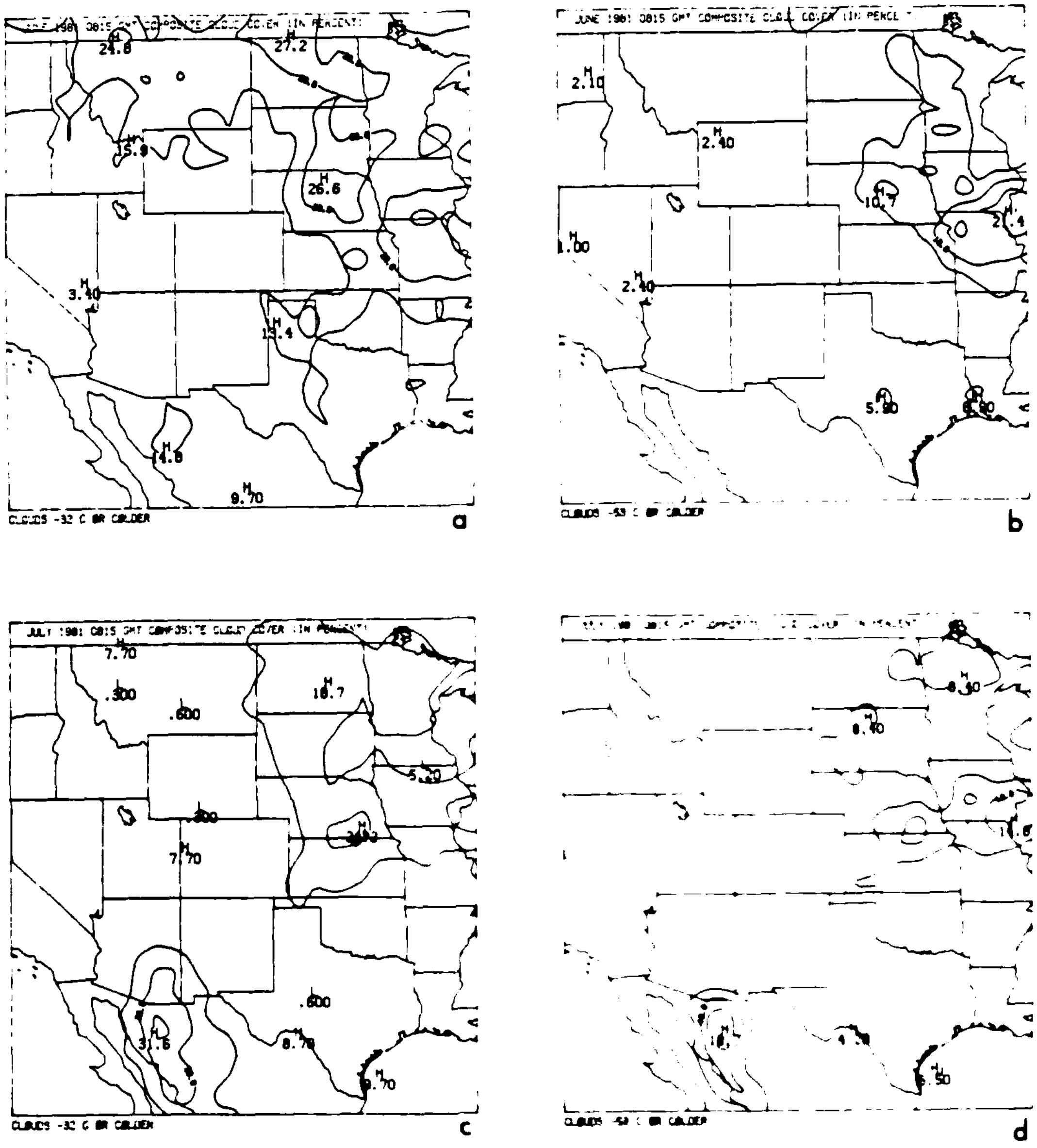

Figure 21 Average cloud cover over a 1° x 1° area in percent at 0115 MST (0815 GMT): a) June 1981, colder than -32°C; b) June 1981, colder than -53°C; c) July 1981, colder than -32°C; d) July 1981, colder than -53°C.

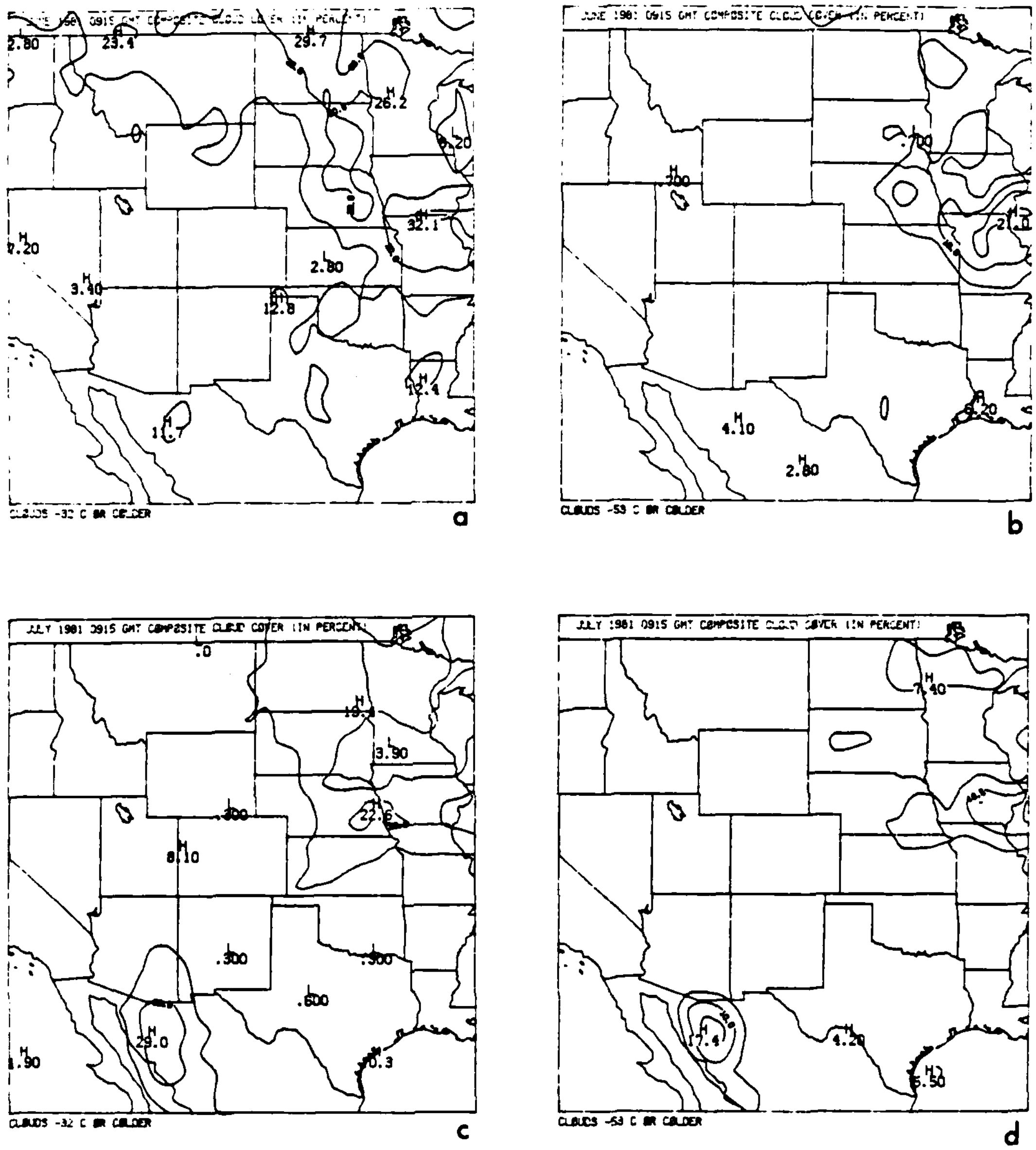

Figure 22 Average cloud cover over a 1° x 1° area in percent at 0215 MST (0915 GMT): a) June 1981, colder than -32°C; b) June 1981, colder than -53°C; c) July 1981, colder than -32°C; d) July 1981, colder than -53°C.

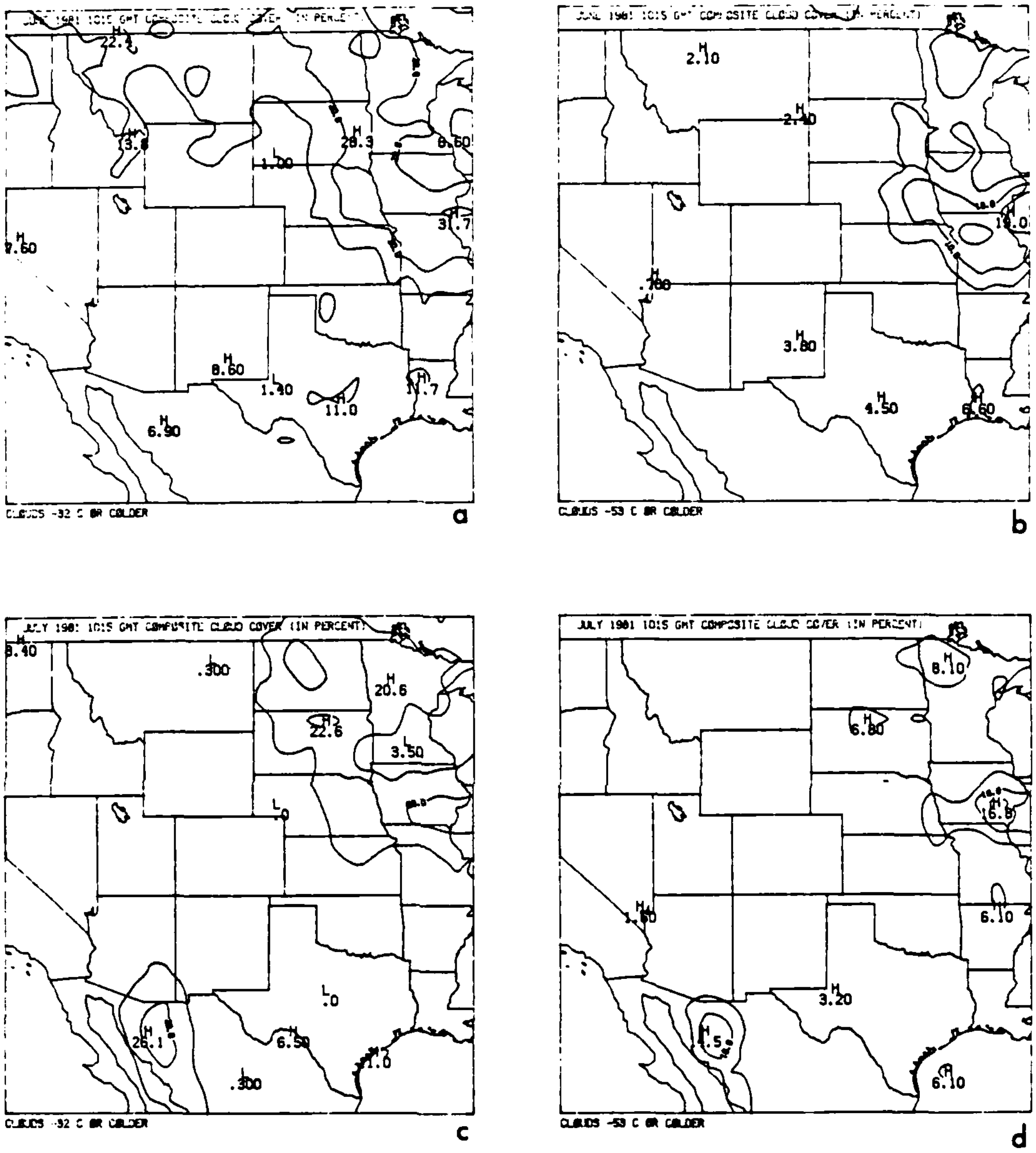

Figure 23 Average cloud cover over a 1° x 1° area in percent at 0315 MST (1015 GMT): a) June 1981, colder than -32°C; b) June 1981, colder than -53°C; c) July 1981, colder than -32°C; d) July 1981, colder than -53°C.

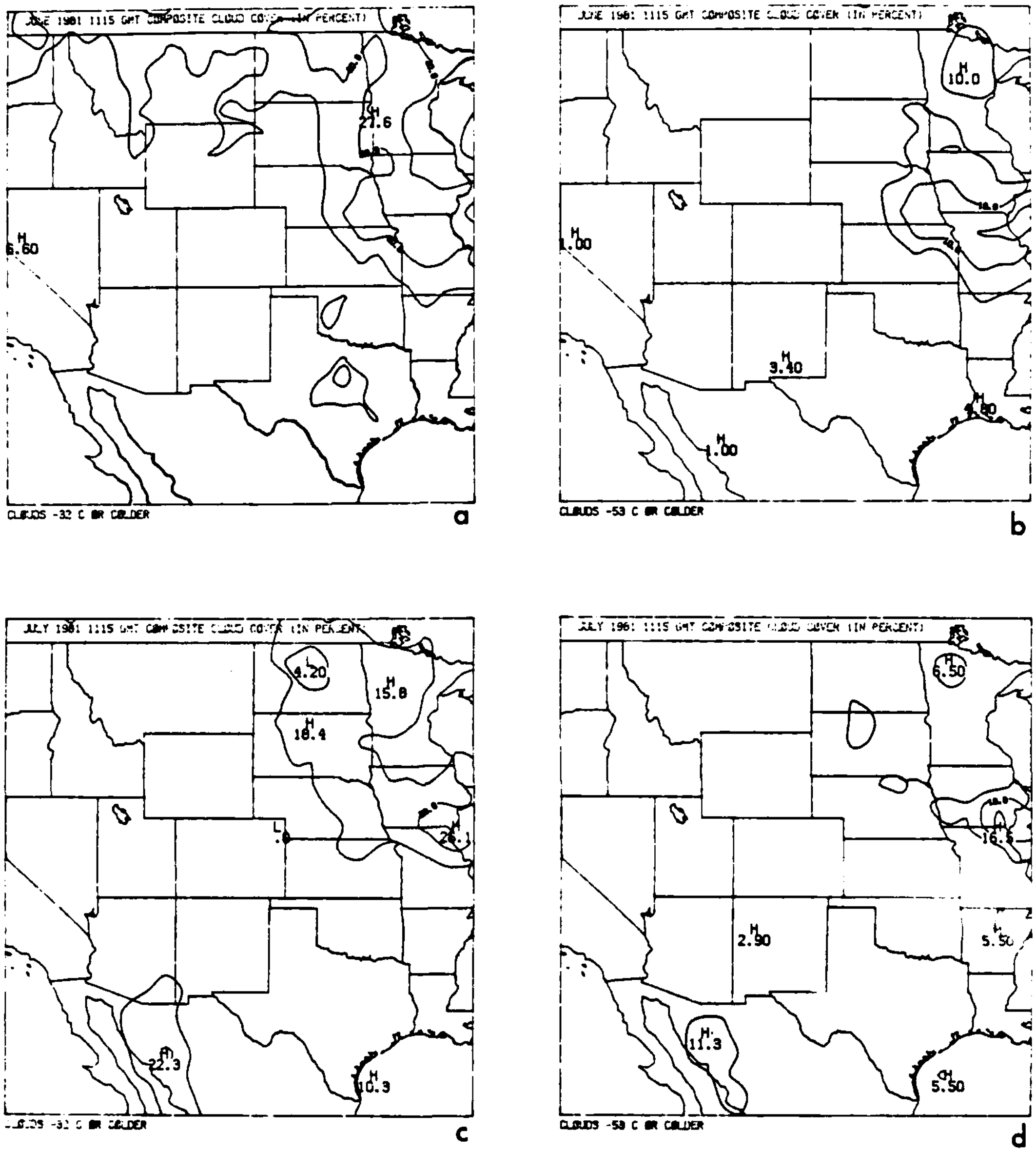

Figure 24 Average cloud cover over a 1° x 1° area in percent at 0415 MST (1115 GMT): a) June 1981, colder than -32°C; b) June 1981, colder than -53°C; c) July 1981, colder than -32°C; d) July 1981, colder than -53°C.

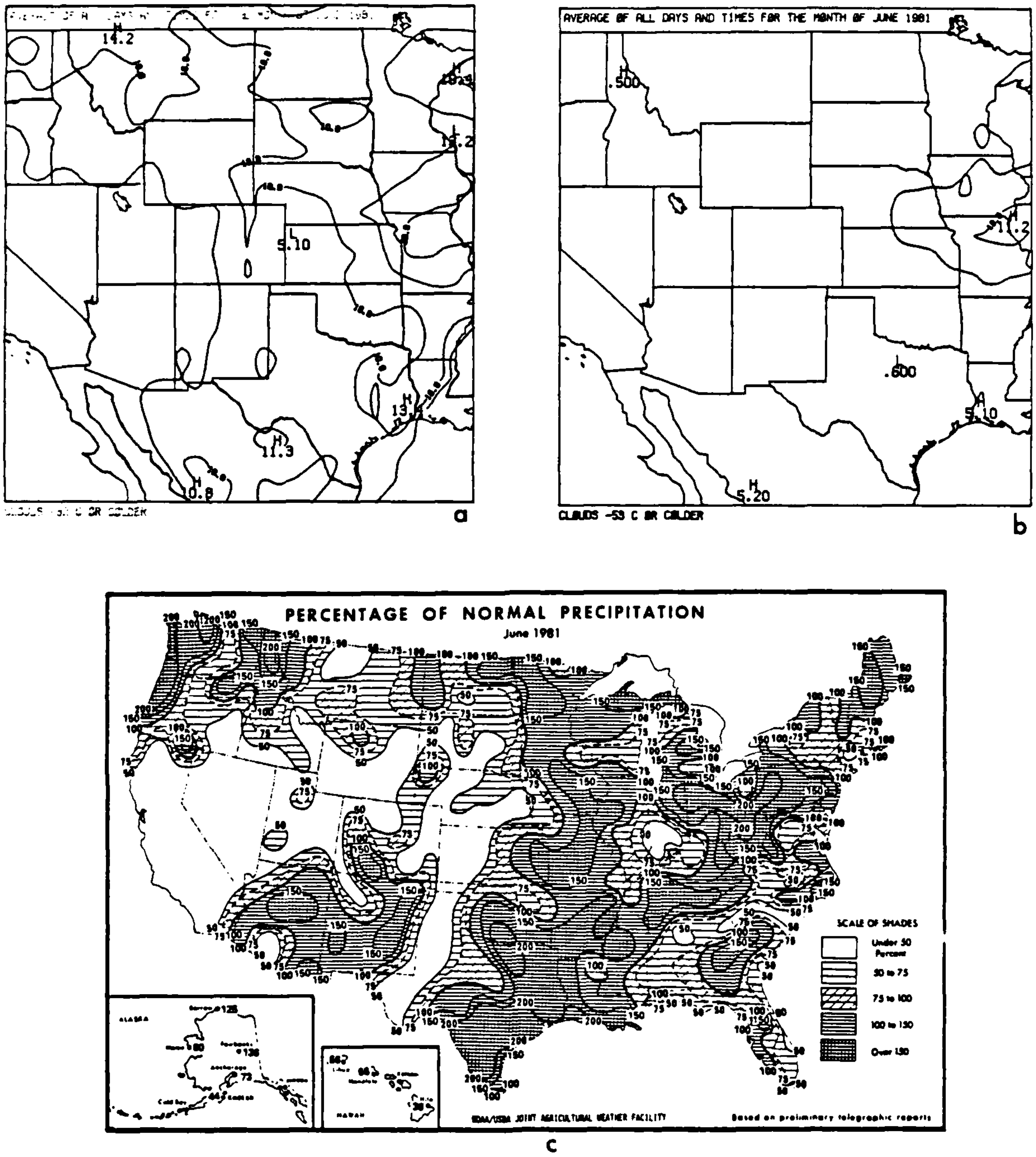

Figure 25 Overall average cloud cover for June 1981: a) colder than -32°C; b) colder than -53°C; c) precipitation expressed as a percentage of normal for June 1981 (from Ludlam, 1981a).

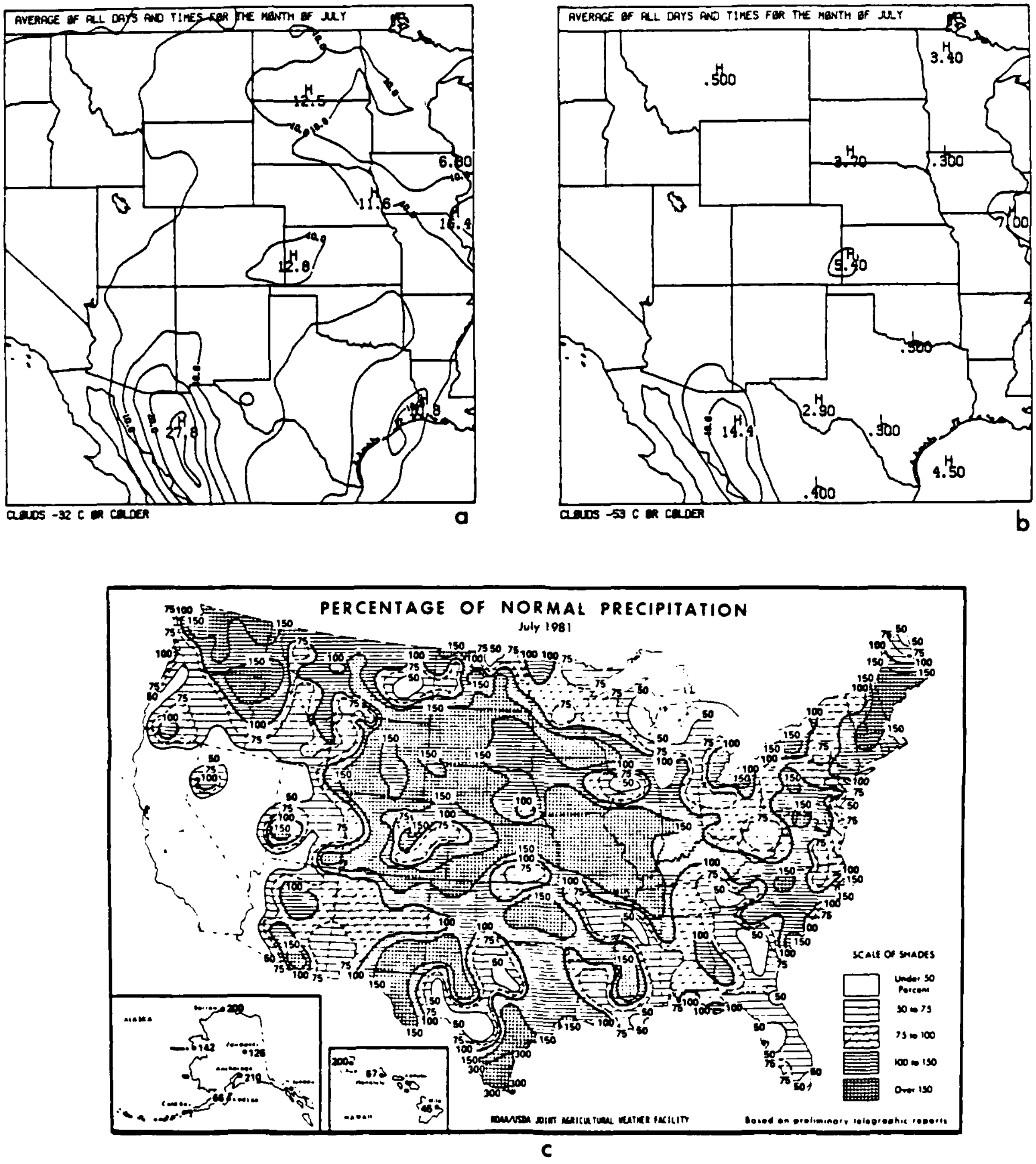

Figure 26 Overall average cloud cover for July 1981: a) colder than -32°C; b) colder than -53°C; c) precipitation expressed as a percentage of normal for July 1981 (from Ludlam, 1981b).

D. Concurrence with Previous Research

The mountain areas where clouds frequently develop (discussed in section 3B) have been noted in other cloud compositing studies, including those referenced by Klitch et al. (1982) as well as a study of radar data by Henz (1973). The "moisture bridge" from Mexico studied by Tucker in Reiter et al. (1983) was also discussed previously.

Reiter and Tang (1984) demonstrated a diurnal plateau wind circulation over and in the vicinity of the Rocky Mountains/Great Basin. In general, the cloud coverage fields agree with the locations of their PBL low pressure systems. However, the precipitation anomalies of the 1981 season (see Section 2C) and the fact that more moisture available further east leads to higher cloud frequencies there complicates the comparison between these two studies.

4. Conclusion

The hourly average cloud cover fields for June and July 1981, depict the diurnal cycle of mountain induced convection. Certain mountain locations, consistent with those in satellite climatologies for other seasons, frequently favor the development of convective storms. A diurnally modulated center of high, frequent cloud coverage along the Mexican Sierra Madre Occidental appears instrumental in providing upper air moisture and instability that allows mountain induced convection to blossom into strong storms. Overall average cloud cover fields concur with the observed precipitation anomalies for 1981.

Reducing the satellite data to compact arrays of cloud coverage values saves a great deal of computing resources in a compositing study. However, manual digitization is labor intensive, so economy over computer analysis of more dense digital fields was not achieved. When digital data are not available, careful manual digitization of photographs can provide a fine data set for climatological research. An automated method of data reduction, such as a photodigitizer used by Kelly (1983), could reduce labor costs, making this method less expensive than those that composite higher resolution digital data.

5. Acknowledgments

Ray McAnelly and Shuhua Zhang assisted with manual digitization and data entry. This research was supported by Air Force Office of Scientific Research, Research Grant No. AFOSR 82-0162. The United States Government is authorized to reproduce and distribute reprints for Governmental purposes notwithstanding any copyright notation thereon.

References

Clark, J. Dane, ed., 1983: GOES user's guide. U.S. Department of Commerce, NOAA, National Environmental Satellite Data and Information Service.

Henz, J.F., 1973: Characteristics of severe thunderstorms on Colorado's high plains. Proc. Eighth Conf. on Severe Local Storms, Denver, Amer. Meteorol. Soc., 96-103.

Kelly, F.P., 1983: An extreme event forecast guidance method using satellite cumulus climatologies. Masters Thesis, Dept. Atmos. Sci., Colorado State University, Fort Collins, CO. 107 p.

Klitch, Marjorie A. and Thomas H. Vonder Haar, 1982: Compositing digital satellite data to detect regions of orographically induced convection on the northern high plains. Atmospheric Science Paper No. 351, Colorado State University, Dept. Atmos. Sci., Fort Collins, CO. 87 p.

Klitch, Marjorie A., John F. Weaver, Frank P. Kelly and Thomas H. Vonder Haar, 1985: Convective cloud climatologies constructed from satellite imagery. Mon. Wea. Rev., 113(3): 326-337.

Ludlam, David M., 1981a: Weatherwatch. Weatherwise, 181-187.

Ludlam, David M., 1981b: Weatherwatch. Weatherwise, 228-235.

Philip, C.B., 1979: Observations of progressive convective interactions from the Rocky Mountain slopes to the plains. Atmospheric Science Paper No. 326, Dept. Atmos. Sci., Colorado State University, Fort Collins, CO. 100 p.

Reiter, Elmar R., John D. Sheaffer, Donna F. Tucker, Ray L. McAnelly, Marjorie A. Klitch, W.L. Cotton and Maocang Tang, 1983: Effects of mountain ranges on mesoscale systems development. Annual Scientific Report to U.S. Air Force Office of Scientific Research, Grant No. AFOSR 82-0162. 123 p.

Reiter, Elmar R. and Maocang Tang, 1984: Plateau effects on diurnal circulation patterns. Mon. Wea. Rev., 112(4): 638-651.

Weaver, J.F. and F. Kelly, 1982: A mesoscale, climatologically-based forecast technique for Colorado. Proc. Ninth Conf. on Weather Forecasting and Analysis, Seattle, Amer. Meteorol., Soc., 277-280.

APPENDIX B

Meso-β-scale Characteristics of the
Meso-α-scale Convective Complex

by

Ray L. McAnelly and William R. Cotton

Meso-β-scale Characteristics of the Meso-α-scale Convective Complex

R.L. McAnelly and W.R. Cotton

Colorado State University
Department of Atmospheric Science
Fort Collins, CO 80523

November, 198~~4~~5

Submitted to Monthly Weather Review
November, 198~~4~~5

ABSTRACT

A variety of meso-β-scale (20–200 km, < 6 h) temporal and spatial characteristics associated with the life-cycle of the Meso-α-scale (200–2000 km, > 6 h) Convective Complex (MCC) are described. The analysis is based on a typical episode of MCCs in the central United States. Thunderstorms in the MCC are generally well-organized into meso-β-scale convective features. Each MCC is typically preceded by several of these meso-β convective clusters or bands, which tend to be aligned along linear meso-α-scale features such as the eastern slope of the Rockies and thermodynamic discontinuities evident in hourly surface or satellite data. The intense development of the MCC involves the growth, merger and interaction of those meso-β convective features located nearest the intersection of the meso-α features along which they are aligned. Throughout the mature phase of the MCC, multiple meso-β convective components persist within the more uniform meso-α cloud shield as expanding regions of more stratiform anvil precipitation develop. The decay of the system is marked by the weakening and difluent propagation of its meso-β convective components. Hourly precipitation data reveal a characteristic precipitation life-cycle in relation to the MCC's satellite appearance. These typical meso-β-scale characteristics offer potential tools for the short-range forecasting of MCCs and their hydrological consequences.

1. INTRODUCTION

The mid-latitude Mesoscale Convective Complex (MCC) has been identified and described by Maddox (1980) as a unique class of convection, organized on the meso-α scale (200–2000 km)[1], which accounts for much of the nocturnal precipitation and severe weather over a large portion of the central United States during the convective season. The predominantly nocturnal occurrence of thunderstorms in this area has been long established (Kincer, 1916; Means, 1944; Wallace, 1975), and previous attempts to describe their mesoscale organizational characteristics (Porter _et al_., 1955; Miller, 1972) have generally invoked the more widely recognized quasi-two-dimensional squall line conceptual model (Palmen and Newton, 1969; Lilly, 1979). However, guided by the view offered by geostationary satellite (upon which the MCC's definition is based), Maddox (1983) and Fritsch and Maddox (1981) demonstrated with composited synoptic rawinsonde data that the "average" MCC has distinctly different structural and dynamical characteristics from the squall line. The latter study used numerical model support to infer that a convectively forced mesoscale region of mean ascent in the mid-to-upper troposphere is a fundamental aspect of the MCC that explains many of its observed features.

Bosart and Sanders (1981), Maddox and Doswell (1982) and Wetzel _et al_. (1983) presented case studies of several MCC or closely related events and have further described the unique meso-α-scale structure and evolution of the MCC and its cause-effect relationship to its environment. These individual case studies and the above composite

---

[1] See Orlanski (1975) for a detailed discussion of scale terminology.

studies suggest that the continental mid-latitude MCC is in many larger-scale respects more akin to the oceanic tropical cloud cluster (Gray and Jacobsen, 1977; McBride, 1981; McBride and Zehr, 1981) than to the meso-α-scale squall line.

Various field programs have collected meso-α and smaller-scale data on many tropical cloud clusters and mid-latitude squall lines. The emerging view of the cloud cluster (Betts et al., 1976; Zipser, 1977; Houze, 1977; Leary and Houze, 1979a,b; Zipser et al., 1981; Houze et al., 1981; Johnson and Priegnitz, 1981; Gamache and Houze, 1982; Leary, 1984) emphasizes the existence of a deep mesoscale "anvil" cloud, which produces about 40% of the cluster's total rainfall. A mesoscale circulation involving mid-level inflow, weak descent beneath the anvil, and weak ascent within the anvil has been convincingly demonstrated to be as integral to the system as the embedded convective-scale circulations and precipitation, which are concentrated on the leading edge of the system. Similar meso-β-scale (20-200 km) circulations have been diagnosed in the vertical plane across mid-latitude squall lines (Newton, 1966; Sanders and Emanuel, 1977; Ogura and Chen, 1977; Ogura and Liou, 1980). With its stronger shear, however, the mid-latitude squall line is better ventilated, which may prevent the stratiform precipitation (and mesoscale ascent) behind the squall from being as extensive as in the tropical case. These mesoscale circulations have been simulated in mesoscale models (Brown, 1979; Chang et al., 1981; Fritsch and Chappell, 1980). It is believed that the mesoscale descent results from the cooling due to hydrometeor melting and evaporation, while the ascent and development of the anvil cloud is a less understood response to the convective heating (Fritsch and Maddox, 1981) or to microphysical processes (Johnson and Kriete, 1982).

Comparably detailed meso-β-scale studies of MCCs have not been done. Recent efforts to describe the internal structure of the MCC (Leary and Rappaport 1983; Rockwood _et al_., 1984) used radar, satellite and hourly precipitation data to emphasize the convective versus stratiform precipitation regimes within the MCC, using the tropical cloud cluster (Zipser, 1977; Leary and Houze, 1979a) as a comparative model. Cotton _et al_. (1983) and Wetzel _et al_. (1983) investigated various meso-β-scale aspects of an MCC within the context of its convective to meso-α-scale evolution, from its initial convective roots over the central Colorado Rockies to its early weakening stages in northeast Kansas. That case occurred within an 8-day episode during which one or more MCCs occurred each evening over the central United States.

This paper is an expanded study of that MCC episode, concentrating on various phenomenological meso-β-scale aspects of MCC evolution. The episode is briefly discussed in Section 2. The data and analysis techniques are described in Section 3. In Section 4, we describe qualitatively the meso-β-scale (in space and time) sub-structures associated with several MCCs, emphasizing a degree of commonality that expands previous conceptual models of the MCC life cycle. Quantitative hourly precipitation characteristics of the MCC are then described in Section 5, revealing a characteristic precipitation signature in relation to its satellite appearance.

2. CASES STUDIED

As evidenced by the accumulating climatological data base on MCCs [Maddox (1980, 1981); Maddox _et al_. (1982); Rodgers _et al_. (1983)], successive MCCs (and less organized mesoscale convective systems) often develop daily over a several day period when a slowly evolving large-scale circulation pattern becomes favorable for their formation. The MCCs studied here occurred within such an eight-day episode, 3-10 August 1977, in which afternoon and evening convection developed up-scale each day into one or more MCCs that persisted well into or through the night. The tracks of the mesoscale convective systems which attained MCC dimensions are shown in Fig. 1, based on the centroids of their cloud shields as seen in infrared satellite imagery at 3-h intervals. The darkened tracks indicate periods when the systems met Maddox's (1980) areal and thermal criteria for a mature MCC.

The quasi-stationary large-scale pattern which set up this episode is discussed in Cotton et al. (1983) and Wetzel et al. (1983). It basically featured a zonal polar jet along the United States/Canadian border, a quasi-stationary surface front from the Colorado plains to the Great Lakes and New England, maritime tropical southerly flow to the south of the front, and an apparent extension of a monsoonal circulation over the southwestern United States bringing a southwesterly influx of Pacific moisture over the central Rockies to the High Plains.

Several general aspects of the MCC episode can be inferred from Fig. 1. Two distinct MCC genesis regions are evident, one along the eastern slopes of the Rockies and High Plains ("western" systems), and the other further east over the more level and lower terrain of Missouri and Iowa ("eastern" systems). The MCCs tended to occur in the vicinity of, and track along, the quasi-stationary surface front mentioned above. The remnants of decayed complexes persisted for long periods (up to 3 days) as identifiable regions of loosely organized convection and anvil cloud, which occasionally reintensified into mature complexes. Except along the Gulf coast and in the southeastern states, the eight-day precipitation over the United States east of the Continental Divide was strongly dominated by these systems (see Fig. 2 of Wetzel et al., 1983).

3. DATA AND ANALYSIS METHODOLOGY

The investigation of the MCCs was carried out over the central United States region shown in Fig. 2. The analysis is based primarily on geosynchronous satellite imagery, National Weather Service radar data, conventional hourly surface observations, and hourly precipitation data, all of which provide temporal and spatial information on the meso-β scale. Except for the hourly surface observations, the techniques developed for analyzing these data are somewhat unconventional. They are discussed in this section.

a. Satellite data and analysis

The life-cycles of twelve of the episode's MCCs were quantified using infra-red (IR) satellite imagery from the Geostationary Operational Environmental Satellites positioned over the equator at 75° W and 135° W (GOES-East and GOES-West, respectively). The data consisted of nearly complete sets of half-hourly, "MB-enhanced" IR images (Clark, 1983) from both satellites. Fig. 3 illustrates the evolution of the first MCC of the episode (MCC #1) as seen in the GOES-East imagery. The enhanced features which were utilized in this study are the IR isotherms of −32 and −53°C and the light-shaded interior anvil regions that are indicative of overshooting thunderstorm activity (Clark, 1983).

In order to facilitate our investigation of the relationship of the satellite-viewed storm systems to other meteorological fields, we first re-mapped the -32 and -53°C IR contours of relevant cloud shields from approximately hourly-interval images onto standard meteorological working maps. On-the-hour GOES-East images were used when available, and if not, images at 15 or 30 minutes off the hour were re-mapped. This manual procedure was done by overlaying a 1° x 1° latitude-longitude grid onto an image (adjusting for obvious navigation errors), inspecting the path of an IR contour through a given block, and drawing its re-mapped path through the corresponding 1° x 1° grid block on the working map. Such re-mapping has an estimated accuracy to within 25 km. Examples of the re-mapped cloud shields can be seen for MCC #1 in Fig. 6 (compare the 0300-0900 GMT[2] mappings with the corresponding images in Fig. 3). In addition to the -32 and -53°C IR contours, areas and axes of overshooting thunderstorm activity were also drawn on the working maps.

In the analysis of the MCCs' sub-structures (Section 4), these IR maps were used for the display and interpretation of the simultaneous IR and radar fields. In the more quantitative analysis of the MCCs' hourly precipitation characteristics (Section 5), where an objectively defined MCC life-cycle was required, we used the working maps to derive an hourly record of the cloud-top IR areas colder than -32 and -53°C for each MCC. These measurements were made with a planimeter, yielding on-the-hour IR areas either directly, or by linear interpolation from off-the-hour IR maps.

Considering the errors due to navigation, re-mapping and

---

[2] Central Standard Time is 6 h earlier than the universal time convention used throughout this paper.

planimetric measurement, the accuracy of the IR area is estimated to range from within 20% for the smallest areas considered (~ 5,000 km^2) to within 5% for large anvils (> 100,000 km^2). Of greater impact than those measurement inaccuracies was the subjective determination of what constituted an MCC's anvil in the first place. Usually, it was unambigously defined by a single contiguous -53°C IR area and a larger, enveloping -32°C IR area. A typical example is illustrated in Fig. 2 by the MCC depicted over eastern Iowa and northern Illinois. Occasionally, however, multiple IR areas were summed if each was a significant, discrete component of the mesoscale system that was within 2 h (before or after) of being a part of the organized, contiguous IR area (as with the two large -53°C areas in Fig. 3f). Slightly more problematic were those storm systems which appeared in satellite imagery to undergo a growth and decay cycle characteristic of a quasi-circular MCC, but which were contiguous during part of their life-cycle with adjacent cold anvil cloud shields that appeared to be produced independently and which never became organized parts of the systems. In such a case, a relative warm axis could be found in the cloud shield separating the quasi-circular MCC from its contiguous, "non-MCC" appendage. The most extreme case of such a subjective boundary determination is illustrated in Fig. 2, where the MCC over the Texas panhandle was deemed to be distinct from the adjacent activity in southwest Kansas and the Oklahoma panhandle. For the limited quantitative applications that the IR areal measurements were used, these errors and subjective decisions are not significant.

Based on the hourly IR measurements, we define the mature MCC to "start" when the contiguous area within the -53°C IR isotherm first exceeds 50,000 km^2, to reach its "maximum" when this area attains its largest size, and to "end" when this area first becomes less than 50,000 km^2 (at 02, 10 and 16 GMT, respectively, for MCC #1 in Fig. 3). The mature duration is defined as the time elapsed from "start" to "end". Although Maddox (1980) used both -32 and -53°C IR areas as criteria for these MCC benchmarks, our analysis of hourly precipitation data shows that the colder area better correlates with the active rainfall rate and appears to be the core of the MCC, whereas the -32°C area is largely inactive anvil debris. Therefore, we have based these definitions solely on the -53°C area.

In addition to these areally-defined points in the life-cycle, a meso-α "cellular" stage is defined more subjectively as the period after the system has unified and during which the -53°C IR contour is relatively smooth and circular. In Fig. 3, for instance, contrast the smooth "cellular" appearance at 07 and 09 GMT with the more jagged -53°C appendages before, and the more ragged -53°C edges afterward. Within the "cellular" stage, the time of maximum "overshooting-top" activity is defined subjectively as when the light-shaded anvil interior reaches its largest and coldest extent (07 GMT in Fig. 3). These points in the life-cycle were determined to the nearest hour. Considering the errors in the areal IR measurements and the subjective decisions regarding the definition of an MCC's anvil, we believe the timing of the life-cycle stages would be within an hour of any independent attempts to define them from the satellite imagery.

IR-defined life-cycles were determined in this manner for the twelve MCCs listed in Table 1. The system numbers are those assigned by Wetzel _et al_. (1983) and refer to the chronologically numbered storm tracks in Fig. 1. Note that system #5 had two mature periods, first as a western MCC (#5a), and again as an eastern MCC when it re-intensified in eastern Iowa (#5b). Similarly, system #9/10, depicted in Fig. 1 as a merging track in Iowa, developed between and adjoined the pre-existing western MCC #10 and eastern MCC #9. The MCCs in the episode that are not listed in Table 1 were eliminated because of a less intense and more unorganized appearance in IR data. For the purposes of the precipitation analysis discussed in Section 5, the twelve MCCs in Table 1 were stratified according to genesis region and maximum anvil size into four groups of three similar systems each: western large (W-L), western small (W-S), eastern large (E-L) and eastern small (E-S) MCCs. The W-L and E-L MCCs had maximum anvil areas about 2.5 times larger, and had durations longer, than their smaller counterparts.

b. Radar data and analysis

In Section 4, the radar echo structures of the large MCCs listed in Table 1 are described, based on data from the radar network depicted in Fig. 2. Radar plan-position indicator (PPI) film documenting most of the MCC cases was acquired for six National Weather Service (NWS) WSR-57 (10-cm) radar sites from eastern Colorado to Iowa. Radar observation logs for the entire episode from these six sites and an additional three NWS sites (in Nebraska, Oklahoma and Missouri) were also obtained. Other NWS radar data consisted of operational hourly radar depiction maps (which in 1977 were composited manually from the radar observations) and their crudely digitized counterparts, Manually Digitized Radar (MDR) maps (Moore et al., 1974). Supplementing these NWS radar data were 5-min digitized mappings of composite PPIs and echo-top PPIs (Schroeder and Klazura, 1978), processed from 5-cm radar volume scans collected at Goodland, Kansas, under the Bureau of

Reclamation's High Plains Experiment (HIPLEX).

In order to analyze the radar echo structure associated with the MCC's IR cloud shield, we produced hourly working maps of areally composited radar data. Each map was constructed using data at about 25 minutes after the hour, near the time that NWS hourly radar observations were made. The outlines of all echoes on the NWS PPI film and the HIPLEX PPIs were re-mapped in a manner analogous to re-mapping the IR satellite data, except that polar grid references were used. When possible (e.g., with the HIPLEX digital mappings), higher intensity reflectivity contours were also re-mapped. With only two of the six NWS radars having Video Integrator Processor (VIP) intensity displays, however, such quantitative intensity resolution was severely limited. On the other hand, the temporal resolution of the PPI film was generally excellent (~ 5 min), and occasional PPI pictures with reduced receiver gain revealed the stronger echoes. Thus, aided by temporal continuity, axes and embedded cells of relatively strong convection could be identified and re-mapped as well. In addition, the intensities, locations and heights of echoes that were logged on the radar observation forms were mapped onto the hourly charts, providing more inferrences of the intensity and location of particularly strong convection. For the meso-β-scale focus of this study, the positional accuracy of the radar re-mapping is adequate.

In producing and analyzing the hourly radar maps, it was evident that the strong convection was predominantly organized into meso-β-scale clusters or bands that persisted for well over an hour. Such meso-β convective features are thus the basic unit of the MCC's substructure that we describe in relation to the evolving IR cloud shield in Section

4. Each schematic meso-β echo feature depicted in the analyses (e.g., in Fig. 6) may represent almost total echo coverage, or alternatively, simply a cluster or line of discrete echoes which maintain a meso-β cohesiveness. In general, the meso-β convective features represent smaller areas of concentrated convective activity within the much larger areas of scattered thunderstorm and rainshower activity as defined by the NWS hourly radar observations. Echoes of sufficient intensity and height to warrant their entries in the radar observation logs were always located within the meso-β features. Some areas of weak echo and isolated or short-lived echoes have been omitted from the schematic structures if they had little apparent effect on the MCC's cloud shield. Hourly precipitation patterns, as derived from the precipitation network depicted in Fig. 2 (discussed in Section 3c), are also consistent with the schematic meso-β features.

Because of the wide variety of convective organization within these meso-β features, we term them loosely as meso-β-scale convective "clusters", "lines", "bands" or simply "components". Their more detailed documentation is beyond the meso-β to α-scale scope of this paper. Convective structures seen within them on the PPI film included many of those reviewed by Kessler (1982), ranging from rather unorganized multi-cell systems to well-defined meso-β squall-lines, and approaching isolated supercell-type systems. Similarly, stratiform echo in and around the meso-β features ranged in amount from none to very extensive, and it was seen to extend from more intense convective echo in any or all directions. The limiting quality of the radar data prevented any quantification of the echo into convective versus stratiform types (e.g., Houze, 1977).

c. Hourly precipitation data and composite analysis methodology

The description of the temporal evolution of the MCC's precipitation characteristics (Section 5) is based on an analysis of hourly precipitation data[3], recorded by the network depicted in Fig. 2. This hydrological network has a non-uniform station spacing over the area of interest, and is particularly sparse (considering convective rainfall) in the western plains. Another difficulty with these data are the use of two types of recording gages, with increments of 0.25 mm and 2.5 mm, respectively (traces are not recorded). Thus, light precipitation ($\lesssim$ 2.5 mm/h) that is characteristic of much of an MCC's area and lifetime would be recorded much less accurately (or even go undetected) with the 2.5-mm gages than with the 0.25-mm gages. For instance, an MCC's precipitation field centered over northwest Wisconsin would be recorded much differently than an identical field centered over southwest Missouri. For areas larger than such local clusters of predominantly one gage type, however, the mix of gage types is relatively stable over the network. Thus, considering the long duration of an MCC relative to the hourly sampling period, and the large area affected by its time-integrated rainfall, the network provides data that adequately describe its meso-β-scale rainfall characteristics. It is the inability of the network to representatively sample convective-scale rainfall that has prompted us to adopt a composite analysis approach, which smooths out some of the finer-scale variability in the storm systems. In this approach, the hourly precipitation information of twelve MCCs are combined into the four

---

[3] "Hourly Precipitation Data" is published monthly by the National Climatic Center, NOAA/EDIS, Asheville, NC 28801.

composite categories shown in Table 1.

The procedure for quantifying the hourly rainfall data for the individual MCCs consisted first of plotting hourly reports for each hour onto the corresponding map of re-mapped -32 and -53°C IR isotherms. Contiguous areas of hourly rainfall were then enclosed into precipitation envelopes, where their boundaries were carefully drawn approximately equidistant between stations reporting measurable rainfall and those stations outside the envelopes reporting no rainfall. Figure 2 includes examples of such hourly rainfall envelopes. Usually, they matched well with the radar-identified meso-β convective features presented in Section 4. An envelope was considered to be associated with the MCC if it was contiguous with the -32°C IR area at either the beginning or end of the hourly period. In general, there was little significant "non-MCC precipitation" anywhere near an MCC, making this determination fairly straightforward. Each "MCC precipitation" envelope was further classified as "core precipitation" if it was approximately half or more within the -53°C IR area at both the beginning and end of the hour, or as "peripheral precipitation" if it did not meet those criteria.

With the MCC-related precipitation thus indentified and classified, the next step in the analysis was to derive hourly rainfall depths, areas and volumes. The area of each envelope was measured with a planimeter, and all rainfall values within it were arithmetically averaged to give a mean hourly rainfall depth. An hourly rainfall volume for each envelope was computed as the product of the area and mean depth (see examples in Fig. 2). All of the 0.25-mm and 2.5-mm gage-type reports within a given envelope were averaged together because of no known suitable way to treat them as separate samples or to adjust them to a consistent single sample. In general, the average of the 2.5-mm-type reports for a given envelope was larger than the average of the 0.25-mm-type reports, because of the presence of reports < 2.5 mm in the latter sample. Thus, the portion of the envelope area contributed by the small 0.25-mm reports could be significant, and the average precipitation depth could be significantly lowered by their presence. However, the resultant rainfall volume is not significantly altered by their presence: a larger area times a smaller mean depth yields a similar volume.

For each hour of an individual MCC, multiple envelopes were combined to give a "core" precipitation area (A) and volume (V) and a "peripheral" A and V, and these were added to give a "total" A and V. Partially due to the inadequate sampling of convective-scale precipitation, the hourly values of A and V showed considerable temporal variability. To reduce some of this "noise", filtered hourly values of A and V were computed for core, peripheral and total rainfall by using a 1-2-1 running average. With this filter, a smoothed value for each hour was computed by weighting the values from the previous hour, the given hour and the following hour by 25, 50 and 25%, respectively.

The composite analysis approach to this quantified precipitation information is illustrated in Fig. 4, where the timing of the IR-defined life-cycle characteristics is indicated along an hourly time axis for each MCC. In each composite category, the three individual MCCs are considered to have common composite times of "start", "maximum" and "end". Besides having common genesis regions, similar maximum IR areas and similar mature durations (Table 1), the MCCs in each category were reasonably consistent in terms of other IR-defined characteristics. These include: the durations of "start-to-maximum" and "maximum-to-end"; the timing and duration of the "cellular" appearance within the "start-maximum-end" sequence; the timing of the "overshooting-top maximum" within this sequence and also within the "cellular" period; the timing of the maximum $-32^{o}C$ IR area; and the absolute GMT times of these IR features. Thus, a realistic time scale for a composite MCC can be derived for each category. The composite's "start" is defined to occur at MCC hour 0, and its "maximum" and "end" are determined by the average "start-to-maximum" duration and average mature duration, respectively, rounded to the nearest hour. The other composite life-cycle points are similarly determined to the nearest composite hour.

The averaging methodology for deriving the composite MCCs' precipitation characteristics is based on these time scales. Each individual MCC's smoothed hourly values of rainfall area and volume, A and V, were first fitted onto its composite time scale, with the end of each hourly precipitation period coinciding with the IR-defined MCC hour. For those MCCs whose "start-to-maximum" or "maximum-to-end" durations differ from the respective composite duration (2-h maximum difference), the fitting of the individual MCC measurements was accomplished by linearly interpolating the data from the closest two real hours onto the composite hour. For each MCC category, the three individual composite fits were then arithmetically averaged hour-by-hour to give average areas $(\bar{A})$ and volumes $(\bar{V})$ for the core, peripheral and total rainfall. Average hourly rainfall intensities were finally computed as $\bar{R} = \bar{V} / \bar{A}$. The identical averaging methodology was used to derive quantitative composite histories of the -53 and $-32^{o}C$ IR areas.

To provide more insight into the average hourly precipitation rates ($\overline{R}$), a similar composite approach was followed in deriving frequency distributions of measurable rainfall reports over various intensity categories. This analysis was carried out separately for the 2.5-mm and 0.25-mm gages, thus providing two independent analyses for each composite. The procedure consisted of tabulating hour-by-hour the number of MCC-related measurable precipitation reports exceeding each intensity threshold in each MCC, smoothing these frequencies in time with a 1-2-1 running average, fitting the smoothed frequencies onto the composite MCC time scale, and summing the three individual-MCC frequencies in each composite. The total sample size for a given hour is thus the summed number of measurable reports (roughly proportional to rainfall area), with each MCC being weighted by its number of reports (as opposed to the equal MCC weighting used to derive $\overline{A}$, $\overline{V}$ and $\overline{R}$ by arithmetic averaging). Relative frequency distributions were then calculated by dividing the number of reports exceeding each intensity threshold by the total sample size.

For further comparison, a similar analysis was performed utilizing hourly mappings of Manually Digitized Radar (MDR) data, derived from the National Weather Service WSR-57 radar network (Moore et al., 1974). These data consisted of a grid of boxes, each being aproximately 84-km square at 40°N and assigned an MDR code value according to the criteria in Table 2. The frequencies of non-zero MDR values associated with each MCC were tabulated, smoothed and composited in a manner analogous to the rainfall intensities.

d. Other data and analysis

In the case studies of MCC evolution in Section 4, the roles of significant surface features such as fronts, troughs and mesoscale outflows from convective activity are qualitatively described. The identification of their existence, movements and roles has required the detailed analysis of extended sequences of hourly surface maps, augmented by IR and visible satellite imagery. The surface analyses are based on all available (first and lesser-order) hourly surface observations (cloud reports and comments included) on file with the Bureau of Reclamation. For the sake of brevity, we present only one surface analysis near the beginning of each case.

Because of our meso-β-scale emphasis, upper-air analyses are also presented rather sparingly to simply describe the large-scale environment in which the MCCs formed. These analyses are based on soundings from the conventional synoptic rawinsonde network.

4. THE MESO-β-SCALE SUBSTRUCTURE AND EVOLUTION OF THE MCCs

Several meso-β-scale characteristics of MCC evolution are described qualitatively in this section. In order to emphasize those characteristics that are somewhat consistent from case to case, several MCCs from the episode are presented, concentrating on the large systems in Table 1. We first describe each of the western large systems, and then for comparison, discuss one of the eastern large systems.

a. MCC #1 - Western system of 3-4 August

The first MCC of the episode (MCC #1 from Fig. 1) developed from afternoon convection on the High Plains of western Nebraska and northeast Colorado, propagated eastward through the night of 3-4 August as an intense MCC, and weakened in the early daylight hours over the Mississippi Valley. Fig. 3 provides an IR satellite overview of this evolution.

An upper-air analysis for 0000 GMT 4 August (Fig. 5a) depicts various large-scale low to mid-tropospheric features accompanying the formative stages of MCC development in western Nebraska (see Fig. 3a). The observed winds at 850, 700 and 500 mb are plotted at the rawinsonde sites, and the fields of 700-mb height, 850 to 700-mb thickness, and surface to 500-mb precipitable water vapor are analyzed. Notable features which are consistent with previous MCC studies (Maddox, 1983; Bosart and Sanders, 1981; Maddox and Doswell, 1982; Cotton et al., 1983; Wetzel et al., 1983) include: a pronounced southerly low-level jet from the Texas panhandle into western Kansas and Nebraska; pronounced lower-tropospheric thermal advection (from the elevated heat source over the southern Rocky Mountain plateau) by the veering 850 to 700-mb winds in the same region; and abundant moisture (exceeding 30 mm of precipitable water) to the south and east of the developing system. The shaded region of pronounced convective instability, considering both the Lifted Index and the Total-Totals Index (Miller, 1972), over Nebraska and Kansas corresponds closely to the center of subsequent MCC development seen in Fig. 3.

At 700 mb, a weak short wave extended across the development region from South Dakota to eastern New Mexico, with a downstream ridge from northeastern Texas into Missouri and Iowa. The 500-mb height field (not shown) indicates no short-wave feature in the area. However, objective kinematic analysis (not shown) of the depicted 500-mb winds indicates a region of cyclonic vorticity advection (CVA) centered over northeastern Colorado, upstream of the obvious anticyclonic vorticity axis running roughly along the eastern border of Colorado into northeastern New Mexico. Thus, the developing meso-α-scale cloud system in Fig. 3, occurring at the leading edge of this CVA field, was apparently supported dynamically at mid levels in a manner consistent with the development of the composite MCC as described by Maddox (1983).

A surface analysis of sea-level pressure, temperature and dewpoint at the same time (Fig. 5b) depicts the major surface features at the genesis stage of MCC #1. The analysis is based on hourly surface observations whose locations are shown by the plotted winds. The larger-scale features included a cold front in southeast Montana (just entering Fig. 5b), a north/south lee-side trough that had existed all afternoon along the High Plains from Montana to New Mexico, and a weak stationary front extending southeastward from southeast Montana to southeast Nebraska and turning northeastward towards Wisconsin. The latter feature had little thermal contrast, but separated relatively weak, dry northerly winds to its north from stronger, moist southerly flow to the south. The southeasterly wind in the moist tongue (dewpoint temperatures > 16°C) extending from Kansas across western Nebraska provided low-level moisture to the developing convective clusters in western Nebraska (Fig. 3a).

Significant smaller-scale surface features at 0000 GMT (Fig. 5b) included an expanding complex of merging mesohighs produced from the developing convection in western Nebraska, and an older mesohigh in eastern Kansas produced by an area of light rainshowers and thundershowers that had travelled southeastward from the south-central Nebraska region throughout the day. A coherent IR cloud shield from this convective activity can be seen in eastern Kansas in Fig. 3a, with an axis of residual cloudiness extending northwestward back into Nebraska. Note also the very thin band of unenhanced cloudiness oriented northwest-southeast (NW/SE) across Kansas about 150 km to the west of this cloud shield. This cloud band, producing no radar echoes at this time, was apparently aligned closely along the western border of the mesohigh, where the surface data indicate converging cool, moist easterly flow from eastern Kansas with warm, drier southerly flow from southern Kansas.

The composite IR satellite and meso-β radar analysis in Fig. 6 illustrates several important evolutionary features of MCC #1. Included in the analysis are IR contours of -32 and -53°C at the indicated hours, and the positions and 2 h displacements of meso-β echo features at about 25 min after the respective hour.

The IR/radar depiction for 01 GMT (Fig. 6a) shows three meso-β convective clusters (labelled A, B and C) in a N/S line in western Nebraska and eastern Colorado. These had all originated along the Wyoming and Colorado foothills and are typical of the eastward-propagating orogenic convection induced by the differential diurnal heating over the mountains and plains (Wallace, 1975; Paegle, 1978). In this case, the climatological afternoon upslope wind produced by this diurnal forcing over the High Plains (Johnson and Toth, 1982) were synoptically enhanced by the N/S surface trough and focused in western Nebraska and northeastern Colorado to the north of the low pressure center in eastern Colorado (Fig. 5b). Cluster A formed earliest and was most intense, producing severe winds and large hail in western Nebraska[4]. Propagating into the moist tongue seen in Fig. 5b (dewpoint

---

[4] These and subsequent severe weather events are extracted from Storm Data", published monthly by the National Climatic Center, NOAA/EDIS, Asheville, NC 28801.

temperatures > 16°C), cluster A intensified most rapidly and produced the bulk of the cold cloud shield which met MCC criteria by 0200 GMT.

In eastern Kansas, cluster D (Fig. 6a) was a residual area of weak convection that had produced the surface mesohigh in that region (Fig. 5b), and a new line of convective echoes (E) was apparently triggered on the western boundary of the mesohigh. A final meso-β feature (F) in South Dakota was to the north of the stationary front (Fig. 5b) and persisted as a detached and minor peripheral component of the subsequent MCC.

Over the next 4 h (Fig. 6b,c), these clusters continued their general eastward propagation, with the line of orogenic clusters (particularly A and B) propagating much faster than the convective bands to the east. By 05 GMT (Fig. 6c), clusters A and B had become well-organized into meso-β-scale squall lines. This was likely due to their propagation into the low-level jet region, thereby increasing the low to mid-tropospheric shear (see Fig. 5a). The 0500 GMT IR image (Fig. 3c) identifies these clusters as distinct bands of intense overshooting cumulonimbi.

A new meso-β echo feature (G) formed along the stationary front in central Nebraska by 03 GMT (Fig. 6b), and together with the similarly oriented clusters E and D, loosely defined a NW/SE meso-α-scale axis of convective clusters. By 05 GMT (Figs. 6c, 3c), this axis was being approached by the A-B orogenic line. The western portion of G was overtaken as it merged into the northeast end of A, while its eastern portion rapidly intensified as a right-moving severe storm that produced a 50-km hail swath (and its own overshooting top signature in the 0500 GMT IR image) and merged with the meso-β band E.

The motion of clusters A and B over the previous 6 h (Fig. 6a-c) was confluent, perhaps due in part to steering by the confluent 700-mb winds in this region (Fig. 5a). Their rapid propagation and confluence continued over the next 2 h, so that by 07 GMT (Fig. 6d), clusters A and B had merged and overtaken clusters G and E, creating a large meso-β (or small meso-α) band of intense convection. Cluster D lost much of its discrete identity and expanded as an echo of more uniform intensity that merged into the A-B-G band. The combined overshooting convective cloud top from this complex attained its coldest temperature and largest areal extent at about this time (Fig. 3d). A tornado and a 200-km track of severe surface winds were produced by cluster A during the merging of these lines, making the case appear similar in many respects to the "derecho" as described by Johns and Hirt (1983).

We note qualitatively that the most intense phase of MCC development, between about 03 and 07 GMT (Figs. 6, 3), was focused near the intersection of two meso-α-scale linear features: the rapidly propagating N/S string of orogenic convection A-B, and the slower, NW/SE convective axis G-E. Analogous intersecting meso-α-scale linear features are seen to play key roles in all of the MCCs subsequently described. In the most general terms, meso-β convective features originate along (and subsequently help define) the meso-α axes, and those meso-β features nearest the point of intersection of the meso-α axes (in this case clusters A and G) intensify most rapidly, merge and become the apparent core of the MCC.

After the merging of the several discrete meso-β features into a larger meso-β cluster of widespread intense reflectivity (Fig. 6d), a larger area of more uniform and weaker echo developed (Fig. 6e). The

AD-A161 136 EFFECTS OF MOUNTAIN RANGES ON MESOSCALE SYSTEMS DEVELOPMENT(U) COLORADO STATE UNIV FORT COLLINS DEPT OF ATMOSPHERIC SCIENCE E R REITER ET AL SEP 85 2/2

UNCLASSIFIED AFOSR-TR-85-0924 AFOSR-82-0162 F/G 4/2 NL

END

FILMED

DTIC

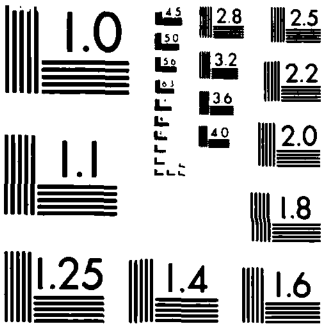

MICROCOPY RESOLUTION TEST CHART
NATIONAL BUREAU OF STANDARDS-1963-A

meso-β convective band A continued its southeastward propagation near the leading edge of this larger precipitation field, so that the echo structure of the MCC resembled that of tropical cloud clusters (Zipser, 1977; Houze, 1977). The other meso-β convective features became weaker and/or ill-defined within the larger precipitation field, and new meso-β features (H,I) developed on the southwestern flank of the precipitation complex.

Whereas up until the time of maximum MCC convective intensity (Fig. 3d) the meso-β convective features displayed a confluent tendecy (Fig. 6a-d), in the weakening stages they became difluent, with the northern bands (F,D) propagating eastward and the southern ones (A,I,H) more southeastward (Fig. 6e,f). This difluent propagation may be due to further convective growth being forced at the boundary of the expanding surface mesohigh. Accompanying this difluent motion of the weakening MCC's meso-β convective components was a loss of circularity of its cloud shield, which lengthened in a NE/SW orientation and assumed more of a meso-α comma cloud configuration (Fig. 3f,g) that is more typical of a short-wave disturbance.

b. MCC #2 - Western system of 4-5 August

The next evening's MCC (#2 from Fig. 1) displayed similarities to, but also some significant differences from, MCC #1. The synoptic conditions accompanying the developing stages of this system at 0000 GMT 5 August, discussed in more detail in Cotton et al. (1983), are summarized in Fig. 7. The 700-mb height field (Fig. 7a) displays two short-wave troughs extending southwestward from Minnesota and southward from Montana, both towards Colorado. Weak troughing extends further southeastward from Colorado into Oklahoma, just upstream of a subtropical ridge axis extending westward from the southeastern United States into Kansas. As on the previous day, confluence in the 700-mb winds from Nebraska to the Texas panhandle provided a focusing steering flow over the MCC genesis region. Other low to mid-tropospheric features similar to the previous evening's case include: a southerly low-level jet evident in the Texas panhandle and Oklahoma; lower-tropospheric thermal advection, most evident in the same region; 500-mb CVA upstream of a N/S anticylonic vorticity axis in eastern Colorado and New Mexico; and increasing moisture into which the system developed. A cool surge of northerly flow over the northern plains (see 850-mb winds) resulted in the most unstable region (shaded area) to be further south than on the previous evening, along with a similar southward displacement of the low-level jet (compare with Fig. 5a). The southward displacement of those features likely contributed to the more southern track of MCC #2 (Fig. 1).

Large-scale surface features at 0000 GMT (Fig. 7b) which also apparently helped control the MCC's evolution included a weakly defined front, associated with the cool surge mentioned above and extending east-northeastward from its stalled position in eastern Colorado, and an E/W discontinuity across southern Kansas, separating relatively cool, moist easterly flow over much of Kansas from the southerly flow to its south. This latter feature was the remnant of the outflow boundary produced by the previous evening's MCC as it tracked eastward, and it also closely marked the southern extent of that system's precipitation. A N/S string of developing mesohigh complexes produced by the orogenic convection on the eastern slopes of Colorado and New Mexico was propagating eastward towards these E/W discontinuities.

The evolution of MCC #2 is illustrated by the IR/radar analysis in Fig. 8. The mountain origins of meso-β cluster B in this figure, and the evolution of clusters A and B in eastern Colorado, are detailed in Cotton et al. (1983), and the low-level forcing associated with this MCC's genesis and continued evolution is followed in Wetzel et al. (1983). At 01 GMT 5 August (Fig. 8a), the N/S line of orogenic convection was organized into three meso-β clusters (A, B and C), all within a contiguous IR cloud shield. Newer convection (D) was developing further east in southern Kansas. Two hours later (Fig. 8b), cluster D had grown in a general E/W orientation, and along with a new cluster (E), defined an E/W axis of meso-β convection that was aligned along and probably triggered by the southern Kansas surface discontinuity (Fig. 7b). The motion of clusters A and B was confluent from 01 to 03 GMT, during which B produced severe winds and hail in southeast Colorado. With stronger easterly moisture advection feeding these eastward propagating clusters than cluster C (see Fig. 7b), they became the core of the mature MCC while C persisted as a relatively weak peripheral cluster on the southwest flank of the meso-α system.

For the period 03-05 GMT, IR imagery indicates two distinct centers of very intense convection, qualitatively associated with the intersections of the N/S orogenic line A-B with the E/W-oriented surface front in northwest Kansas (cluster A) and with the old outflow boundary in southwestern Kansas (cluster B). After 05 GMT, the coldest region of overshooting tops consolidated between these two centers of activity (A and B) into a larger region of overshooting convection, becoming the apparent core of the intense MCC and persisting through 07 GMT (Fig. 8c,d). Accompanying this consolidation of clusters A and B was the development of a larger area of lighter and more uniform radar echo between them.

Ahead of this primary MCC development, cluster F developed in northeast Kansas as a relatively independent and stationary mesoscale convective system of sub-MCC dimensions, producing its own intense IR anvil cloud shield that persisted through 10 GMT as a somewhat detached lobe of the main MCC (Fig. 8b-e). More chaotic and/or displaying less coherent meso-β continuity were the evolution patterns of the other meso-β convective features. Cluster D, for instance, displayed a general northward movement (Fig. 8c,d) due to widespread cell growth (dissipation) on its north (south) side. The cloud shield evolution associated with cluster D's "anomalous" propagation included the dissipation of its initial E/W cloud band in southern Kansas (Fig. 8c) and the filling in of the meso-α cloud shield between the clusters A-B and F (Fig. 8d). After the most intense "overshooting" phase of the MCC at about 07 GMT, clusters A and B weakened considerably. Cluster D continued its northward propagation and became the apparent core of the main MCC, which maintained a highly organized meso-α appearance through 09 GMT (Fig. 8d,e). By this time, however, two distinct centers of intense overshooting activity became apparent again, associated with the now difluent clusters D and B (Fig. 8e).

During the decaying stages of the MCC (after the time of maximum -53°C IR area), cluster D weakened and merged into the southern end of G, which previously had been a minor peripheral component on the northern edge of the MCC in Nebraska. Relatively stationary prior to the MCC's decay phase, cluster G now assumed a NE/SW orientation and began to propagate eastward (Fig. 8e,f), where it intensified and produced much precipitation for several more hours over Iowa. The development and maintenance of this NE/SW band was apparently linked to the approach from the northwest of a surface cold front, seen in South Dakota at 00 GMT (Fig. 7b). The other meso-β convective components weakened during the MCC's decay and became organized in a similarly oriented NE/SW line across eastern Kansas and northern Missouri, loosely joined by a decaying shield of "anvil" precipitation. Difluent motion between the meso-β components was evident in the decaying stage, though not as pronounced as in the previous evening's MCC.

A distinct difference between the meso-β sub-structures of the first two MCCs of the episode is that the major meso-β components of MCC #2 did not become as cohesively unified towards a meso-α organization as in MCC #1 (compare Figs. 8d,e and 6d,e). The meso-β squall-line type organization in MCC #1 may have been due to the stronger low to mid-tropospheric shear (compare Figs. 5a and 7a), making the case more akin to the classic mid-latitude squall line (Palmen and Newton, 1969). Also related to this stronger baroclinicity for the first MCC was a faster and more consistent propagation of its meso-β components. In MCC #2, cluster F remained nearly stationary through much of the life cycle, producing large precipitation accumulations over northeast Kansas, while other clusters (particularly D) propagated more "anomalously" and less consistently.

c. MCC #3 - Western system of 5-6 August

The next evening's system (#3 from Fig. 1) became the final large, well-organized High Plains MCC of the episode, with the subsequent western systems over the next five days being smaller and/or less organized. Low to mid-tropospheric features at 0000 GMT 6 August, at the early stage of its development (Fig. 9a), were similar to the previous two evenings. The features essential for MCC development included a low-level jet over the Texas panhandle, warm advection over the southwest plains, and increasing moisture towards the east over Kansas. A weak 700-mb trough over southeast Colorado and a ridge extending from the southeastern U.S. into eastern Kansas resulted in a short-wave trough/ridge configuration and a confluent 700-mb flow pattern over western Kansas similar to the previous two cases. A stronger short-wave over Wyoming at 700-mb (and 500-mb) was associated with a stronger cool surge over the northern plains than on the previous day.

The surface cold front associated with this strong cold surge had moved southward over the previous 24 h (see Fig. 7b) and by 0000 GMT 6 August (Fig. 9b) had moved well into Kansas. A weaker discontinuity across southern Kansas and northern Missouri was due to the outflow boundary produced by MCC #2 the previous evening, and separated strong southerly flow over the southern plains from moist, weaker easterly flow over Kansas. The pre-MCC precipitation activity was much more widespread than on the previous cases. Post-frontal rain and rainshowers were scattered across Nebraska, and eastward-propagating convection had developed early in the day over the eastern slopes of Colorado. By 0000 GMT this orogenic convection had become widespread over the Colorado and New Mexico High Plains, producing a growing complex of mesohigh outflows.

The IR/radar analysis in Fig. 10a illustrates the meso-β organization of this High Plains convection at around 22 GMT. Clusters A, B and C (and a recently dissipated cluster ahead of A) formed over the foothills early in the day, propagated onto the plains around midday, and by this time were nearing the Kansas border. Another "wave" of orogenic convective clusters (G, H and I) formed a second distinct N/S line about 3 h behind the first. Ahead of these N/S axes of convection, clusters D, E and F originated after 20 GMT as relatively weak convection (no cold IR cloud shield) and were arranged in a SW/NE orientation that was parallel to and on the north side of the cold front.

As on the previous evenings, the intersection of the propagating meso-α axis of orogenic convection (A-B-C) with the more E/W-oriented axis (D-E-F) marked the location of intense MCC development. In this case, cluster B weakened and dissipated as it approached clusters F and E, which simultaneously intensified (Fig. 10a,b). Cluster F produced large hail in western Kansas for over 2 h along with some tornadic activity, and cluster E merged into the intensifying southwest end of the more stationary convective band D (Fig. 10b,c).

Even though the MCC reached mature IR dimensions by about 01 GMT, satellite data at 02 GMT (Fig. 10c) indicate that the "meso-α" complex was actually composed of three distinct regions of mesoscale convective organization: clusters F and D, which produced the primary intensifying anvil in Kansas; the anvil lobe to the southwest that was produced by the meso-β features C, I and J; and an intense anvil lobe in eastern Colorado produced by the second wave of orogenic convection, particularly cluster H. The latter two anvil lobes subsequently weakened in convective intensity, while clusters F and D grew and merged to form a large band of intense convection across central Kansas (Fig. 10d). This merger produced a "bow-echo" radar pattern (Fujita, 1978) and severe weather over central Kansas at the center of the consolidated convective band. The persistence of this NE/SW band was appartently due in part to the active cold front across Kansas (Fig. 9b). Such control by a cold front on the meso-β-scale organization of convection is similar to what was seen in the decaying stage of MCC #2 the previous night (meso-β band G in Fig. 8f).

By 06 GMT (Fig. 10e), the MCC's anvil reached its most intense stage of widespread overshooting convective activity, centered on the F-D band. The convective organization of F had already weakened, however, with a larger, more stratiform precipitation area developing over central Kansas. Cluster H persisted as a relatively weak but large feature on the western end of the MCC through this period, and a small convective cluster (K) that developed to the rear of the F-D band propagated into and helped expand the large anvil precipitation region.

After the MCC reached its maximum -53°C IR areal extent at 07 GMT, the convective activity of the system was dominated by cluster L in northern Missouri (Fig. 10f). This feature originated ahead of the MCC hours earlier, and was one of several meso-β convective features strung from Missouri to New York along the E/W outflow boundary of the weakened system #2 (Fig. 9b). As the MCC (and the cold front) approached Missouri, cluster L rapidly intensified, first becoming an intense anvil lobe on the MCC's eastern flank, and then becoming the core of the system (Fig. 10d-f). This gave the appearance of discrete propagation of the MCC on the meso-β scale, resulting from the weakening of the older meso-β convective features in Kansas and the simultaneous development of newer convection (L) at the intersection of the system with the E/W discontinuity. Following 08 GMT, cluster L evolved into a larger, more stratiform precipitation feature that dominated the MCC through its decay to sub-MCC dimensions at 14 GMT over northern Illinois. A secondary, peripheral convective band (M) developed from previously unorganized shower activity over Nebraska during this decay period.

d. MCC #6 - Eastern system of 6-7 August

The next three evenings produced large MCCs which formed over the lower, more level eastern genesis region of Iowa and Missouri (see Fig. 1). The first of these, MCC #6, is described in this section in order to compare it with the western systems.

The low to mid-tropospheric features at 0000 GMT 7 August, several hours before the system's development, are shown in Fig. 11a. Whereas the southerly low-level jet in the three previously described cases decelerated in the High Plains genesis regions, in this case it curved anticyclonically over Kansas and continued as a southwesterly jet through Illinois. Strong warm advection by the veering 850 to 700-mb winds was similarly extended further east than in the previous cases. Abundant moisture extended from southern Illinois into southeast Nebraska, coincident with a pronounced band of convective instability that extended further west into Colorado. A well-defined shortwave trough at 700 mb over the eastern Dakotas was just to the north of the genesis region of southern Iowa.

The first thunderstorms associated with MCC #6 developed at about 0300 GMT in northwest Missouri, indicated on the surface analysis for that time in Fig. 11b. This development was near the intersection of two meso-α discontinuities. The first of these was the large-scale front which strongly influenced MCC #3 the evening before (see Fig.

9b), and which by this time had become relatively stationary in a ENE/WSW orientation from western Kansas, across southern Iowa and northern Illinois. The second boundary, extending southeastward across Missouri into southern Illinois and Indiana, was produced and maintained by the small but intense eastern MCC #4, which developed in northern Missouri several hours earlier and by this time was weakening over Indiana. As that system developed into a mature MCC near 2200 GMT, it produced a concentrated outbreak of severe weather, including numerous tornadoes, along a 100-km track in central Illinois. This outbreak is described in detail by Forbes and Wakimoto (1983). It is interesting to note that MCC #4 developed near the intersection of an E/W discontinuity that formed along the southern extent of the precipitation produced by MCC #3, with a N/S axis of residual cloudiness trailing from that same system. Thus, the meso-α boundary in Fig. 11b was actually a pre-existing feature that was reinforced, maintained, and in some locations re-formed by MCC #4. The warm sector to the south of the intersecting meso-α boundaries was characterized by strong southerly flow feeding warm, moist air towards the intersection. This configuration of surface discontinuities in the MCC's genesis region was closely repeated for the second and third large eastern MCCs during the next two evenings.

The IR/radar analysis of the MCC's evolution is shown in Fig. 12. Since the eastern portion of the analysis area is beyond the available radar PPI coverage, the analysis is extended by indicating areas of measurable hourly rainfall. As noted in Section 3b, we generally found such hourly precipitation envelopes to be consistent in terms of size and continuity with the MCC's radar-derived meso-β convective features. For further interpretation of the organization and intensity of the convection within these rainfall areas, the NWS radar depiction charts, the MDR maps and satellite imagery were utilized.

Several discrete thunderstorms formed near 0300 GMT in extreme northwest Missouri. By 0430 GMT (Fig. 12a), this convective activity had consolidated into three small meso-β clusters (A, B and C) and had produced a small, convectively intense anvil cloud. Meso-β feature D in northern Iowa was a less intense band of thunderstorms on the north side of the stationary front and remained a minor component of the MCC. In the wake of MCC #4, now weakening over Indiana and Ohio, meso-β cluster E in central Illinois was also a relatively weak, recently formed feature.

Over the next two hours (Fig. 12b), clusters A, B and C consolidated into a single intense meso-β cluster (A) on the western flank of the rapidly expanding anvil cloud. A new meso-β band, F, formed to the northeast of cluster A and began developing southeastward into the northwestward expanding band E. Satellite images show that this NW/SE oriented band E-F developed within a thickening band of cloudiness that was advecting northeastward from its origins several hours earlier along the weak outflow boundary in Missouri. This convection produced an anvil lobe protruding southeastward from the initial anvil.

The MCC's anvil had a cold, intense cellular appearance from about 08 to 11 GMT (Fig. 12c,d). Though cluster A and the E-F band became aligned into a common, more extensive E/W band, the radar and rainfall data show that the most intense convection persisted as two discrete meso-β regions, in southeast Iowa and in central Illinois. Towards the end of this intense MCC phase, a new meso-β cluster, G, formed just to the southeast of cluster A.

As the MCC weakened after 11 GMT (Fig. 12e,f), as indicated by the interior anvil top warming, cluster G propagated southeastward away from the weakening cluster A, similar to the difluent propagation seen in the western cases. The more interior precipitation feature E expanded into a larger region of relatively light, stratiform rain, with its convective elements concentrated along its southern edge. Cluster E persisted as a large, coherent feature with a southeastward drift through 15 GMT, when it began to break up into weak, difluently propagating elements.

Several differences are apparent between the large eastern MCCs (as typified by #6) and the large western MCCs (#1, 2 and 3). In all the western systems, a N/S string of discrete meso-β convective clusters developed on the High Plains just to the east of the Rockies, in diurnally forced (or enhanced) upslope flow, and played a major role in MCC development. This upscale development centered on the intersection of the N/S meso-α string of convective clusters with another, more E/W-oriented meso-α boundary, along which other meso-β convective features were aligned. The eastern MCCs, without this orographic forcing, developed instead near the intersection of a large-scale front and an old, meso-α outflow boundary to its south. Fewer meso-β convective components were involved in the formative stages of the eastern MCCs, which instead tended to grow upscale more rapidly from one or two vigorous meso-β clusters.

Another major difference between the western and eastern MCCs was that the latter tended to continuously regenerate convective elements on the southwestern flank (as with cluster A in Fig. 12), remaining more stationary than the eastward propagating western MCCs. There are several factors that likely contributed to this difference. The low-level jet that supplies much of the moist, unstable air to the systems was more rear-feeding (southwesterly) for the eastern systems, while topography constrains it to be more southerly over the sloping plains in the western cases. Secondly, more widespread low-level moisture was available for the eastern systems, versus the consistent west-to-east (high-to-low elevation) moisture gradient for the western systems. Finally, more pronounced forcing on the eastern flank of the western systems, due to a downsloping density current, may have contributed to their more pronounced eastward propagation. At any rate, the western MCCs, with their more numerous and faster propagating meso-β convective components, displayed seemingly more chaotic and random patterns of development in their internal sub-structures, than the eastern systems.

5. MESO-β-SCALE PRECIPITATION CHARACTERISTICS OF THE MCCs

The previous section demonstrates that despite the characteristic meso-α-scale evolution of the MCC's cloud shield (as typified by the satellite sequence in Fig. 3), there is a complex variability in its radar sub-structure from system to system. The hourly precipitation patterns and amounts likewise display a corresponding variability. Rockwood et al. (1984) present these characteristics for a particular dual MCC case. To avoid becoming mired in the complex details of the individual MCCs in this episode, we have adopted a composite analysis approach that reduces the information content of the twelve MCCs listed in Table 1 into four composite categories: western-large, western-small, eastern-large and eastern-small MCCs (W-L, W-S, E-L and E-S, respectively). As discussed in Section 3c and illustrated in Fig. 4, each composite MCC is based on three individual systems that had similar IR-defined life-cycle characteristics. The resultant composite categories, while losing the spatial complexity inherent in the individual systems, retain important temporal variations that allow generalizations to be made concerning the western/eastern and large/small MCCs. Because our sample size is too limited to permit meaningful calculations of statistical significance, our interpretation of these variations are qualitative.

The growth/decay cycle of the IR cloud shield associated with each composite MCC is displayed in Fig. 13. For all composites, both -53 and -32°C areas expand monotonically to their maximum sizes, followed by monotonic decreases. The major difference between the two large composites is that the E-L system has a much larger expansion rate in its first several hours, and attains a meso-α "cellular" organization much sooner, than the slower developing W-L MCC. Comparing the large and small systems, both large composites have early growth rates exceeding those of their smaller counterparts. For example, over the organizational period from MCC hours -2 to 2, the growth rates of the -53°C area in the W-L and E-L systems are 159% and 195% of the W-S and E-S rates, respectively. This suggests a potential short-range forecasting technique whereby the maximim size and duration of an MCC might be projected from its early growth trend. For each composite, the expansion rates of the -32 and -53°C areas are fairly constant from "start-to-maximum", with the ratio of -53 to -32°C areas remaining relatively steady at about 0.6 to 0.8. After the "maximum", the -32°C area continues to expand for another hour, and the ratio decreases steadily to the "end". This single growth/decay cycle was characteristic of the individual MCCs, and supports the view that the mature MCC develops an organized meso-α-scale vertical circulation (Maddox, 1980); a system less organized on the meso-α-scale and more dominated by convective-scale circulations might be expected (if it could produce a large contiguous anvil at all) to produce a more pulsating anvil with multiple maxima of cold IR areas during its extended duration.

Just as the -53°C area attains a maximum 1 h prior to the maximum -32°C area in all composites, the "overshooting-top-maximum", with an extensive interior region of cloud-top temperatures considerably colder than -53°C, occurs about 2 h prior to the maximum -53°C area. Thus, to the extent that cloud-top temperatures represent the intensity of vertical motions, there is evidence that the MCC transforms steadily from a relatively small system dominated by intense convective circulations into a larger system of diminishing vertical motions.

Recall from Section 3c that hourly values of measurable rainfall area and volume (A and V) were derived for each individual MCC, and these were filtered with a 1-2-1 running average to yield smooth values of A and V. The total time-integrated rainfall volume for each MCC, derived by summing the unsmoothed values of V from MCC hour -2 to "end"+1, is listed in Table 1 as a measure of total storm rainfall production. While the W-L and E-L MCCs produced anvils about 2.5 times larger than their smaller counterparts, their average rainfall volumes were 13.6 and 4.6 times greater, respectively, than that of the smaller systems' averages. Since this can only be partly accounted for by the larger systems' longer durations (less than a factor of 2), there is evidence that large MCCs are more efficient precipitators than smaller systems. This is particularly evident for the western cases, where one would expect significant sub-cloud evaporation of precipitation in this semi-arid region. Indeed, the W-S MCC #5a produced no recorded rainfall for 2 h of its "cellular" period. A probable contributor to the larger systems' greater efficiency is that the area-to-perimeter ratio of their precipitation-producing cloud area is larger, which implies a correspondingly large ratio of protected "core" precipitation to "peripheral" precipitation, the latter being more susceptible to evaporation in the subsaturated environmental air.

Using the 1-2-1 smoothed precipitation volumes and based on a total accumulated volume from MCC hour -1 to "end", the timing of quartiles of accumulated volume for each individual MCC is shown in Fig. 4. Within the W-L and E-L categories, note that the quartiles of accumulated volume are timed fairly consistently with respect to the IR features. Thus the composite precipitation analyses presented below accurately reflect the nature of the individual large systems. In contrast, there is much less consistency in the timing of the accumulated volume quartiles in both small MCC categories. While this is likely due in part to more serious sampling problems by the hourly rainfall network (i.e., fewer affected stations), it also likely reflects an inherent greater variability of these "smaller-scale" and less precipitation-efficient MCCs. Thus, the small MCC composite analyses presented below reflect less accurately the individual systems.

Fig. 14 depicts the precipitation trend for each composite MCC in terms of average hourly rain rate, area and volume ($\overline{R}$, $\overline{A}$ and $\overline{V}$). For the W-L and E-L MCCs, the graphs indicate that maximum $\overline{R}$ occurs early in the intense growth phase of the MCC, followed by a steady decrease that tends to level off in the latter decaying stage. $\bar{A}$ increases steadily until 1-2 h after the MCC "maximum" and near the $-32^{\circ}C$ maximum, followed by a steady decrease. The resultant $\bar{V}$ maximizes 1-2 h prior to the "maximum", towards the end of the "cellular" stage and near or shortly after the "overshooting-top maximum". From the quartiles of total accumulated precipitation volume shown in Fig. 4, it can be seen that the peak in $\bar{V}$ occurs about 1 h prior to the 50% quartile. The volumes, partitioned between "core" and "peripheral" precipitation, indicate that the great majority of the MCC's rainfall occurs within its "core" ($-53^{\circ}C$) region. Note that the maximum rain area, about 12×10^4 km^2 for both large composites, is less than half the maximum $-53^{\circ}C$ area seen in Fig. 13, indicating that most of the MCC anvil is non-precipitating. It is only during the last few hours, as the $-53^{\circ}C$ area shrinks to sub-MCC dimensions, that the diminishing rainfall becomes appreciably "peripheral".

The small composite MCCs in Fig. 14 show comparable trends in $\bar{R}$ and $\bar{A}$, which maximize early and relatively late, respectively, in the life cycles. The magnitudes of $\bar{R}$ are also comparable to those of the large systems. The smaller areas affected, however, result in much smaller volumes, which exhibit a much less pronounced growth/decay trend than seen in the large MCCs. The disproportionally low rainfall areas and volumes, relative to the IR anvil areas, of the small MCCs compared to the large systems (especially for the western composites) again suggest that the larger MCCs are more precipitation-efficient.

A more detailed examination of the average hourly rainfall rates depicted in Fig. 14 was made by deriving frequency distributions of reported rainfall intensities in the manner discussed in Section 3c.

The resulting distributions for the 2.5-mm and 0.25-mm gages are illustrated in Figs. 15 and 16, respectively, where the percentage of measurable reports contributed by each intensity category is represented by the height of the appropriately shaded bar. For the large MCCs, the maximum average rates in the early growth stage (Fig. 14) are shown in both gage-type analyses to be due to the relative maximum occurrence of the heavier hourly rates, including reports exceeding 51 mm. In Fig. 15, for example, the percentages of hourly reports $\geq$ 12.7 mm reach maxima of 25% at MCC hour 5 and 43% at hour 1 for the W-L and E-L composites, respectively. After these maxima, the decreasing fraction of intense rainfall represents the weakening of the meso-β clusters that built the meso-α complex. The meso-α system nevertheless continues to expand for several more hours, becoming increasingly dominated by the lighter rainfall intensities. While the W-S MCC shows a similar tendency in both Figs. 15 and 16, the E-S composite presents a less consistent trend, with intense rates persisting through most of its maturity in Fig. 15.

A similar frequency distribution analysis, utilizing the Manually Digitized Radar (MDR) data discussed in Section 3c, is shown in Fig. 17 and corroborates the findings of the rainfall distribution. For each composite (including the E-S MCC), the relative frequencies of intense "convective" MDR values (code thresholds 6 and 8 in Table 2) are high through the initial developing stage of MCC growth, remaining high until or maximizing in the early "cellular" stage. The relative occurrence of these high values decreases thereafter, with an increasing proportion of MDR values less than 6. Note that the areas of non-zero MDR coverage in Fig. 17, scaled to the number of non-zero blocks, are considerably larger than the hourly rainfall areas in Fig. 14, and are in fact much more comparable to the IR anvil areas in Fig. 13. The likely reason for this discrepancy is that the radars, which typically scan at 0.5 to 1.0^{o} in elevation out to ranges beyond 200 km, sample up to several kilometers in altitude and are detecting precipitation particles aloft in the anvil which never reach the surface.

From the analyses presented in Figs. 4 and 13-17, a fairly clear picture of MCC precipitation evolution emerges, particularly for the "better-behaved" large MCCs. The maximum relative occurrence of intense rainfall rates near the beginning of the organized "cellular" period and near the "overshooting-top maximum", and their subsequent decrease through the remainder of the "cellular" stage, imply that the intense early convection producing these intense rates is a necessary upscale forcing mechanism of the organized meso-α-scale circulation, which develops as a several-hour response to that forcing. During that response, the MCC is transformed into a larger precipitating system of increasingly lighter and more stratiform anvil rainfall, and then gradually decreases in size as it decays.

The relationship between the enhanced IR cloud-top features and the concurrent rainfall characteristics of these MCCs are qualitatively consistent with empirical convective rainfall nowcasting techniques that rely on anvil expansion rates, cloud-top temperatures and cloud histories (Scofield and Oliver, 1977; Griffith et al., 1978). Moreover, inasmuch as these composites represent typical MCC life cycles, the relation of the IR and precipitation trends in Figs. 13-17 provides a potential tool for forecasting certain aspects of the latter 2/3 of the MCC's life cycle, especially for the "better-behaved" large systems.

For example, the real-time observation via satellite and radar (or raingages) of the formation of a growing, incipient MCC (MCC hour 0) would portend the increase or continuation of intense convective rainfall over the next 2-4 h, and a longer steady increase in both precipitation area and volumetric rainfall rate. Continuing into the life cycle, the observation of a decrease in relative frequency of intense convection within an organized, "cellular" MCC would signal that the system will expand and the "cellular" stage will persist for 2-3 h longer, then will gradually decay. From the standpoint of average precipitation intensity in Fig. 14, such decreasing trends might be reliably established in real time over the period of MCC hours 3 to 5 for the W-L MCC, and hours 1 to 3 for the E-L system. As a hydrological forecasting tool, that determination would permit the projections of maximum volumetric rain rates of the system to occur over the next 3-5 h. A further precursory indicator of those projected maxima would be the first signs of the IR cloud shield showing weakening in its "overshooting top" intensity (evident by MCC hours 6 and 5, respectively, for the W-L and E-L composites). After a decreasing trend is observed over a 1-2 h period following the maxima in any of the volume, area or average intensity trends, the curves suggest that simple extrapolation techniques could project these trends for several hours through the MCC's dissipation.

6. SUMMARY AND DISCUSSION

Based on an investigation of a series of MCCs that occurred over eight successive evenings in the central U.S., a number of qualitative generalizations are inferred concerning their structural evolution. These include:

1) MCCs originating on the High Plains often develop from the growth, interaction and merger of multiple discrete meso-β convective clusters. These meso-β components tend to originate along larger, meso-α-scale features, such as the eastern slopes of the Rockies, surface troughs and fronts, extensive mesoscale outflow boundaries, and axes of residual convection and mid-level moisture. The orogenic line of meso-β clusters is the most important, probably participating in most western MCCs.

2) In all of the western cases, more than one meso-α feature as described above was important. The region of most intense meso-β convective development and rapid MCC growth occurs near the point where these meso-α features intersect. Purdom (1979) has inferred from satellite imagery that convective development is preferential along discontinuities, such as fronts, arc cloud mesohigh boundaries, and dry lines. He noted that new deveopment is especially favored at the intersection of one of these features with another boundary or with a cumulus cloud field, presumably due to focused vertical motion in such regions. While his work has concentrated on convective scale development on meso-β boundaries (e.g., arc clouds, as observed in high-resolution visible imagery), analogous focusing appears to be occurring on a larger scale with MCC development: meso-β convective clusters are spawned along meso-α-scale features, and the intersection of the meso-α features helps to reinforce the convection and to activate their upscale development into an MCC.

3) The eastern MCCs, generated in Iowa and Missouri, involved fewer discrete meso-β components in their formation, tending instead to grow upscale from one or two vigorous meso-β convective clusters. However, they did develop at the intersection of linear meso-α features, as did

the western systems.

4) In both eastern and western regions, meso-α features resulting from previous MCCs were important in affecting the evolution of new systems. Examples of such environmental modifications by an earlier MCC are the generation of a mesoscale outflow boundary, the reinforcement of a preexisting thermal discontinuity, and the development of a significant soil moisture discontinuity due to rainfall.

5) The configuration and development of meso-β clusters were more chaotic and random in the western MCCs, unless there were strong environmental controls, such as an active cold front or strong vertical wind shear. The latter tends to produce meso-β squall lines oriented perpendicular to the shear and also maintains the severe weather potential longer into the MCC lifecycle. The less chaotic nature of the eastern MCC's meso-β sub-structure may be related to the fewer intense meso-β clusters that were involved in their genesis and a more saturated subcloud environment, which together would produce fewer and less vigorous storm outflows that could interact in the manner described by Purdom (1979).

6) In the absence of strong controlling influences (such as fronts), the decay of the MCC is characterized by (or perhaps caused by) the difluent propagation of its meso-β elements.

7) The precipitation produced by an MCC is largely confined to the meso-β convective features, particularly for the western systems. Though the cold, uniform cloud shield may be indicative of mid to upper-tropospheric meso-α-scale ascent and precipitation generation, subcloud evaporation significantly reduces the area and amount of precipitation reaching the surface.

It must be recognized that these generalizations are drawn from an analysis of only a few MCCs occurring in a quasi-steady-state synoptic pattern, and thus may not be representative of MCCs that form under different synoptic conditions, in different geographical regions, or earlier or later in the convective season. For instance, Clark _et al_. (1980) and Merritt and Fritsch (1984) discussed several classes of organized mesoscale convection that can meet the satellite-defined MCC criteria, but each type was associated with a distinct synoptic pattern which exerted strong controls on the internal organization of the storm. Indeed, the cases discussed here and those recently described by others (Leary and Rappaport, 1983; Rockwood _et al_., 1984) indicate that there is extreme variability in the internal structure and evolution of MCCs.

Nevertheless, the net result in each case is a long-lived meso-α-scale system that develops from more localized, intense convective forcing. By averaging through the internal complexity of the MCCs, an analysis of hourly precipitation statistics has shown that this evolution is characterized by a well-defined precipitation life-cycle relative to the satellite appearance, especially for the larger MCCs. Average precipitation rates, and the fraction of precipitation due to intense rainfall rates, increase through the initial developmental stage and reach their peak near the time that the MCC attains an organized, meso-α-scale "cellular" appearance. The essential upscale transformation into an intense MCC has thus occurred by this time, which is still early in the life-cycle. During the several-hour intense "cellular" stage, the volumetric rain rate of the MCC reaches a well-defined maximum, which may reflect the maximum intensity of its meso-α-scale circulation. Shortly after this maximum, the MCC reaches its maximum size (-53°C IR area) and loses its organized meso-α-scale "cellular" appearance. Though the active rain area continues to expand a while longer, it is characterized by increasingly lighter rain and is apparently indicative of a prolonged, weakening mesoscale circulation.

This life-cycle resembles closely that discussed by Leary (1984) and generalized by Houze and Betts (1981) for mesoscale precipitation features in the tropical Atlantic. The latter study hypothesized that the strong convective forcing maximizes about a third of the way through the feature's typical 12-h life-cycle, the latter 2/3 being a prolonged mesoscale response. It seems likely that useful hydrological forecasting techniques could be developed on the basis of this extended response to real-time observable events. In those MCCs having multiple meso-β-scale convective features, it remains unclear to what extent each feature undergoes a similar life-cycle independently, or whether they interact dynamically in a way that appreciably affects the entire meso-α-scale system.

Acknowledgements

Dr. Peter J. Wetzel performed some of the preliminary analysis incorporated into this study. Careful reviews by John F. Weaver and Michael A. Fortune helped us to finalize the paper. The satellite data covering the MCC episode were provided by Dr. Aylmer H. Thompson. We thank Lucy McCall and Judy Sorbie for their drafting services and Brenda Thompson for processing the manuscript. This research was supported under National Science Foundation Grants #ATM-7908297 and #ATM-8312077, by the National Aeronautics and Space Administration under Contract #NSG-5341, and by the Office of Naval Research under Contract #N00014-

83-K-0321. It was also supported in part by the Air Force Office of Scientific Research under AFOSR Grant #82-0162 and by the National Oceanic and Atmospheric Administration under Grant #NA81RAH00001.

REFERENCES

Betts, A.K., R.W. Grover and M.W. Moncrieff, 1976: Structure and motion of tropical squall-lines over Venezuela. Quart. J. Roy. Meteor. Soc., 102, 395-404.

Bosart, L.F., and F. Sanders, 1981: The Johnstown Flood of July 1977: A long-lived convective system. J. Atmos. Sci., 38, 1616-1642.

Brown, J.M., 1979: Mesoscale unsaturated downdrafts driven by rainfall evaporation: A numerical study. J. Atmos. Sci., 36, 313-338.

Chang, C.B., D.J. Perkey and C.W. Kreitzberg, 1981: A numerical case study of the squall line of 6 May 1975. J. Atmos. Sci., 38, 1601-1615.

Clark, J.D., A.J. Lindner, R. Borneman and R.E. Bell, 1980: Satellite observed cloud patterns associated with excessive precipitation outbreaks. Preprints, Eighth Conf. on Weather Forecasting and Analysis, Amer. Meteor. Soc., 28 June - 1 July, Denver, Colorado, 463-473.

Clark, J.D., Ed., 1983: The GOES User's Guide. U.S. Dept. Commerce, National Oceanic and Atmospheric Administration, National Environmental Satellite, Data, and Information Service, Office of Satellite Data Processing and Distribution, 167 pp. [NTIS No. PB84-104413].

Cotton, W.R., R.L. George, P.J. Wetzel and R.L. McAnelly, 1983: A long-lived mesoscale convective complex. Part I: The mountain-generated component. Mon. Wea. Rev., 111, 1893-1918.

Forbes, G.S., and R.M. Wakimoto, 1983: A concentrated outbreak of tornadoes, downbursts and microbursts, and implications regarding vortex classification. Mon. Wea. Rev., 111, 220-235.

Fritsch, J.M., and C.F. Chappell, 1980: Numerical prediction of convectively driven mesoscale pressure systems. Part I: Convective parameterization. Part II: Mesoscale model. J. Atmos. Sci., 37, 1722-1762.

Fritsch, J.M., and R.A. Maddox, 1981: Convectively driven mesoscale weather systems aloft. Part I: Observations. Part II: Numerical simulations. J. Appl. Meteor., 20, 9-26.

Fujita, T.T., 1978: Manual of downburst identification for project NIMROD. Satellite and Mesometeorology Research Paper No. 156, Dept. of Geophysical Sciences, Univ. of Chicago, 104 pp. [NTIS No. N78-30771/7GI].

Gamache, J.F., and R.A. Houze, Jr., 1982: Mesoscale air motions associated with a tropical squall line. Mon. Wea. Rev., 110, 118-135.

Gray, W.M., and R.W. Jacobson, Jr., 1977: Diurnal variation of deep cumulus convection. Mon. Wea. Rev., 105, 1171-1188.

Griffith, C.G., W.L. Woodley, P.G. Grube, D.W. Martin, J. Stout and D.N. Sikdar, 1978: Rain estimation from geosynchronous satellite imagery--Visible and infrared studies. Mon. Wea. Rev., 106, 1153-1171.

Houze, R.A., Jr., 1977: Structure and dynamics of a tropical squall-line system. Mon. Wea. Rev., 105, 1540-1567.

Houze, R.A., Jr., and A.K. Betts, 1981: Convection in GATE. Rev. of Geophysics and Space Physics, 19, 541-576.

Houze, R.A., Jr., S.G. Geotis, F.D. Marks, Jr., and A.K. West, 1981: Winter monsoon convection in the vicinity of North Borneo. Part I: Structure and time variation of the clouds and precipitation. Mon. Wea. Rev., 109, 1595-1614.

Johns, R.H., and W.D. Hirt, 1983: The derecho...A severe weather producing convective system. Preprints, 13th Conf. Severe Local Storms, Amer. Meteor. Soc., 17-20 October, Tulsa, Oklahoma, 178-181.

Johnson, R.H., and D.C. Kriete, 1982: Thermodynamic and circulation characteristics of winter monsoon tropical mesoscale convection. Mon. Wea. Rev., 110, 1898-1911.

Johnson, R.H., and D.L. Priegnitz, 1981: Winter monsoon convection in the vicinity of North Borneo. Part II: Effects on large-scale fields. Mon. Wea. Rev., 109, 1615-1628.

Johnson, R.H., and J.J. Toth, 1982: A climatology of the July 1981 surface flow over northeast Colorado. Atmospheric Science Paper No. 342, Department of Atmospheric Science, Colorado State University, Fort Collins, Colorado, 80523, 52 pp.

Kessler, E., Ed., 1982: Thunderstorms: A Social, Scientific, and Technological Documentary. Vol. 2: Thunderstorm Morphology and Dynamics. U.S. Dept. of Commerce, National Oceanic and Atmospheric Administration, Environmental Research Laboratories, 603 pp. [U.S. Government Printing Office, Washington, D.C. 20402, Accession No. C55/602/T42/v.2].

Kincer, J.B., 1916: Daytime and nighttime precipitation and their economic significance. Mon. Wea. Rev., 44, 628-633.

Leary, C.A., 1984: Precipitation structure of the cloud clusters in a tropical easterly wave. Mon. Wea. Rev., 112, 313-325.

Leary, C.A., and R.A. Houze, Jr., 1979a: The structure and evolution of convection in a tropical cloud cluster. J. Atmos. Sci., 36, 437-457.

Leary, C.A., and R.A. Houze, Jr., 1979b: Melting and evaporation of hydrometeors in precipitation from the anvil clouds of deep tropical convection. J. Atmos. Sci., 36, 669-679.

Leary, C.A., and E.N. Rappaport, 1983: Internal structure of a mesoscale convective complex. Preprints, 21st Conf. on Radar Meteorology, Amer. Meteor. Soc., 19-23 September, Edmonton, Alberta, 70-77.

Lilly, D.K., 1979: The dynamical structure and evolution of thunderstorms and squall lines. Ann. Rev. Earth Planet. Sci., 7, 117-161.

Maddox, R.A, 1980: Mesoscale convective complexes. Bull. Amer. Meteor. Soc., 61, 1374-1387.

Maddox, R.A., 1981: The structure and life-cycle of midlatitude mesoscale convective complexes. Atmospheric Science Paper No. 336, Dept. of Atmospheric Science, Colorado State University, Fort Collins, Colorado, 80523, 311 pp.

Maddox, R.A., 1983: Large-scale meteorological conditions associated with midlatitude, mesoscale convective complexes. Mon. Wea. Rev., 111, 1475-1493.

Maddox, R.A., and C.A. Doswell, III, 1982: An examination of jet stream configurations, 500 mb vorticity advection and low-level thermal advection patterns during extended periods of intense convection. Mon. Wea. Rev., 110, 184-197.

Maddox, R.A., D.M. Rodgers and K.W. Howard, 1982: Mesoscale convective complexes over the United States during 1981--Annual summary. Mon. Wea. Rev., 110, 1501-1514.

McBride, J.L., 1981: Observational analysis of tropical cyclone formation. Part I: Basic description of data sets. J. Atmos. Sci., 38, 1117-1131.

McBride, J.L., and R. Zehr, 1981: Observational analysis of tropical cyclone formation. Part II: Comparison of non-developing versus developing systems. J. Atmos. Sci., 38, 1132-1151.

Means, L.L., 1952: On thunderstorm forecasting in the central United States. Mon. Wea. Rev., 80, 165-189.

Merritt, J.H., and J.M. Fritsch, 1984: On the movement of the heavy precipitation areas of mid-latitude mesoscale convective complexes. Preprints, 10th Conf. on Wea. Forecasting and Analysis, Amer. Meteor. Soc., 25-29 June, Clearwater Beach, Florida, 529-536.

Miller, R.C., 1972: Notes on analysis and severe-storm forecasting procedures of the Air Force Global Weather Central. Tech. Report 200 (Rev), Air Weather Service (MAC), United States Air Force, 190 pp. [NTIS No. AD-744 042].

Moore, P.L., A.D. Cummings and D.L. Smith, 1974: The National Weather Service Manually Digitized Radar program and its application to precipitation probability forecasting. Preprints, Fifth Conf. on Wea. Forecasting and Anal., Amer. Meteor. Soc., 4-7 March, St. Louis, Missouri, 69-74.

Newton, C.W., 1966: Circulations in large sheared cumulonimbus. Tellus, 18, 699-713.

Ogura, Y., and Y.-L. Chen, 1977: A life history of an intense mesoscale convective storm in Oklahoma. J. Atmos. Sci., 34, 1458-1476.

Ogura, Y., and M.-T. Liou, 1980: The structure of a midlatitude squall line: A case study. J. Atmos. Sci., 37, 553-567.

Orlanski, I., 1975: A rational subdivision of scales for atmospheric processes. Bull. Amer. Meteor. Soc., 56, 527-530.

Paegle, J., 1978: A linearized analysis of diurnal boundary layer convergence over the topography of the United States. Mon. Wea. Rev., 106, 492-502.

Palmen, E., and C.W. Newton, 1969: Atmospheric Circulation Systems; Their Structure and Physical Interpretation. International Geophysics Series, Vol. 13, Academic Press, Inc., 603 pp.

Porter, J.M., L.L. Means, J.E. Hovde and W.B. Chappell, 1955: A synoptic study on the formation of squall lines in the north central United States. Bull. Amer. Meteor. Soc., 36, 390-396.

Purdom, J.F.W., 1979: The development and evolution of deep convection. Preprints, 11th Conf. on Severe Local Storms, Amer. Meteor. Soc., 2-5 October, Kansas City, Missouri, 143-150.

Rockwood, A.A., D.L. Bartels and R.A. Maddox, 1984: Precipitation characteristics of a dual mesoscale convective complex. NOAA Tech. Memo. ERL ESG-6, Dept. of Commerce, National Oceanic and Atmospheric Administration, Environmental Research Laboratories, Environmental Sciences Group, Boulder, Colorado, 80303, 50 pp.

Rodgers, D.M., K.W. Howard and E.C. Johnston, 1983: Mesoscale convective complexes over the United States during 1982. Mon. Wea. Rev., 111, 2363-2369.

Sanders, F., and K.A. Emanuel, 1977: The momentum budget and temporal evolution of a mesoscale convective system. J. Atmos. Sci., 34, 322-330.

Schroeder, M.J., and G.E. Klazura, 1978: Computer processing of digital radar data gathered during HIPLEX. J. Appl. Meteor., 17, 498-507.

Scofield, R.A., and V.J. Oliver, 1977: A scheme for estimating convective rainfall from satellite imagery. NOAA Tech. Memo. NESS 86, U.S. Dept. of Commerce, National Oceanic and Atmospheric Administration, National Environmental Satellite, Data, and Information Service, 47 pp. [NTIS No. PB-270 762/8GI].

Wallace, J.M., 1975: Diurnal variations in precipitation and thunderstorm frequency over the conterminous United States. Mon. Wea. Rev., 103, 406-419.

Wetzel, P.J., W.R. Cotton and R.L. McAnelly, 1983: A long-lived mesoscale convective complex. Part II: Evolution and structure of the mature complex. Mon. Wea. Rev., 111, 1919-1937.

Zipser, E.J., 1977: Mesoscale and convective-scale downdrafts as distinct components of squall-line structure. Mon. Wea. Rev., 105, 1568-1589.

Zipser, E.J., R.J. Meitin and M.A. LeMone, 1981: Mesoscale motion fields associated with a slowly moving GATE convective band. J. Atmos. Sci., 38, 1725-1750.

LIST OF TABLES

FIGURE LEGENDS

Fig. 1. Tracks of the centroids of the 14 mesoscale convective systems which attained MCC dimensions (darkened track) during the episode of 3-10 August 1977, based on 3-h interval analysis of geosynchronous, infrared satellite data. Circled system numbers indicate the chronological order of their initial appearances. The date is given near each 0000 GMT symbol. Smoothed terrain heights are indicated by solid contours at 600-m intervals and the dashed 300-m contour. [Adapted from Wetzel _et al_. (1983)].

Fig. 2. Radar and hourly precipitation networks over the MCC study area (refer to legend in figure for plotting conventions). PPI film was acquired from the six National Weather Service WSR-57 (10-cm) radars at Limon, CO (LIC), Grand Island, NE (GRI), Des Moines, IA (DSM), Garden City (GCK), and Wichita (ICT), KS, and Kansas City, MO (MKC). Their maximum ranges and higher-resolved coverages are indicated. Radars at GCK and MKC had VIP display capability. Radar observation logs were obtained from these six sites and the NWS radar sites at Alliance, NE (AIA), Oklahoma City, OK (OKC), and Monett, MO (UMN). Also used were 5-cm radar data from the HIPLEX site at Goodland, KS (GLD). The small closed and open circles represent operable sites of recording raingages with increments of 0.25 and 2.5 mm , respectively. Shaded regions are examples of hourly rainfall envelopes associated with the eastern MCC #6 and the western MCC #12, whose satellite-observed cloud shields are represented by the re-mapped IR isotherms of -32 and -53°C (thin solid contours). For each MCC, an example of calculating an hourly envelope's area (A), average rainfall ($\bar{R}$) and volume (V) from its number (N) of measurable reports (plotted in mm) is given.

Fig. 3. Enhanced IR GOES-east satellite images spanning the life-cycle of the western MCC #1 through the night of 3-4 Aug 1977. Central Standard Time is 6 h earlier than the indicated GMT time. The stepped shades of medium gray, light gray, dark grey and black are thresholds for areas with apparent blackbody temperatures colder than -32, -42, -53 and -59°C, respectively. Temperatures progressively colder than -63°C appear as a gradual black-to-white shade. The grid in the 0900 GMT image is positioned about 150 km too far northward. A distance scale is indicated over Nebraska in (g). The life-cycle terminology is described in the text.

Fig. 4. Stratification of twelve MCCs into four composite categories by geographical genesis region and maximum anvil size. Each MCC is represented by a time scale labelled in GMT hours and is fitted to its composite time scale according to the IR-defined characteristics (defined in text) of "start", "maximum" and "end" (vertical dashed lines). Also indicated are the times of other IR-defined characteristics: a meso-α-scale "cellular" stage (in brackets); an "overshooting-top" maximum intensity (circled); and the maximum size of the -32°C IR area (asterisk). Based on a total accumlated hourly rainfall volume from 2 h prior to "start" to "end", the timing of the total's quartiles is indicated by the appropriately shaded circles under each MCC time scale. The composite MCC for each category, labelled with an hourly time scale "starting" at hour 0, is based on the average timing and durations of these IR and precipitation characteristics for the three individual MCCs. The timing of the composite IR features is rounded to the nearest whole MCC hour.

Fig. 5. Synoptic conditions at 0000 GMT 4 Aug 1977, near the development time of the western MCC #1 (refer to legends in figure for analysis and plotting conventions). (a) Low to mid-tropospheric features. Analyzed fields include 700-mb heights, 850 to 700-mb thicknesses and surface to 500-mb precipitable water. Shaded region highlights area of most pronounced convective instability, based on Lifted Index (L.I.) and Total-Totals Index (T.T.). Winds at 850, 700 and 500 mb are plotted at conventional rawinsonde sites (unlabelled) and at Limon, CO (LIC). (b) Surface features. Analyzed fields include sea-level pressure, temperature and dewpoint temperature. Winds and precipitation symbols are plotted at observation sites. Analyzed meteorological features are described in the figure legend.

Fig. 6. Composite IR satellite and radar analysis at 2-h intervals, from 01 to 11 GMT 4 Aug 1977, for the western MCC #1. The anvil cloud shields are indicated by the -32 and -53°C IR contours (outer and inner solid lines, respectively), re-mapped from satellite images at the labelled times. Darkly shaded regions (identified by letters) denote significant radar-observed, meso-β-scale convective features at about 25 min after the indicated IR whole hour, with the vectors showing their previous 2-h movements. The dashed line segments extending from the meso-β convective features indicate flanking axes of weaker convection. In the more developed MCC stages, in (e) and (f), the light-shaded area within the dashed envelope indicates weaker, more uniform and widespread echo.

Fig. 7. Synoptic analysis at 0000 GMT 5 Aug 1977, near the development time of the western MCC #2. (a) Low to mid-tropospheric features are as in Fig. 5a. An additional sounding was available at Goodland, KS (GLD). (b) Surface features are as in Fig. 5b.

Fig. 8 Composite IR satellite and radar analysis, from 01 to 11 GMT 5 Aug 1977, for the western MCC #2, similar to Fig. 6. Dashed portions of IR contours [as in northeast Kansas in (d)] are estimated positions when the contours are ill-defined in the imagery. The second time label in (c), 0525 GMT, denotes a radar analysis time differing from the hour of the IR image, 0430 GMT.

Fig. 9. Synoptic analysis at 0000 GMT 6 Aug 1977, near the development time of the western MCC #3. (a) Low to mid-tropospheric features are as in Fig. 5a. (b) Surface features are as in Fig. 5b.

Fig. 10. Composite IR satellite and radar analysis, from 22 GMT 5 Aug to 08 GMT 6 Aug 1977, for the western MCC #3, similar to Figs. 6 and 8. In (b), (c) and (d) the IR contours are -40 and -62°C.

Fig. 11. Synoptic analysis near the development time of the eastern MCC #6. (a) Low to mid-tropospheric features at 0000 GMT 7 Aug 1977 are as in Fig. 5a. (b) Surface features at 0300 GMT 7 Aug 1977 are as in Fig. 5b. The shaded region over Indiana denotes the IR cloud shield colder than $-32^{\circ}C$ associated with the small eastern MCC #4. The large thunderstorm symbol in northwest Missouri denotes the location of initial thunderstorm development for MCC #6.

Fig. 12. Composite IR satellite and radar analysis for the eastern MCC #6, similar to Figs. 6, 8 and 10. East of the area of reliable radar coverage, hatched envelopes denote regions of measurable precipitation for the hour ending on the whole hour after the indicated IR time.

Fig. 13. Trends of composite MCC anvil size, as defined by areas of cloud-top IR temperature colder than -32 and $-53^{\circ}C$ (upper and lower solid curves, respectively). Ratio of -53 to $-32^{\circ}C$ areas is given by the dashed line. IR features of the composites are as in Fig. 4.

Fig. 14. Trends of composite MCC measurable hourly precipitation area ($\bar{A}$, solid line), average hourly precipitation rate ($\bar{R}$, dashed line) and hourly precipitation volume ($\bar{V}$, bars). Precipitation volumes are partitioned between "core" and "peripheral" rainfall (dark and light shaded portions, respectively, and defined in text). 1-2-1 running averages (defined in text) of the individual MCCs' hourly values were used to compute the composite values. Hourly values are plotted at the end of the hour to which they apply. Noted IR features are as in Fig. 4.

Fig. 15. Trends of composite MCC frequency distributions of measurable hourly precipitation reports over various intensity categories, utilizing raingages with increments of 2.5 mm . Bars are partitioned into percentages of measurable reports contributed by each intensity category, shaded according to the key inset in the west-large composite. The contribution due to the lightest intensity category (reports of 2.5 mm) is represented by the distance from 100% line down to the top of the partitioned bars. The total sample size for each hour (No.) is the number of measurable reports summed over the three MCCs, and is plotted as the dashed line. The average hourly intensity of these reports ($\bar{R}$) is plotted as the solid line. Other details are as in Fig. 14.

Fig. 16. Trends of composite MCC frequency distributions of measurable hourly precipitation reports over various intensity categories, utilizing raingages with increments of 0.25 mm . Details are as in Fig. 15, except the lightest intensity category is for reports less than 2.5 mm .

Fig. 17. Trends of composite MCC frequency distributions of non-zero Manually Digitized Radar (MDR) blocks over various intensity categories (see Table 2). The dashed line gives the average number of non-zero MDR blocks, which is scaled to areal coverage on the right ordinate. Hourly values, applicable at about 30 min off the hour, are plotted at the end of that hour. The east-large composite includes data for MCC #6 and #9/10 only, as no data were available for MCC #8. Other details are as in Fig. 15.

Table 1

Table 1. Meso-α-scale statistics of the 12 MCCs studied quantitatively, stratified by genesis region and by maximum anvil size into four composite categories.

	LARGE MCCs					SMALL MCCs				
		Maximum IR Area (10^3 km^2)		Mature Duration (h)	Total Rainfall Volume (10^{-3}km^3)		Maximum IR Area (10^3 km^2)		Mature Duration (h)	Total Rainfall Volume (10^{-3}km^3)
		-53°C	-32°C				-53°C	-32°C		
WESTERN MCCs	#1	340	611	14	4867	#5a	101	218	9	109
	#2	252	383	16	6075	#11	86	155	7	289
	#3	238	386	13	6049	#12	138	208	8	855
	Western Large Average	277	460	14.3	5664	Western Small Average	108	194	8.0	418
EASTERN MCCs	#6	239	354	10	3540	#4	108	167	7	2516
	#8	307	562	13	8213	#5b	89	132	6	323
	#9/10	307	522	9	6964	#9	139	227	9	1221
	Eastern Large Average	284	479	10.7	6239	Eastern Small Average	112	175	7.3	1353

Table 2

Table 2: Manually Digitized Radar (MDR) data code

Code No.	Coverage in box	Maximum Reflectivity (dBZ)	Maximum Convective Rainfall Rate (mm/h), Category
0	No echo	N/A	0
1	Any VIP1	< 30	0-5, light
2	≤ 1/2 VIP2	30-40	6-27, moderate
3	> 1/2 VIP2		
4	≤ 1/2 VIP3	41-45	28-55, heavy
5	> 1/2 VIP3		
6	≤ 1/2 VIP3,4	46-49	56-114, very heavy
7	> 1/2 VIP3,4		
8	≤ 1/2 VIP3,4,5,6	50-56	115-180, intense
9	> 1/2 VIP3,4,5,6	or > 56	or > 180, extreme

Fig. 1

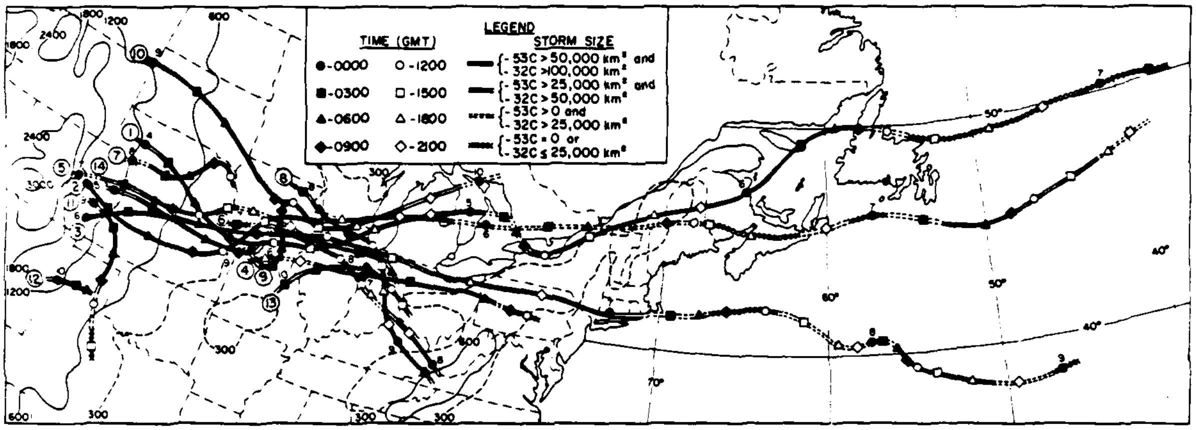

Fig. 1. Tracks of the centroids of the 14 mesoscale convective systems which attained MCC dimensions (darkened track) during the episode of 3-10 August 1977, based on 3-h interval analysis of geosynchronous, infrared satellite data. Circled system numbers indicate the chronological order of their initial appearances. The date is given near each 0000 GMT symbol. Smoothed terrain heights are indicated by solid contours at 600-m intervals and the dashed 300-m contour. [Adapted from Wetzel et al. (1983)].

Fig. 2

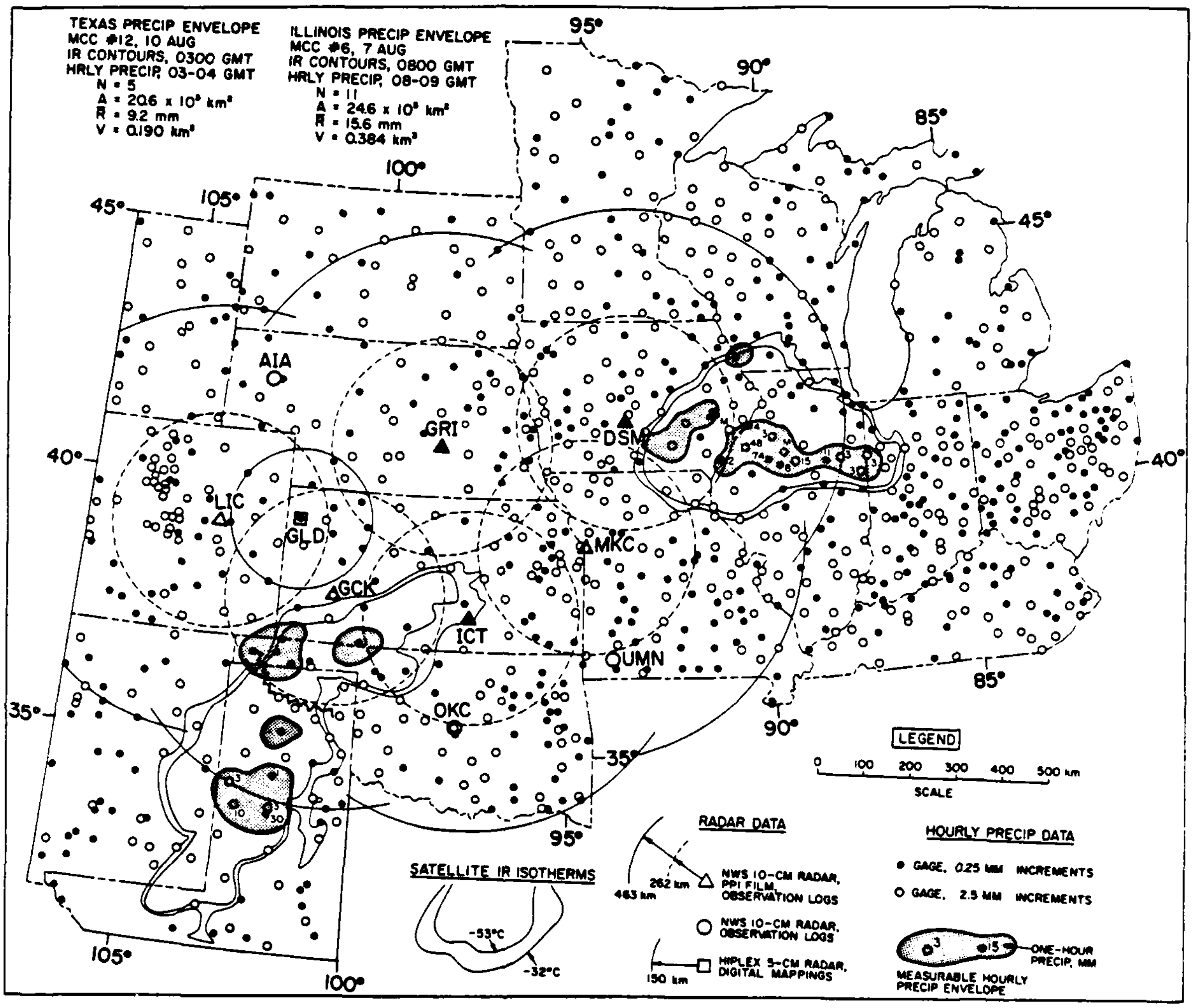

Fig. 2. Radar and hourly precipitation networks over the MCC study area (refer to legend in figure for plotting conventions). PPI film was acquired from the six National Weather Service WSR-57 (10-cm) radars at Limon, CO (LIC), Grand Island, NE (GRI), Des Moines, IA (DSM), Garden City (GCK), and Wichita (ICT), KS, and Kansas City, MO (MKC). Their maximum ranges and higher-resolved coverages are indicated. Radars at GCK and MKC had VIP display capability. Radar observation logs were obtained from these six sites and the NWS radar sites at Alliance, NE (AIA), Oklahoma City, OK (OKC), and Monett, MO (UMN). Also used were 5-cm radar data from the HIPLEX site at Goodland, KS (GLD). The small closed and open circles represent operable sites of recording raingages with increments of 0.25 and 2.5 mm, respectively. Shaded regions are examples of hourly rainfall envelopes associated with the eastern MCC #6 and the western MCC #12, whose satellite-observed cloud shields are represented by the re-mapped IR isotherms of -32 and -53°C (thin solid contours). For each MCC, an example of calculating an hourly envelope's area (A), average rainfall (R) and volume (V) from its number (N) of measurable reports (plotted in mm) is given.

Fig. 3

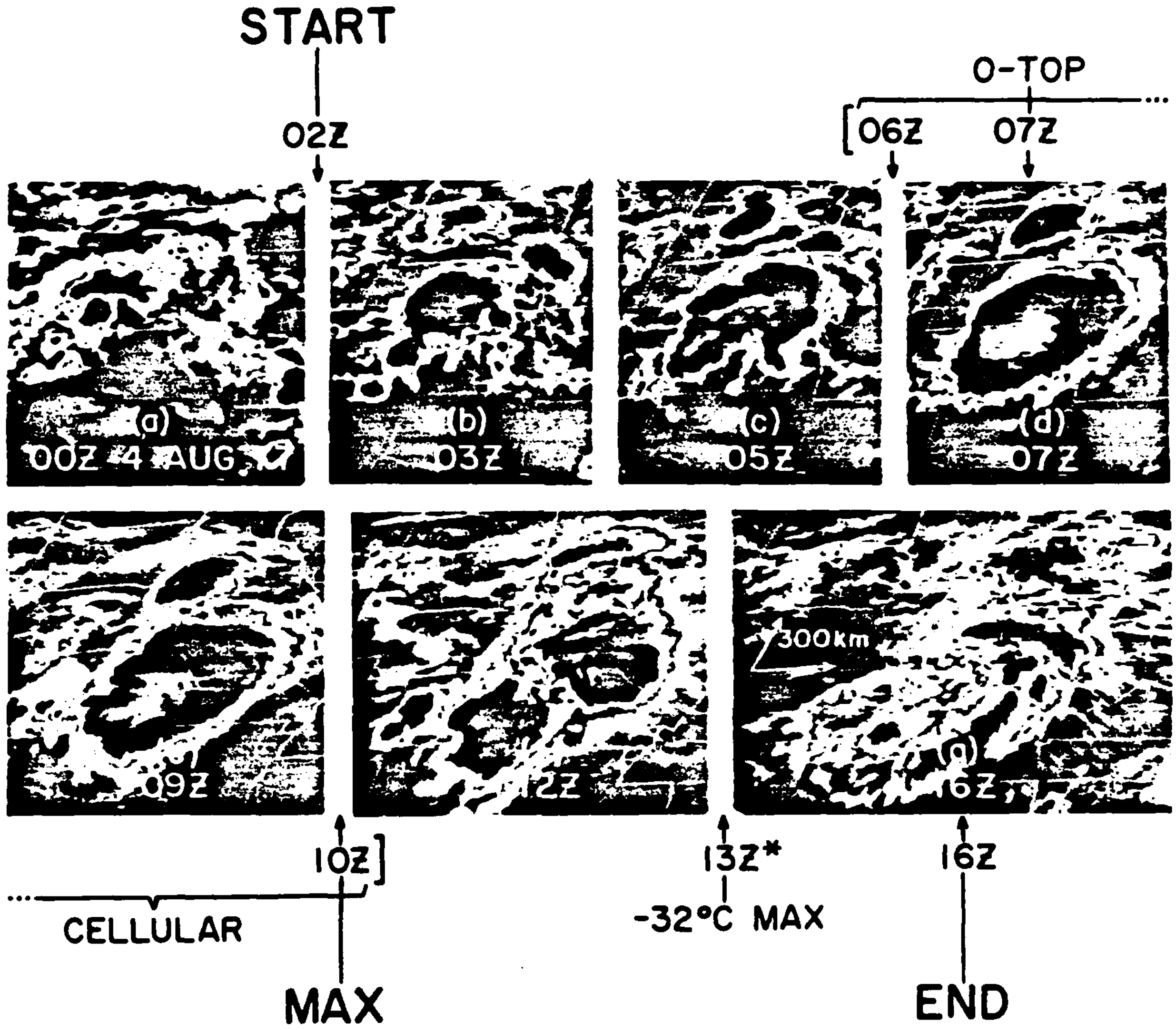

Fig. 3. Enhanced IR GOES-east satellite images spanning the life-cycle of the western MCC #1 through the night of 3-4 Aug 1977. Central Standard Time is 6 h earlier than the indicated GMT time. The stepped shades of medium gray, light gray, dark grey and black are thresholds for areas with apparent blackbody temperatures colder than -32, -42, -53 and -59°C, respectively. Temperatures progressively colder than -63°C appear as a gradual black-to-white shade. The grid in the 0900 GMT image is positioned about 150 km too far northward. A distance scale is indicated over Nebraska in (g). The life-cycle terminology is described in the text.

Fig. 4

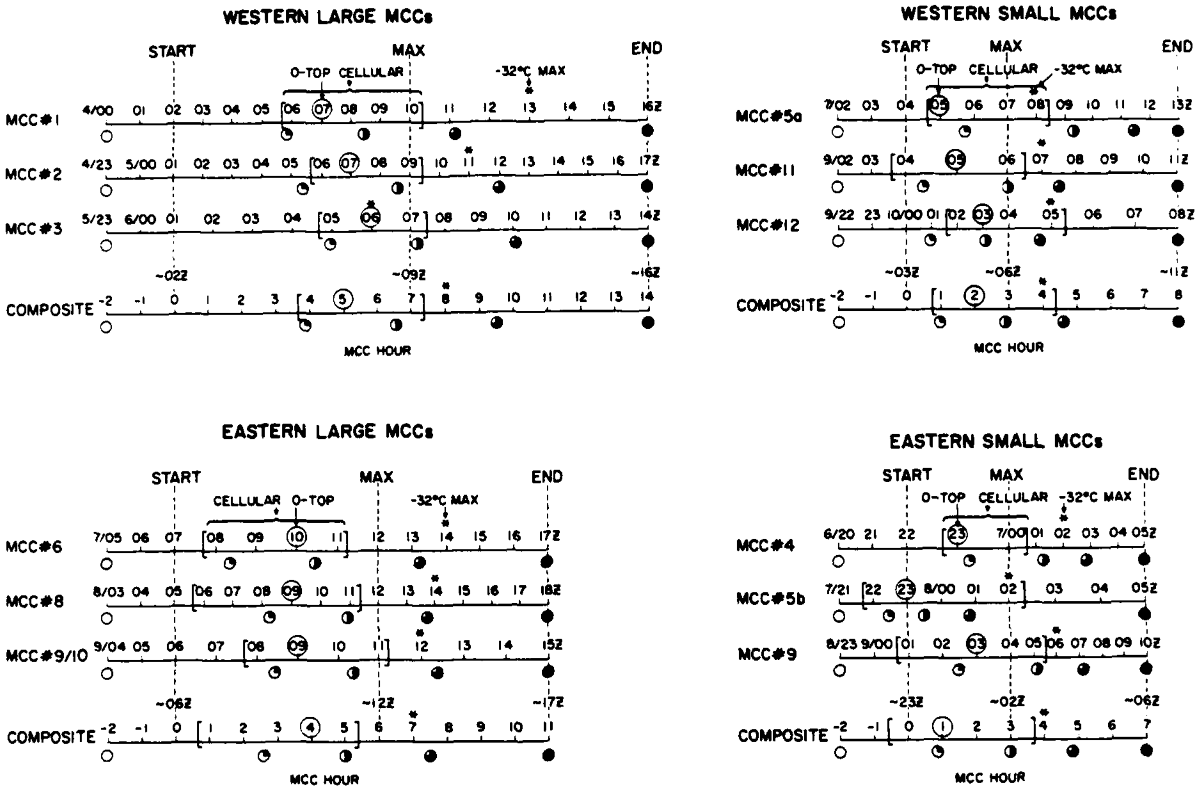

Fig. 4. Stratification of twelve MCCs into four composite categories by geographical genesis region and maximum anvil size. Each MCC is represented by a time scale labelled in GMT hours and is fitted to its composite time scale according to the IR-defined characteristics (defined in text) of "start", "maximum" and "end" (vertical dashed lines). Also indicated are the times of other IR-defined characteristics: a meso-α-scale "cellular" stage (in brackets); an "overshooting-top" maximum intensity (circled); and the maximum size of the $-32^{\circ}C$ IR area (asterisk). Based on a total accumulated hourly rainfall volume from 2 h prior to "start" to "end", the timing of the total's quartiles is indicated by the appropriately shaded circles under each MCC time scale. The composite MCC for each category, labelled with an hourly time scale "starting" at hour 0, is based on the average timing and durations of these IR and precipitation characteristics for the three individual MCCs. The timing of the composite IR features is rounded to the nearest whole MCC hour.

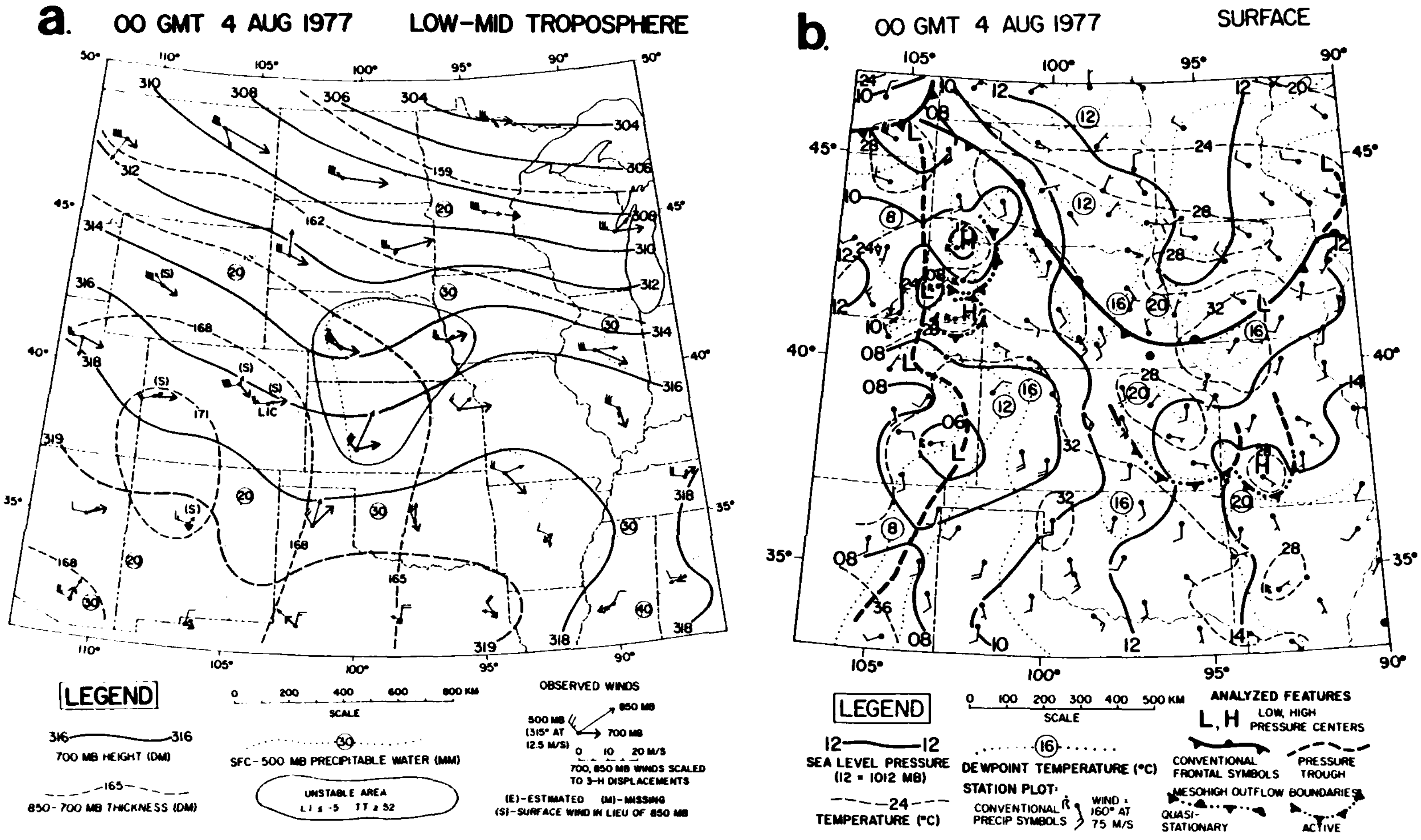

Fig. 5. Synoptic conditions at 0000 GMT 4 Aug 1977, near the development time of the western MCC #1 (refer to legends in figure for analysis and plotting conventions). (a) Low to mid-tropospheric features. Analyzed fields include 700-mb heights, 850 to 700-mb thicknesses and surface to 500-mb precipitable water. Shaded region highlights area of most pronounced convective instability, based on Lifted Index (L.I.) and Total-Totals Index (T.T.). Winds at 850, 700 and 500 mb are plotted at conventional rawinsonde sites (unlabelled) and at Limon, CO (LIC). (b) Surface features. Analyzed fields include sea-level pressure, temperature and dewpoint temperature. Winds and precipitation symbols are plotted at observation sites. Analyzed meteorological features are described in the figure legend.

Fig. 5

Fig. 6

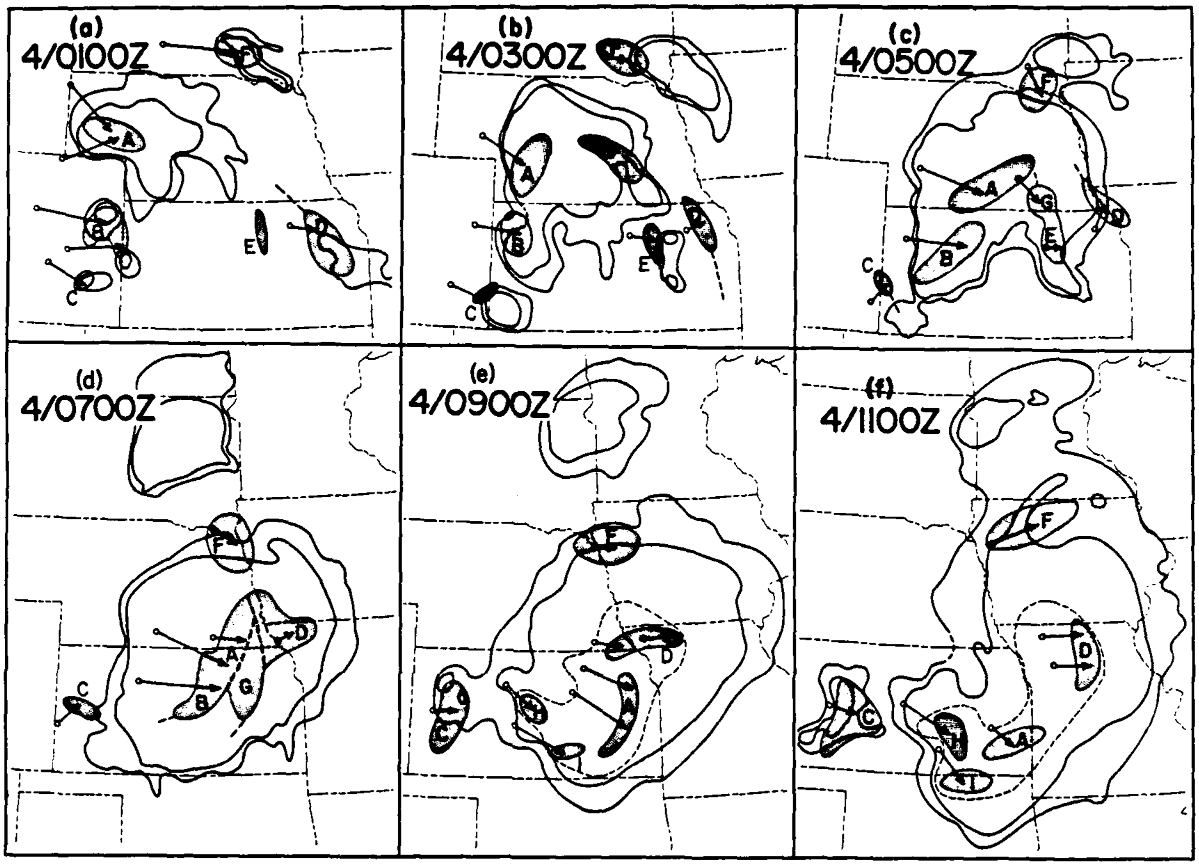

Fig. 6. Composite IR satellite and radar analysis at 2-h intervals, from 01 to 11 GMT 4 Aug 1977, for the western MCC #1. The anvil cloud shields are indicated by the -32 and -53°C IR contours (outer and inner solid lines, respectively), re-mapped from satellite images at the labelled times. Darkly shaded regions (identified by letters) denote significant radar-observed, meso-β-scale convective features at about 25 min after the indicated IR whole hour, with the vectors showing their previous 2-h movements. The dashed line segments extending from the meso-β convective features indicate *flanking axes of* weaker convection. In the more developed MCC stages, in (e) and (f), the light-shaded area within the dashed envelope indicates weaker, more uniform and widespread echo.

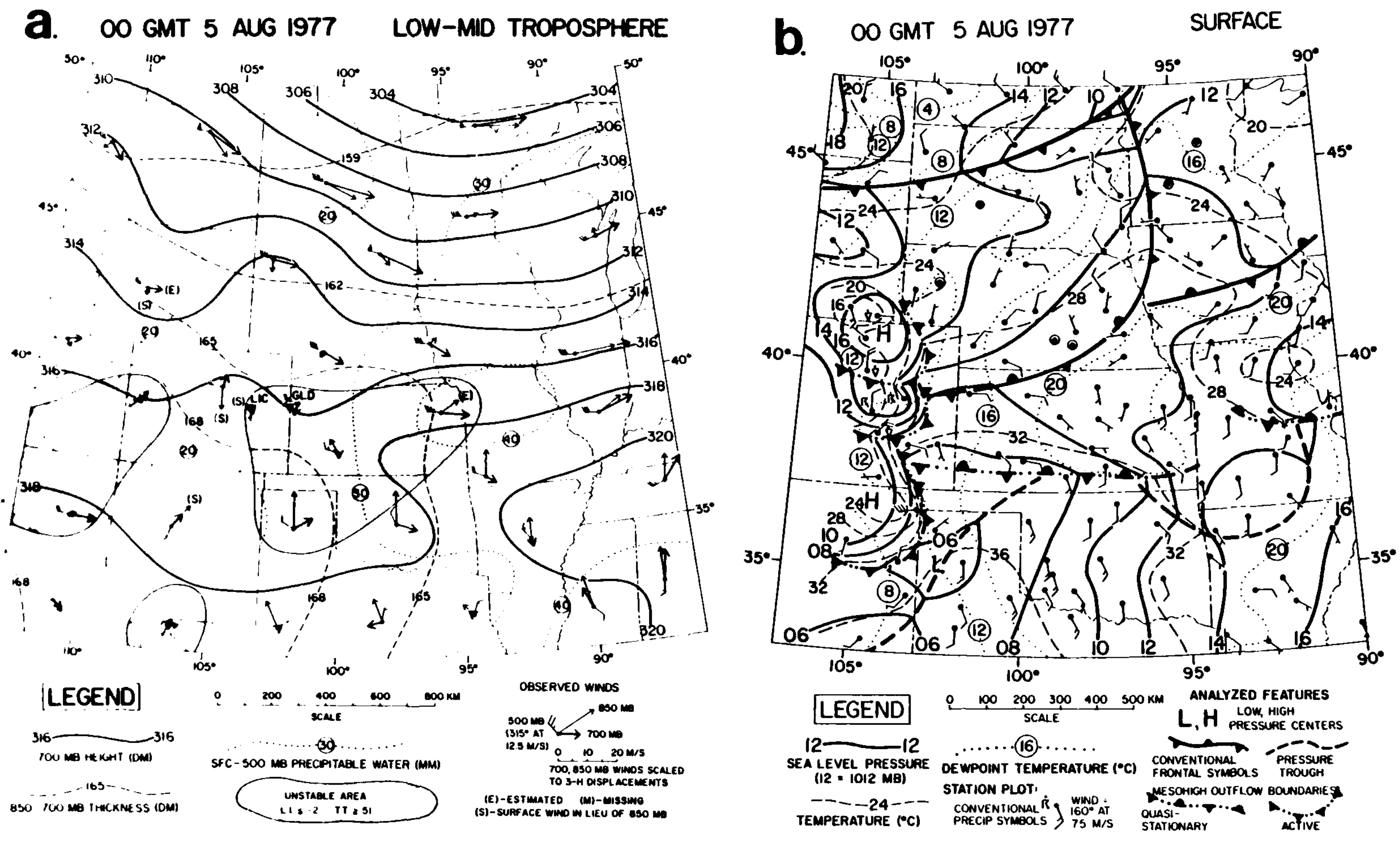

a. 00 GMT 5 AUG 1977 LOW-MID TROPOSPHERE

b. 00 GMT 5 AUG 1977 SURFACE

Fig. 7. Synoptic analysis at 0000 GMT 5 Aug 1977, near the development time of the western MCC #2. (a) Low to mid-tropospheric features are as in Fig. 5a. An additional sounding was available at Goodland, KS (GLD). (b) Surface features are as in Fig. 5b.

Fig. 7

Fig. 8

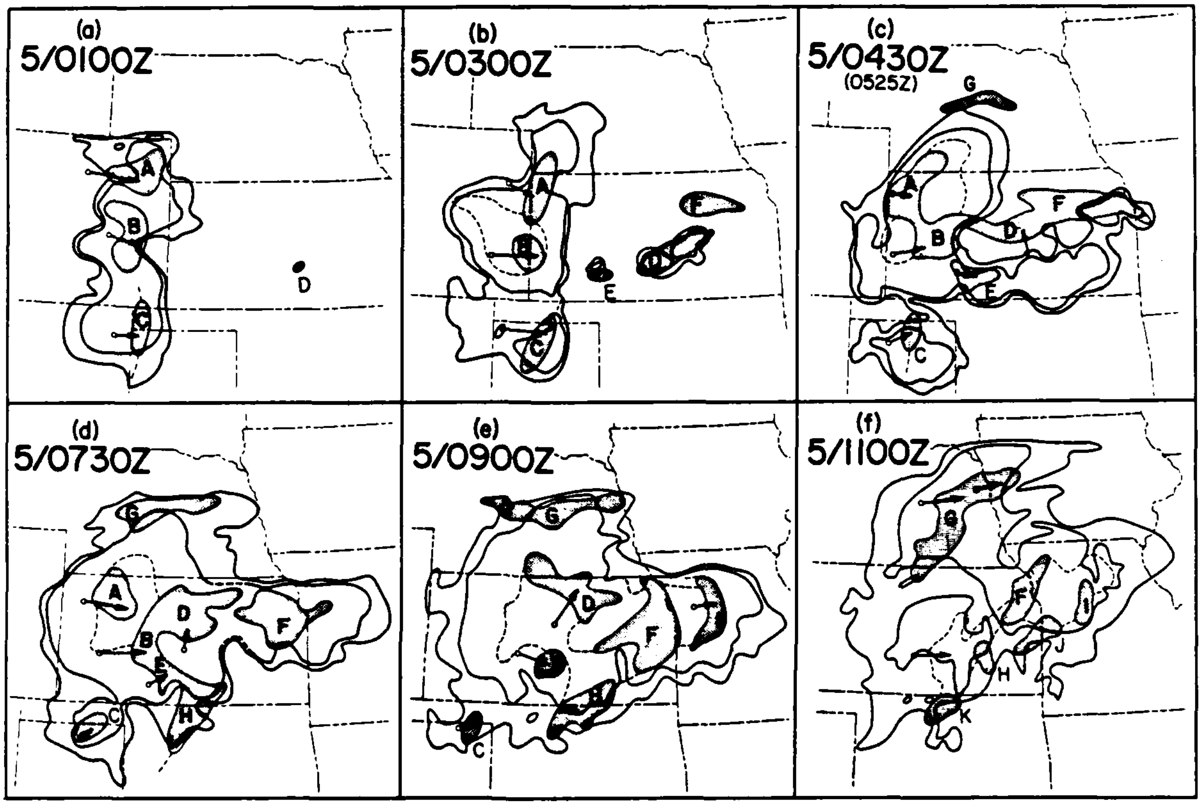

Fig. 8 Composite IR satellite and radar analysis, from 01 to 11 GMT 5 Aug 1977, for the western MCC #2, similar to Fig. 6. Dashed portions of IR contours [as in northeast Kansas in (d)] are estimated positions when the contours are ill-defined in the imagery. The second time label in (c), 0525 GMT, denotes a radar analysis time differing from the hour of the IR image, 0430 GMT.

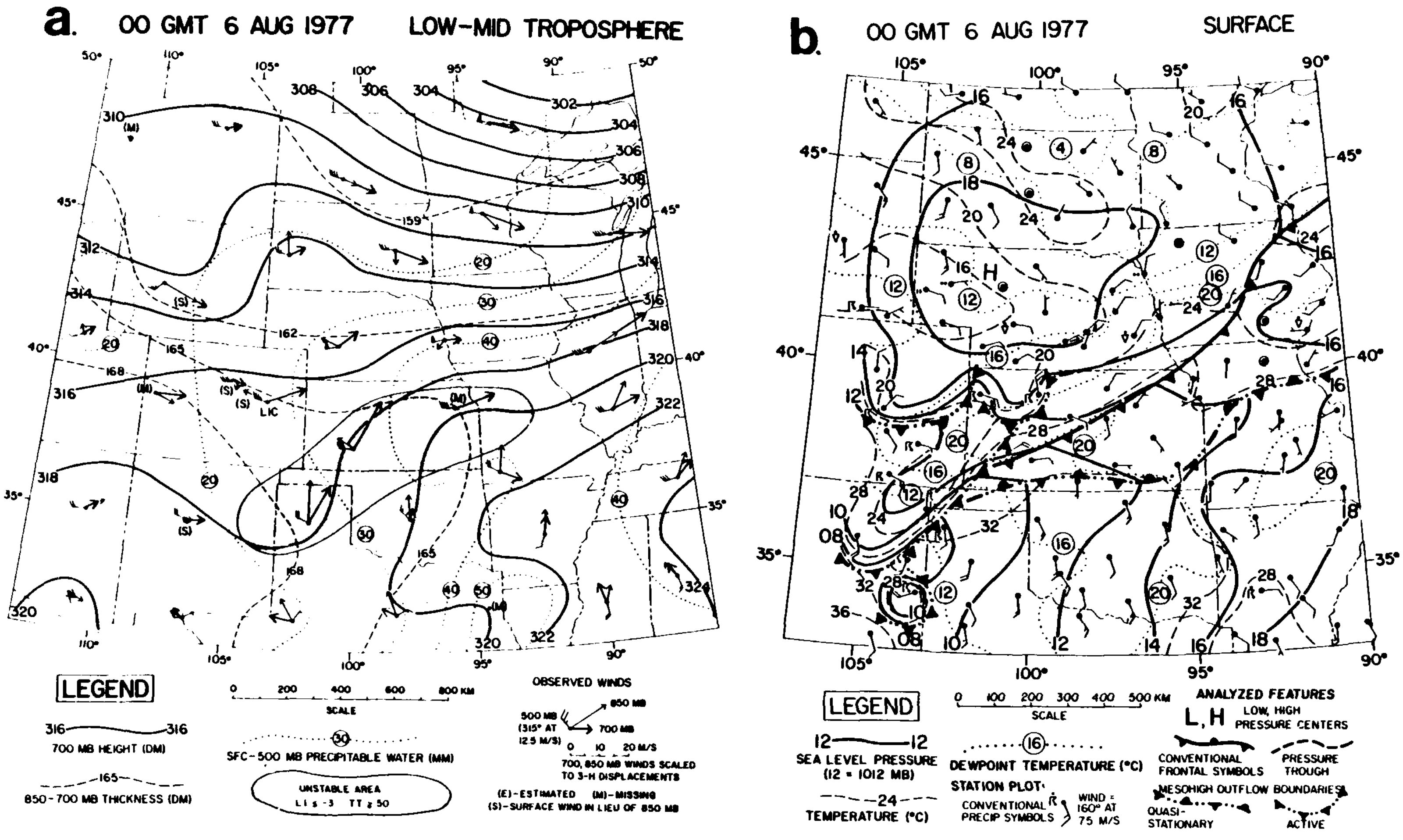

Fig. 9. Synoptic analysis at 0000 GMT 6 Aug 1977, near the development time of the western MCC #3. (a) Low to mid-tropospheric features are as in Fig. 5a. (b) Surface features are as in Fig. 5b.

Fig. 9

Fig. 10

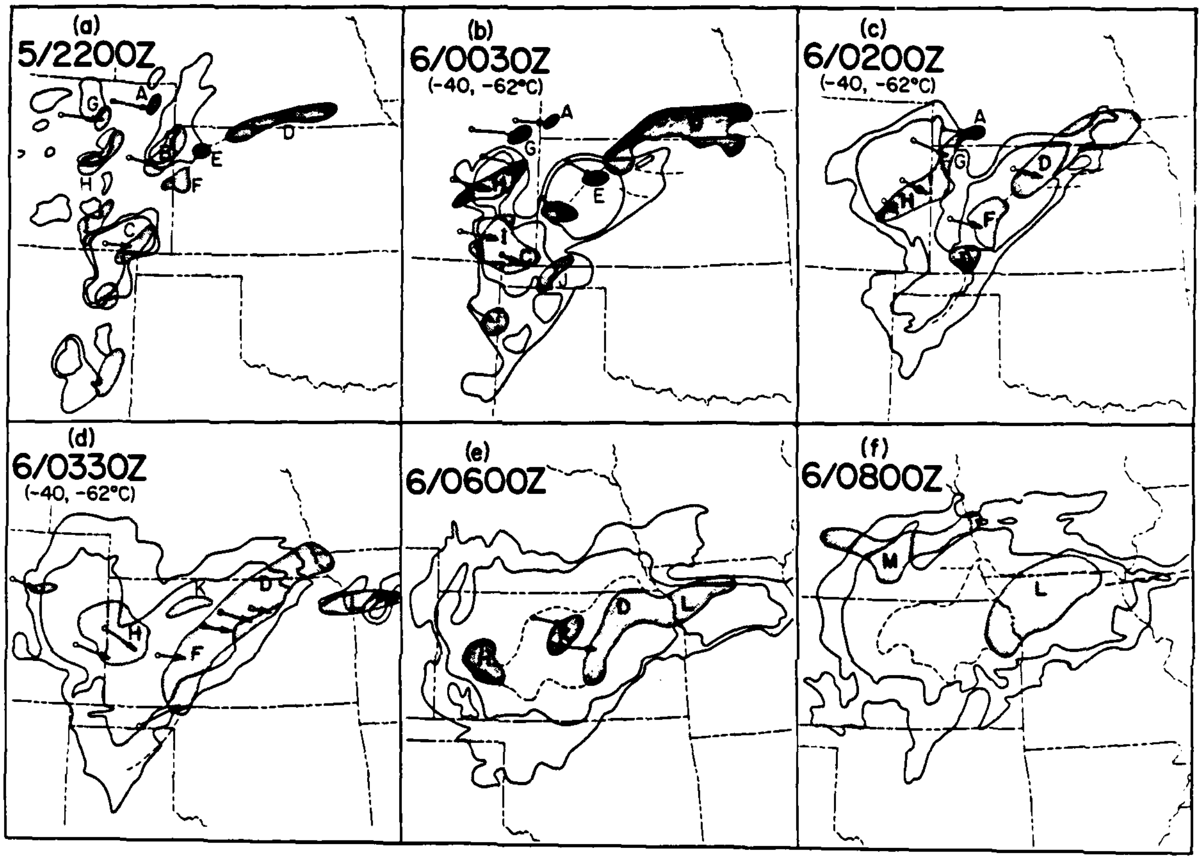

Fig. 10. Composite IR satellite and radar analysis, from 22 GMT 5 Aug to 08 GMT 6 Aug 1977, for the western MCC #3, similar to Figs. 6 and 8. In (b), (c) and (d) the IR contours are -40 and -62°C.

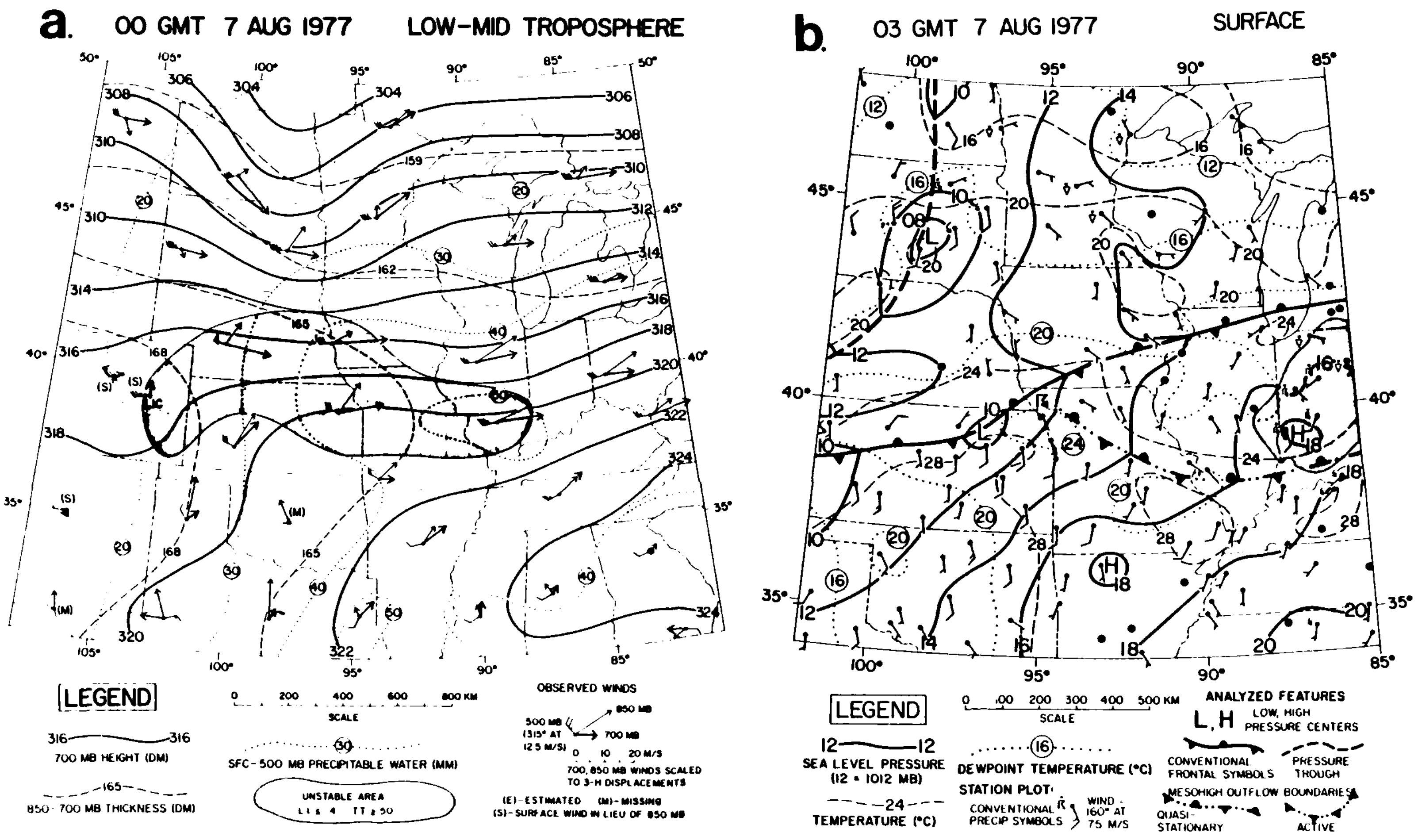

Fig. 11. Synoptic analysis near the development time of the eastern MCC #6. (a) Low to mid-tropospheric features at 0000 GMT 7 Aug 1977 are as in Fig. 5a. (b) Surface features at 0300 GMT 7 Aug 1977 are as in Fig. 5b. The shaded region over Indiana denotes the IR cloud shield colder than -32°C associated with the small eastern MCC #4. The large thunderstorm symbol in northwest Missouri denotes the location of initial thunderstorm development for MCC #6.

Fig. 11

Fig. 12

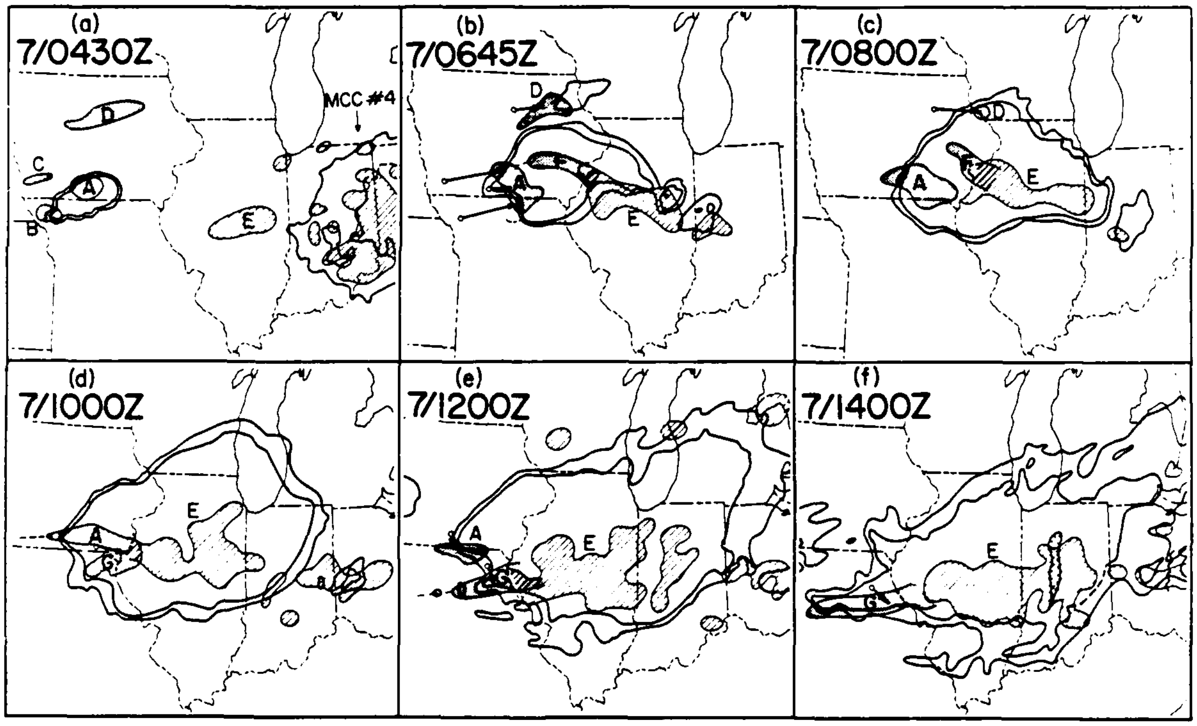

Fig. 12. Composite IR satellite and radar analysis for the eastern MCC #6, similar to Figs. 6, 8 and 10. East of the area of reliable radar coverage, hatched envelopes denote regions of measurable precipitation for the hour ending on the whole hour after the indicated IR time.

Fig. 13

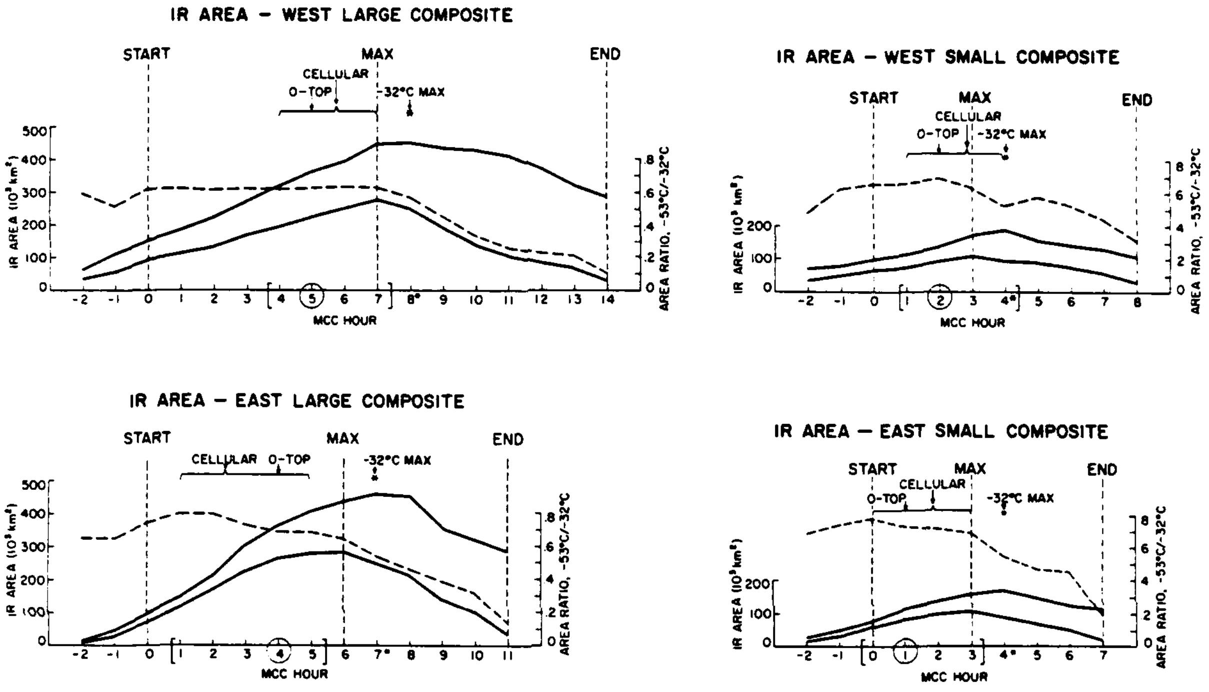

Fig. 13. Trends of composite MCC anvil size, as defined by areas of cloud-top IR temperature colder than -32 and -53°C (upper and lower solid curves, respectively). Ratio of -53 to -32°C areas is given by the dashed line. IR features of the composites are as in Fig. 4.

Fig. 14

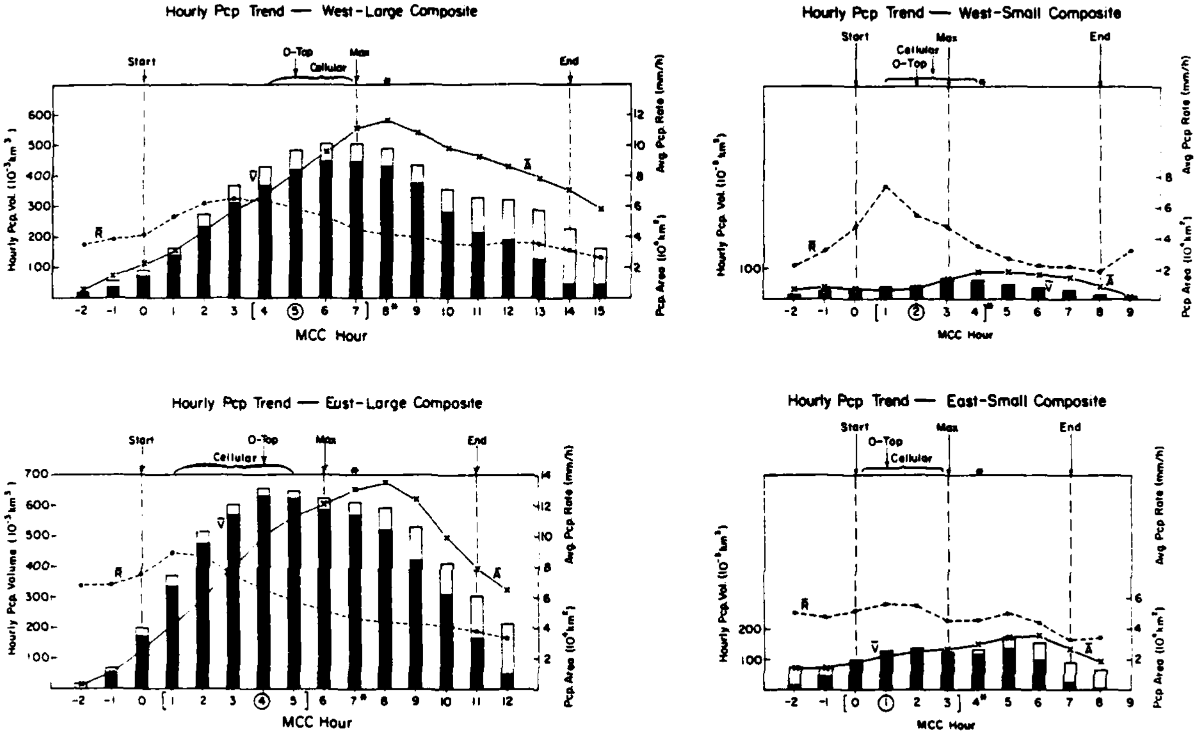

Fig. 14. Trends of composite MCC measurable hourly precipitation area ($\bar{A}$, solid line), average hourly precipitation rate ($\bar{R}$, dashed line) and hourly precipitation volume ($\bar{V}$, bars). Precipitation volumes are partitioned between "core" and " peripheral" rainfall (dark and light shaded portions, respectively, and defined in text). 1-2-1 running averages (defined in text) of the individual MCCs' hourly values were used to compute the composite values. Hourly values are plotted at the end of the hour to which they apply. Noted IR features are as in Fig. 4.

Fig. 15

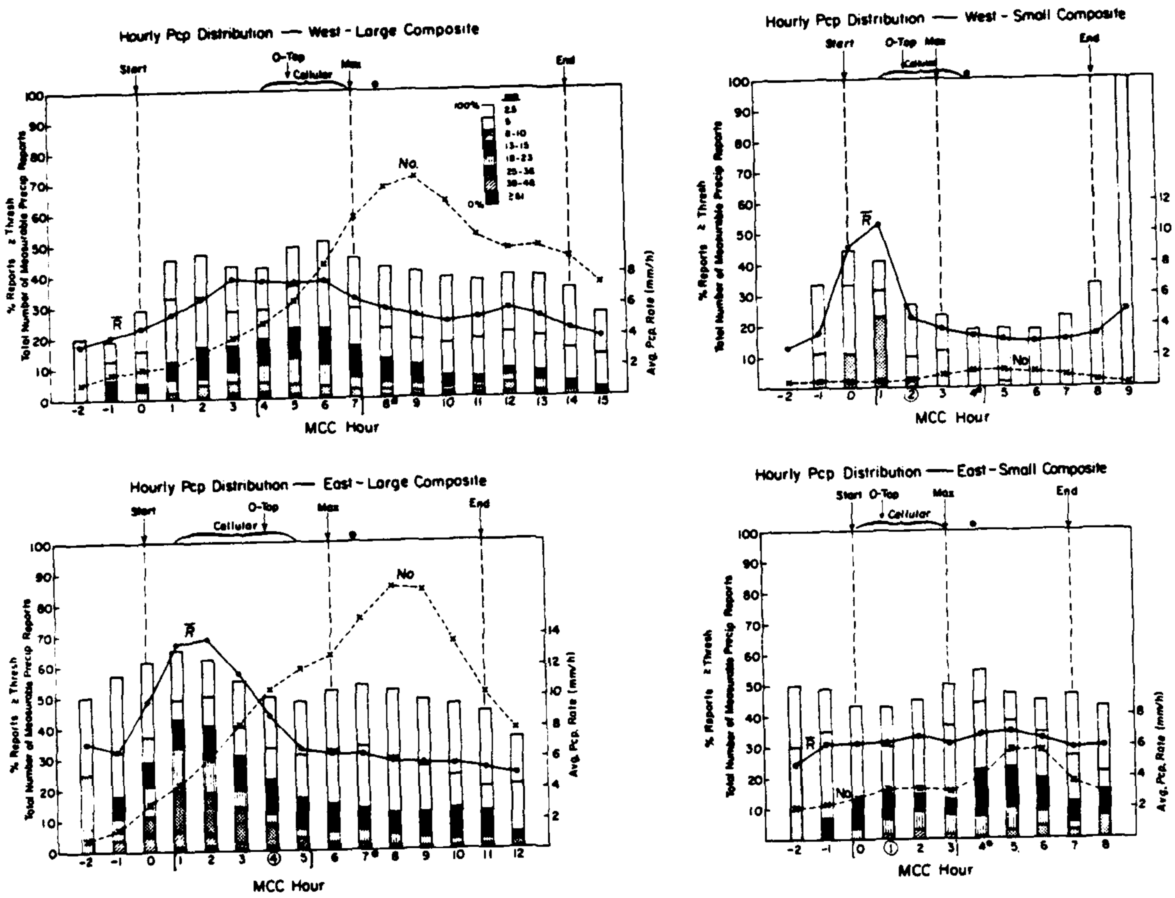

Fig. 15. Trends of composite MCC frequency distributions of measurable hourly precipitation reports over various intensity categories. utilizing raingages with increments of 2.5 mm . Bars are partitioned into percentages of measurable reports contributed by each intensity category, shaded according to the key inset in the west-large composite. The contribution due to the lightest intensity category (reports of 2.5 mm) is represented by the distance from 100% line down to the top of the partitioned bars. The total sample size for each hour (No.) is the number of measurable reports summed over the three MCCs, and is plotted as the dashed line. The average hourly intensity of these reports ($\bar{R}$) is plotted as the solid line. Other details are as in Fig. 14.

Fig. 16

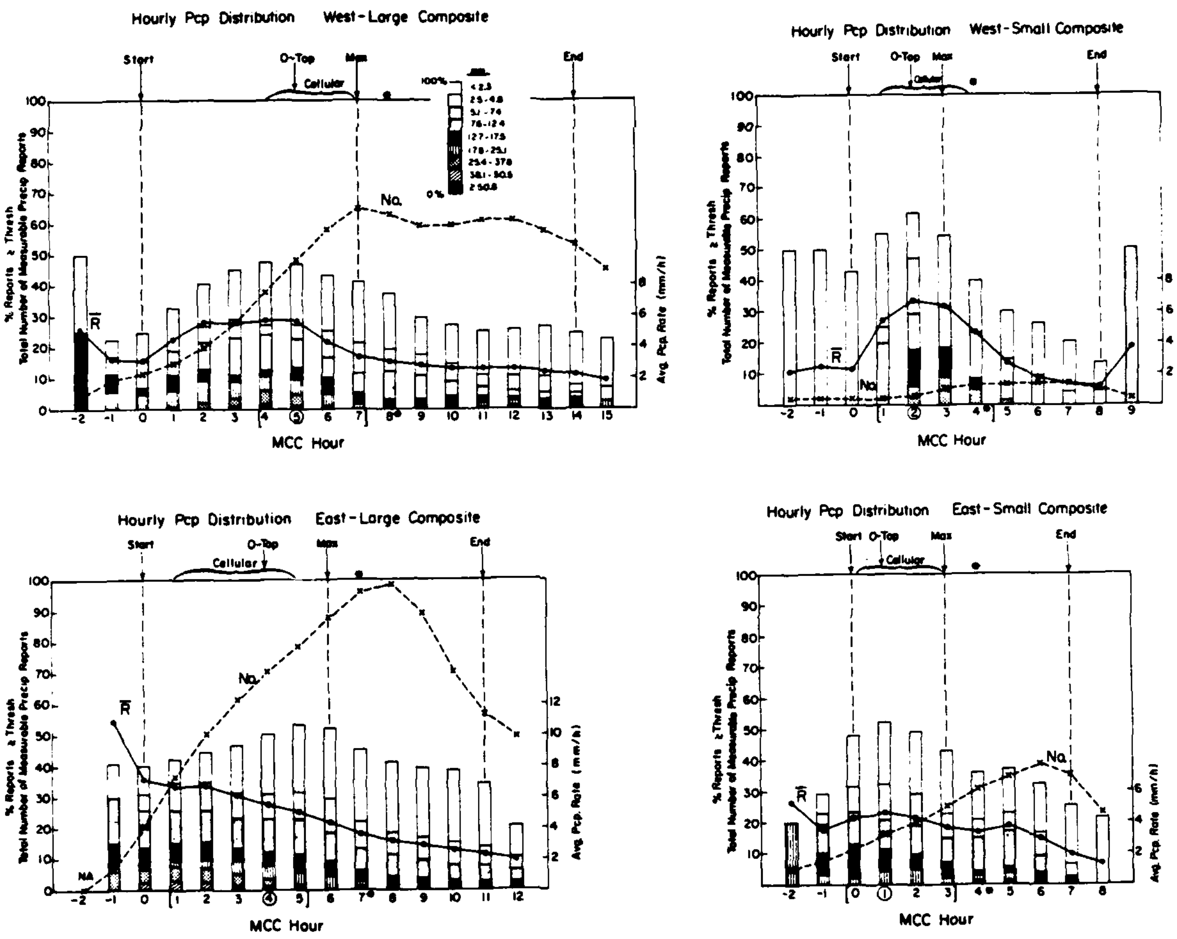

Fig. 16. Trends of composite MCC frequency distributions of measurable hourly precipitation reports over various intensity categories, utilizing raingages with increments of 0.25 mm. Details are *as in Fig. 15, except the lightest intensity category is for reports less than* 2.5 mm.

Fig. 17

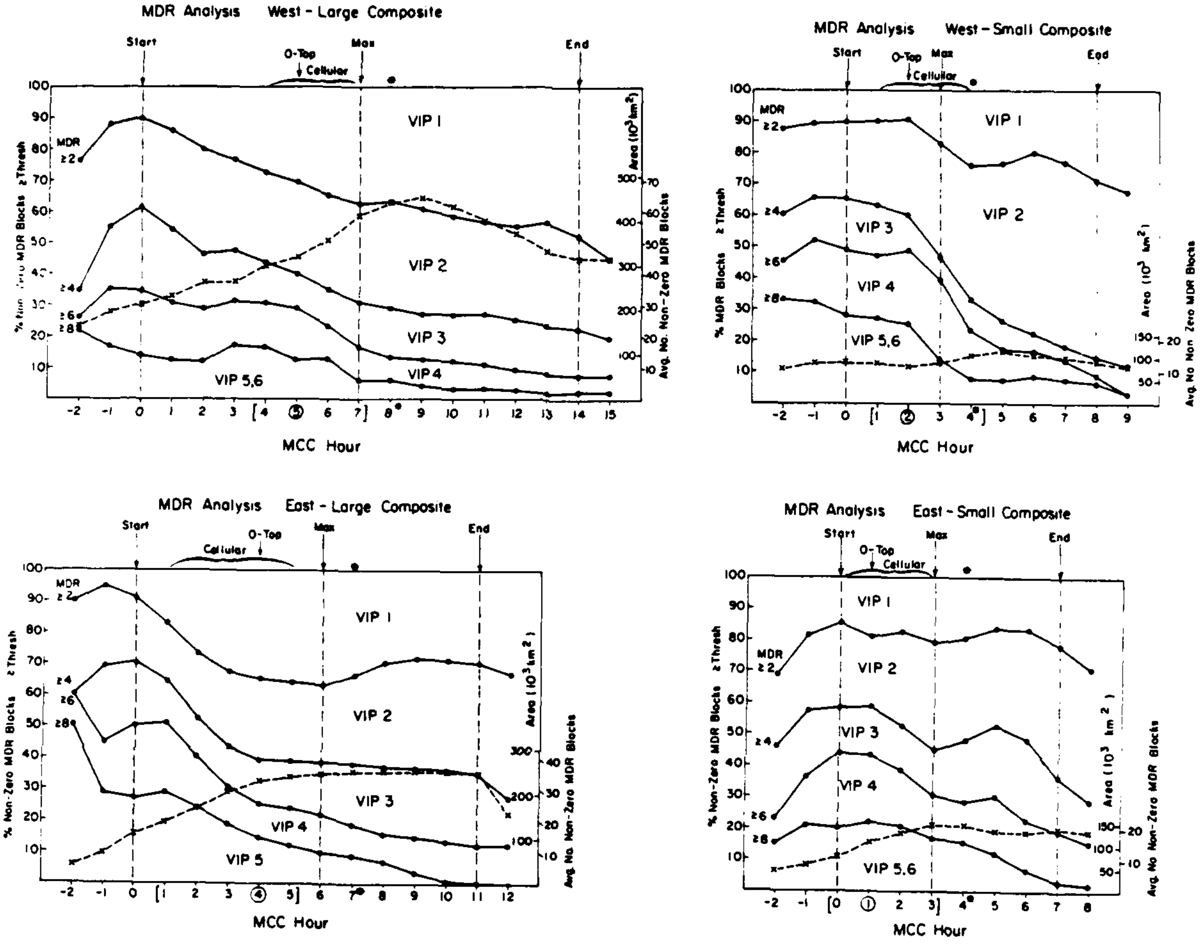

Fig. 17. Trends of composite MCC frequency distributions of non-zero Manually Digitized Radar (MDR) blocks over various intensity categories (see Table 2). The dashed line gives the average number of non-zero MDR blocks, which is scaled to areal coverage on the right ordinate. Hourly values, applicable at about 30 min off the hour, are plotted at the end of that hour. The east-large composite includes data for MCC #6 and #9/10 only, as no data were available for MCC #8. Other details are as in Fig. 15.

APPENDIX C

EVOLUTION OF PRECIPITATION AND UPPER AIR CHARACTERISTICS DURING THE LIFE-CYCLE OF A COMPOSITE MESOSCALE CONVECTIVE COMPLEX

by

Marjorie A. Klitch

EVOLUTION OF PRECIPITATION AND UPPER AIR CHARACTERISTICS DURING THE LIFE-CYCLE OF A COMPOSITE MESOSCALE CONVECTIVE COMPLEX

I. Background

Until the advent of geostationary satellites, Mesoscale Convective Complexes (MCCs) went virtually unnoticed because, due to their size ($\geq$100,000 km^2) and duration ($\geq$6 hours), they could not be resolved on the 12-hour synoptic network. After being identified in the late 1970s by Maddox (1981) and others, MCCs were defined in terms of satellite observations. Evolution of precipitation and other physical characteristics could only be inferred from satellite data. Maddox (1981) attempted to reveal some of the physical characteristics of the atmosphere before, during, and after the dissipation of MCCs. However, the 12-hour frequency of the rawinsonde network prevented fine resolution of the physical characteristics of MCC evolution.

II. Compositing Approach

While Maddox chose cases for compositing so that synoptic times would fall approximately within the same stage of an MCCs presumed life cycle, the research outlined here takes a different approach. A large number of cases were included so synoptic times would fall in all periods of the MCC life cycle. Because the duration of an MCC varies, a normalized time scale was used by dividing each case into seven roughly equal subperiods, representing:

1. Pre-MCC environment,
2. MCC initiation ("start"),
3. Growth phase,
4. Maximum size ("max"),
5. Mature, decaying phase,
6. MCC dissipation ("end"),
7. Post-MCC environment.

Although the actual duration of each stage varied for each case, the subperiods averaged about 2.8 hours in length. Depending on the starting time and duration of an MCC, its 12-hour upper air observations would fall into one, sometimes two, of these seven subperiods. Data composited for one subperiod were from different systems than those at an adjacent subperiod; thus, if MCCs have common evolutionary characteristics, data from each subperiod should compose a reasonably independent data set. Such an approach should reveal the MCC life cycle in more detail.

III. Precipitation Analysis

Seven years of digital hourly precipitation were available for analysis. Thirty-two cases were analyzed. For each system, hourly rainfall rates, areas, and volumes were computed over the MCC region, following the method described by McAnelly and Cotton (1985a), which had been slightly modified in order to automate the analysis.

These hourly values were then fitted into the appropriate subperiod. Because of the high temporal resolution of the data, each subperiod was further divided into two approximately 1.4 hour periods, a and b.

Figure 1 illustrates the systematic variation of precipitation rate, volume, and area for the composited set of 32 MCCs. Rain rates are greatest early in the MCC during the second and third subperiods. Volumetric rates peak around subperiod 4 when the MCC cloud shield is at a maximum. Later, the MCC is characterized by a large area of lighter, more stratiform precipitation. Such observations were also noted in a study of an episode of twelve MCCs in August 1977 (McAnelly and Cotton, 1985b).

Figure 2 depicts the average precipitation accumulation for the composite MCC from subperiod 2a through 6a. Greatest accumulations coincide with the location of the MCC during its growth stage, when rain rates are greatest.

Figure 3 presents the evolution of the distribution of the hourly precipitation rate, based on rain gauges with 0.1 in. (2.5 mm)/hour increments. Figure 4 is the same as Fig. 3, but based on gauges with 0.01 in. (0.25 mm) recording increments. Both figures show the evolution of precipitation from meso-β scale (20-200 km, <6 h) elements in subperiod 2 to more centrally organized, vigorous activity during subperiod 3, to a lighter, widespread regime from subperiod 4 on.

IV. Upper Air Analysis

As described in Section II, upper air synoptic observations for a large number of MCC cases were grouped according to their position in the life cycle of the MCC, resulting in 7 subperiods of relatively independent observations. From these data, kinematic and thermodynamic fields were objectively analyzed at 100 mb pressure levels using the data analysis/assimilation package of CSU's Regional Atmospheric Modelling System (RAMS)(Cotton et al., 1984). Figure 5 shows the trends of vorticity and divergence in the vicinity of the composite MCC at 200, 500 and 800 mb. Convergence increases coherently to a maximum in the low to middle troposphere, appearing first in the low troposphere (stage 3 at 800 mb) and progressing upward with time through the middle troposphere (stage 5 at 500 mb). Strong upper level outflow, indicated by divergence at 200 mb, is most intense at stage 4, when the MCC is at its maximum size.

Vorticity trends evolve similarly. At 800 mb positive vorticity gradually increases until the system reaches the decaying stage. Negative vorticity prevails at 500 mb until the system passes the mature stage when it becomes positive for a short time. At 200 mb negative vorticity becomes stronger until the mature decaying stage after which it appears to gradually weaken. At all three levels, the peak in positive or negative vorticity occurs about one subperiod later than its corresponding peak in negative or positive divergence. This lag probably represents the time required for the mesoscale inflow and outflow (which develops in response to storm-induced pressure perturbations) to become deflected by the Coriolis force.

Note that for each case the upper air observations were composited in a moving reference frame with the MCC at its center. In Figs. 6-11 the composite MCC lies in the center of the domain and the accompanying state outlines indicate its average position at the respective stages.

Figures 6a-g show the evolution of vorticity at 200 mb. While negative vorticity prevails in the vicinity of the MCC at all times, a strong gradient, initially to the northwest tightens and surrounds the MCC by subperiod 4. By the post-MCC stage, this vorticity gradient has slackened, but is still fairly strong to the northeast.

Figures 7a-c show the 200 mb divergence at the start, middle, and end of the composite storm. Initially the MCC is in a center of moderate divergence surrounded by a tight gradient. With time, this gradient weakens and divergence predominates over a much larger area.

At 500 mb (Figures 8a-c) high vorticity, initially to the northwest, seems to intrude into the MCC region, with a strong east-west gradient in the region at the dissipation stage.

Initially, the divergence at 500 mb (Figures 9a-c) is near neutral. A convergence center prevails near the MCC during subperiod 4. By the dissipation stage several convergence centers, bounded by tight gradients to the south and northwest, dominate the region.

At 800 mb positive vorticity is advected from centers in the west* during subperiod 2 (Fig. 10a) to just west of the MCC. Vorticity in the region of the MCC reaches its maximum values by subperiod 4, and weakens slightly by subperiod 6 (Figs. 10b and c).

Initially divergence at 800 mb in the MCC region is near neutral (Fig. 11a), but several convergence and divergence maxima are to the west. By subperiod 4, a convergence center dominates the MCC region (Fig. 11b) and persists but weakens through the dissipation stage (Fig. 11c).

As with the precipitation compositing study (Section III), results from the upper air compositing study can be compared to the satellite defined MCC life cycle. This compositing approach reveals an upward

---

*While it is tempting to conclude these vorticity centers are orographic, this is not necessarily so because the moving reference frame centered on the MCC does not always place the western domain in the mountains.

progression of convergence and vorticity maxima with time from low to middle tropospheric levels, as well as the development of the strong upper-tropospheric divergent anticyclone. These trends suggest that the MCC transforms upscale, from a convectively-forced system driven by buoyant energy released from the boundary layer, into a meso-α-scale system (characterized by a weak vortex) driven by a deep layer of low- to midlevel convergence, which sustains the large, lightly precipitating anvil.

V. Conclusion

This compositing approach has yielded a more detailed description of the physical characteristics of Mesoscale Convective Complexes. In general, the conclusions of Maddox (1981, 1983); McAnelly and Cotton (1985a, 1985b); and others have been confirmed.

These results, however, are somewhat preliminary. Because this research is also funded by another ongoing project, these studies will be completed and should be published in a refereed journal.

References

Cotton, William R., Edward E. Hindman, Gregory Tripoli, Ray L. McAnelly, C. Chen, C. Tremback, P. Flatau, and K. Knupp, 1984: Model Cloud Relationships. Final Report, 26 November, 1981 - 30 September, 1983. Project No. F1 9628-82-K-0003. Air Force Geophysics Laboratory, Air Force Systems Command, United States Air Force, Hanscomb AFB, Massachusetts. (AFGL-TR-84-0028).

Maddox, Robert A., 1981: The structure and life cycle of midlatitude mesoscale convective complexes. Atmospheric Science Paper No. 336, Dept. of Atmos. Sci., Colorado State University, Ft. Collins, CO. 311 p.

Maddox, Robert A., 1983: Large-scale meteorological conditions associated with midlatitude, mesoscale convective complexes. Mon. Wea. Rev., 111, 1475-1493.

McAnelly, Ray L. and William R. Cotton, 1985a: Meso-β-scale characteristics of the meso-α-scale convective complex. To appear in Mon. Wea. Rev.

McAnelly, Ray L. and William R. Cotton, 1985b: The precipitation life cycle of mesoscale convective complexes. Preprints, Sixth Conference on Hydrometeorology, Amer. Meteorol. Soc., 28-31 Octover, 1985, Indianapolis, Indiana. 8 p.

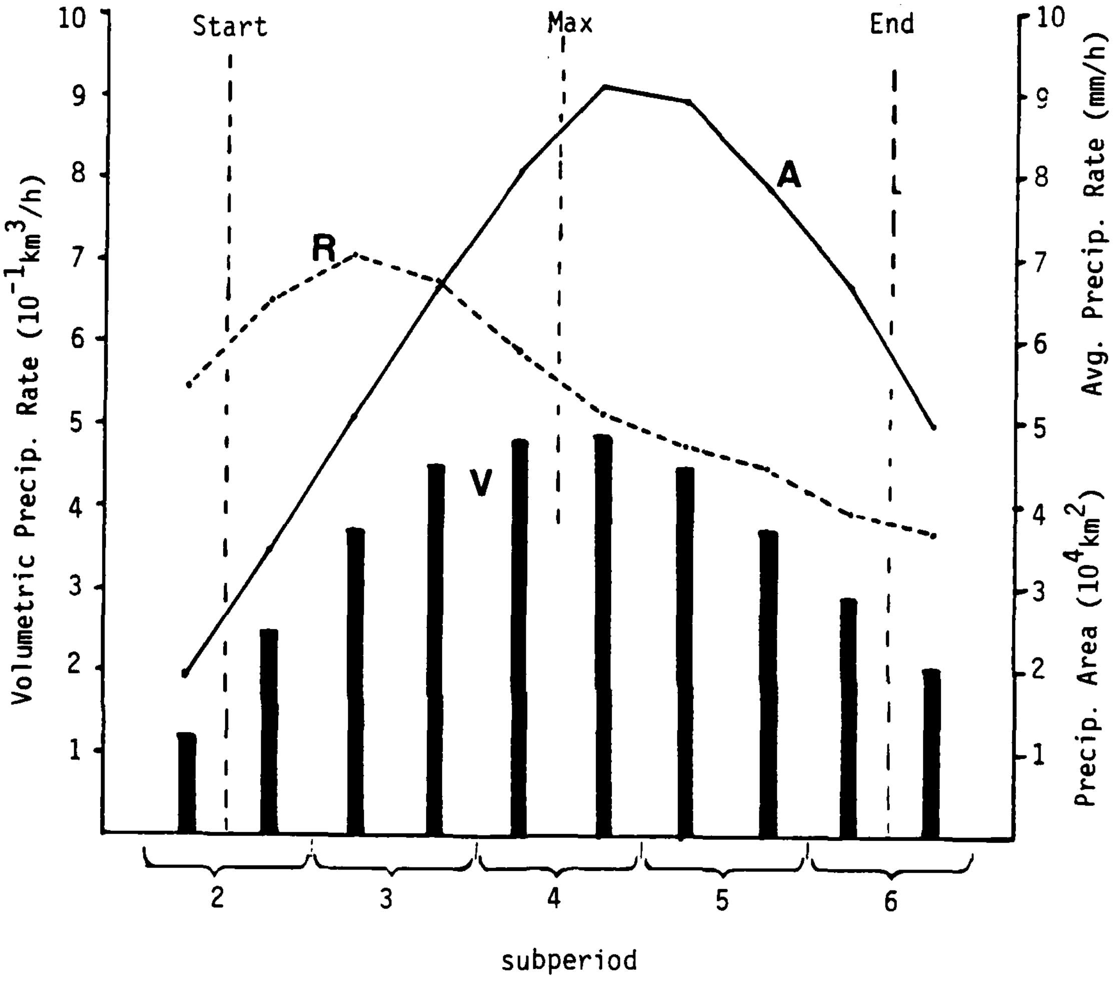

Figure 1. Composite analysis of the temporal trend of the bulk precipitation characteristics of MCCs.

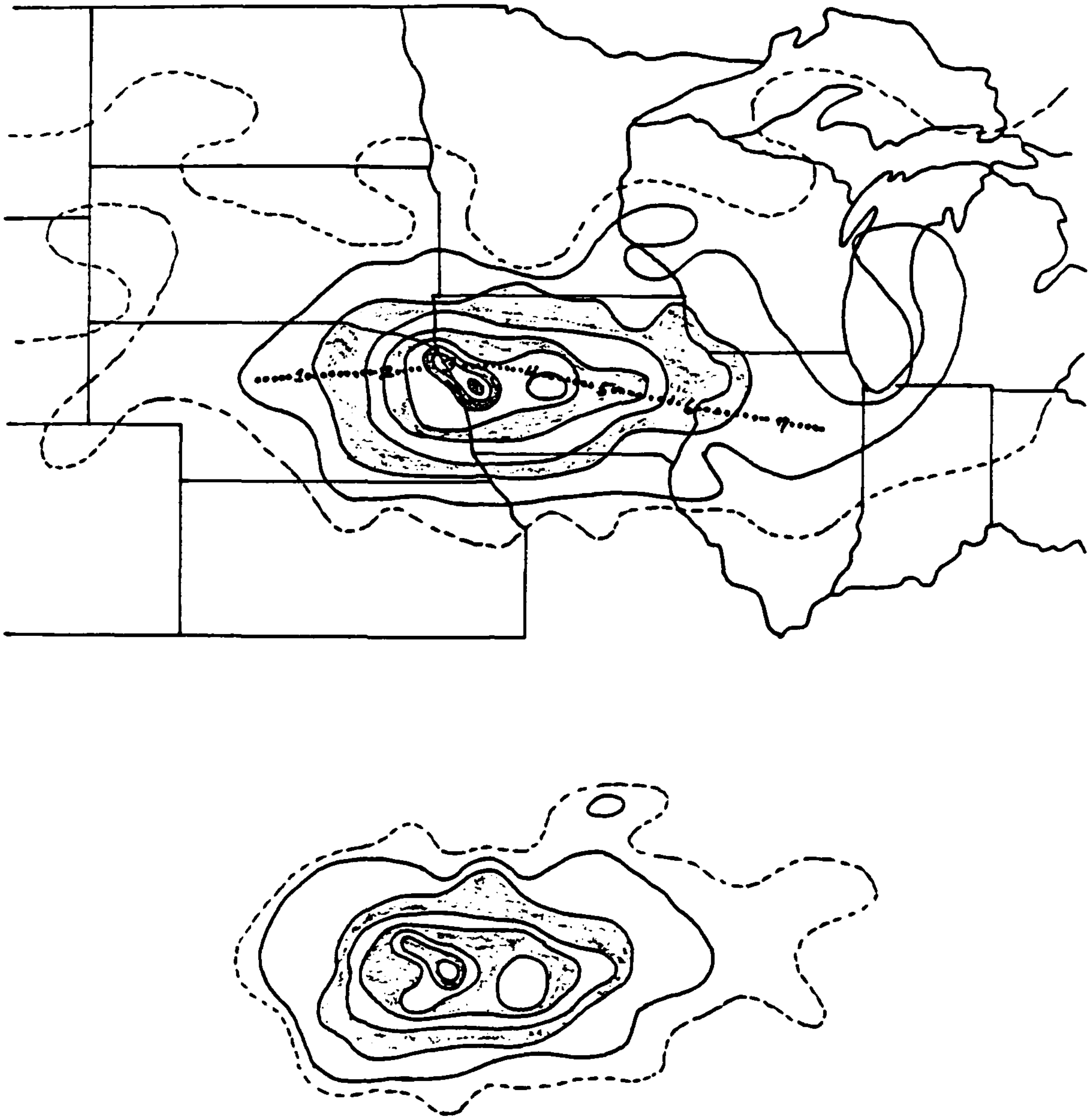

Figure 2. Distribution of average precipitation accumulation for the composite MCC, positioned with respect to the mean position of its "maximum" stage. Top: All precipitation. Dotted line shows mean track and positions at subperiods 1 through 7. Bottom: MCC associated precipitation only. Outer dashed contour is 2.5 mm. Solid contours are in 5 mm increments from 5 to 40 mm.

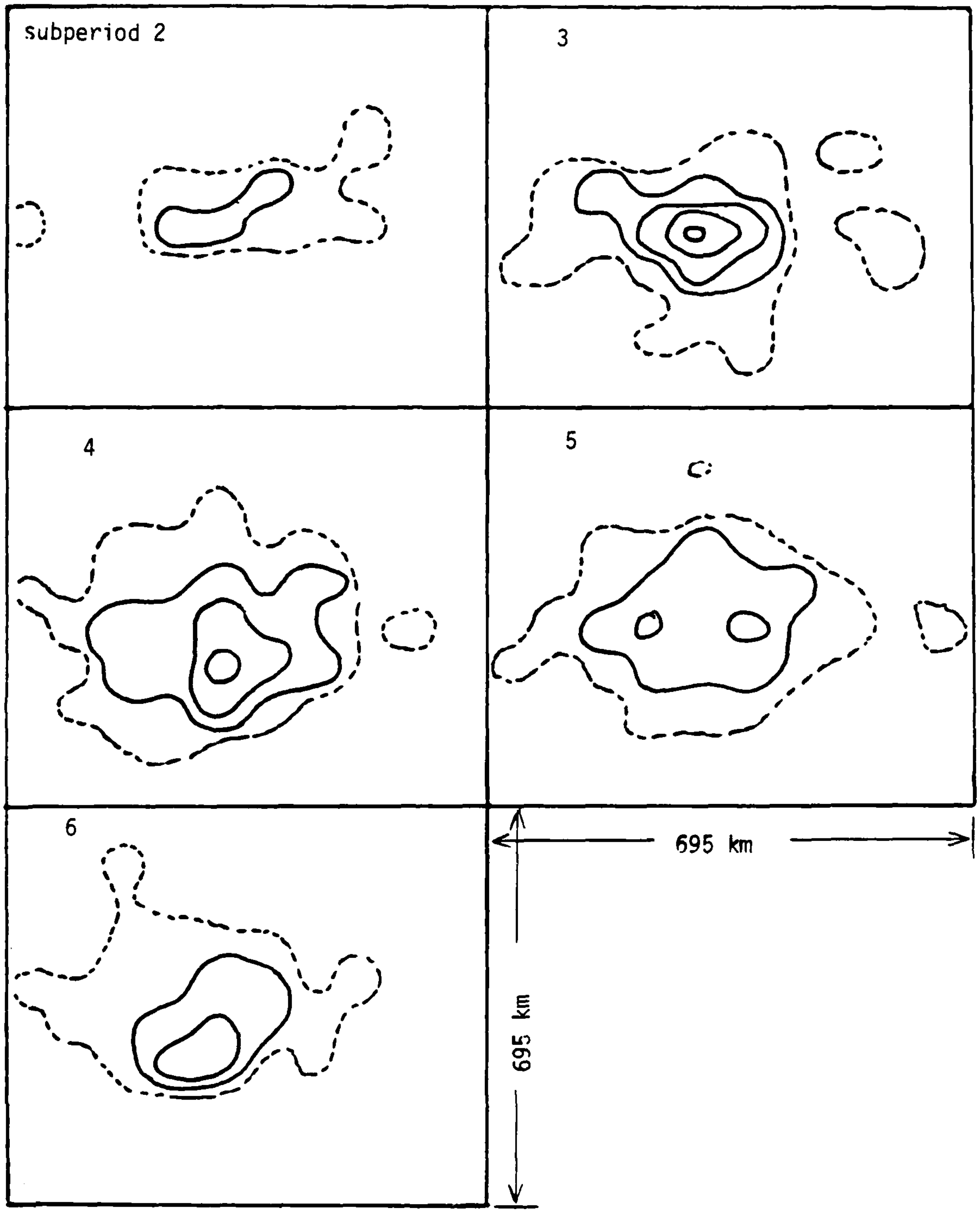

Figure 3. Evolution of the distribution of the composite MCCs precipitation rate. Outer dashed contour is 1.0 mm/h. Solid contours are in 2.5 mm/h increments, beginning at 2.5 mm/h. Based on rain gauges with 2.5 mm/h recording increments.

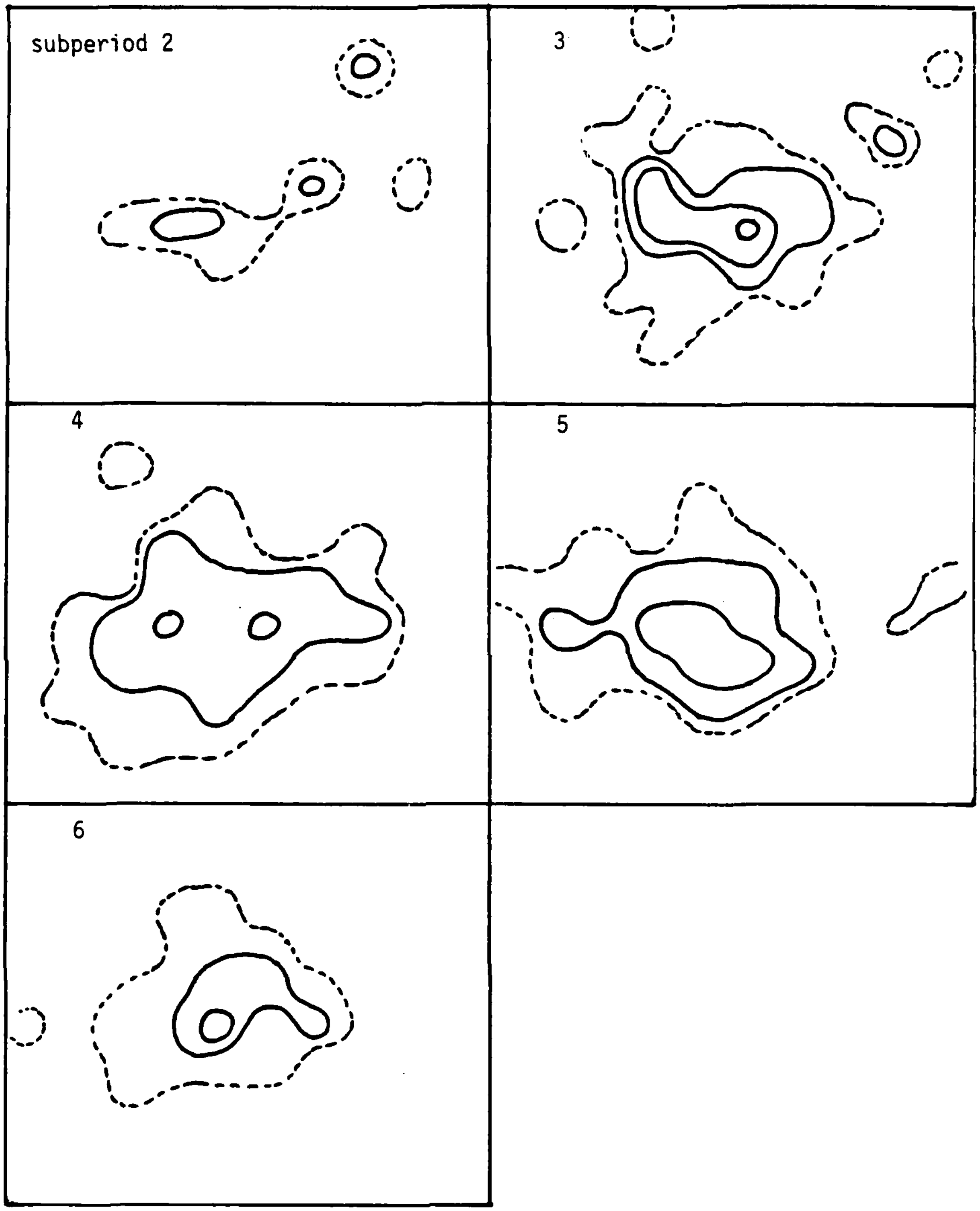

Figure 4. Same as Figure 3, except based on gauges with 0.25 mm/h recording increments.

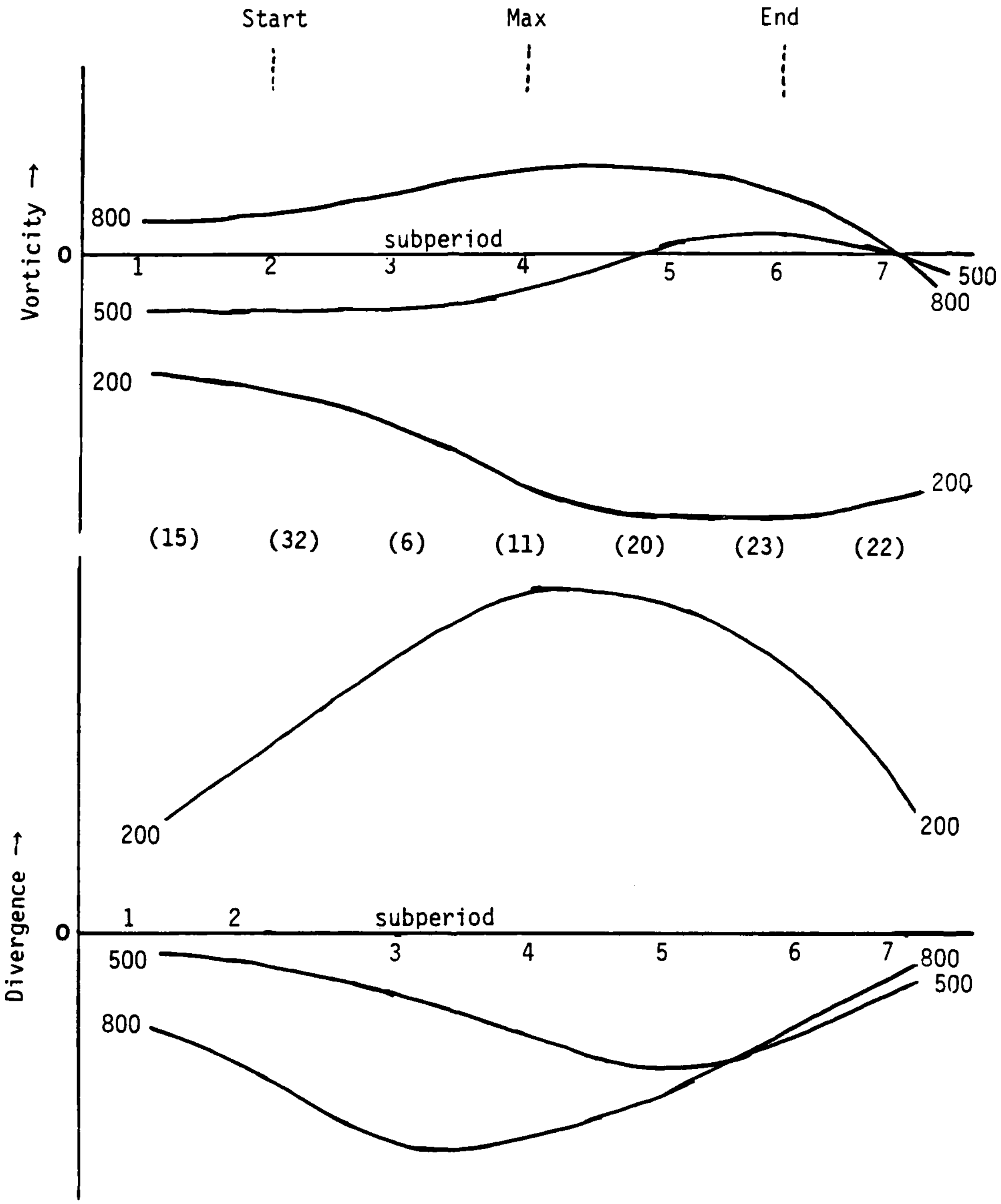

Figure 5. Trends of vorticity and divergence at 200, 500, and 800 mb in the vicinity of the MCC, based on composite objective analysis. The numbers in parentheses between the two graphs are the case sample sizes for each subperiod.

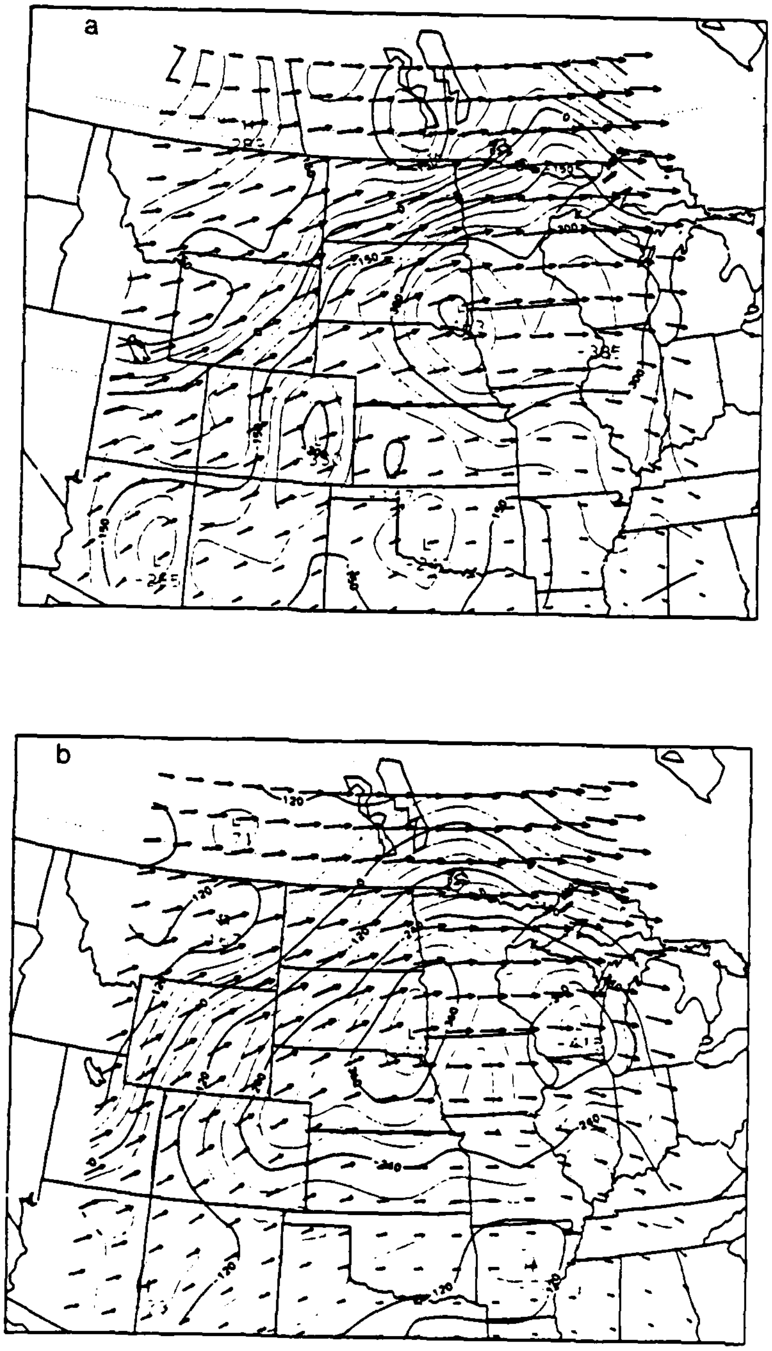

Figure 6. Composite 200 mb vorticity field for a) subperiod 1 (pre-MCC environment), b) subperiod 2 (MCC initiation), c) subperiod 3 (growth phase), d) subperiod 4 (maximum size), e) subperiod 5 (mature decaying phase), f) subperiod 6 (MCC dissipation, and g) subperiod 7 (post-MCC environment).

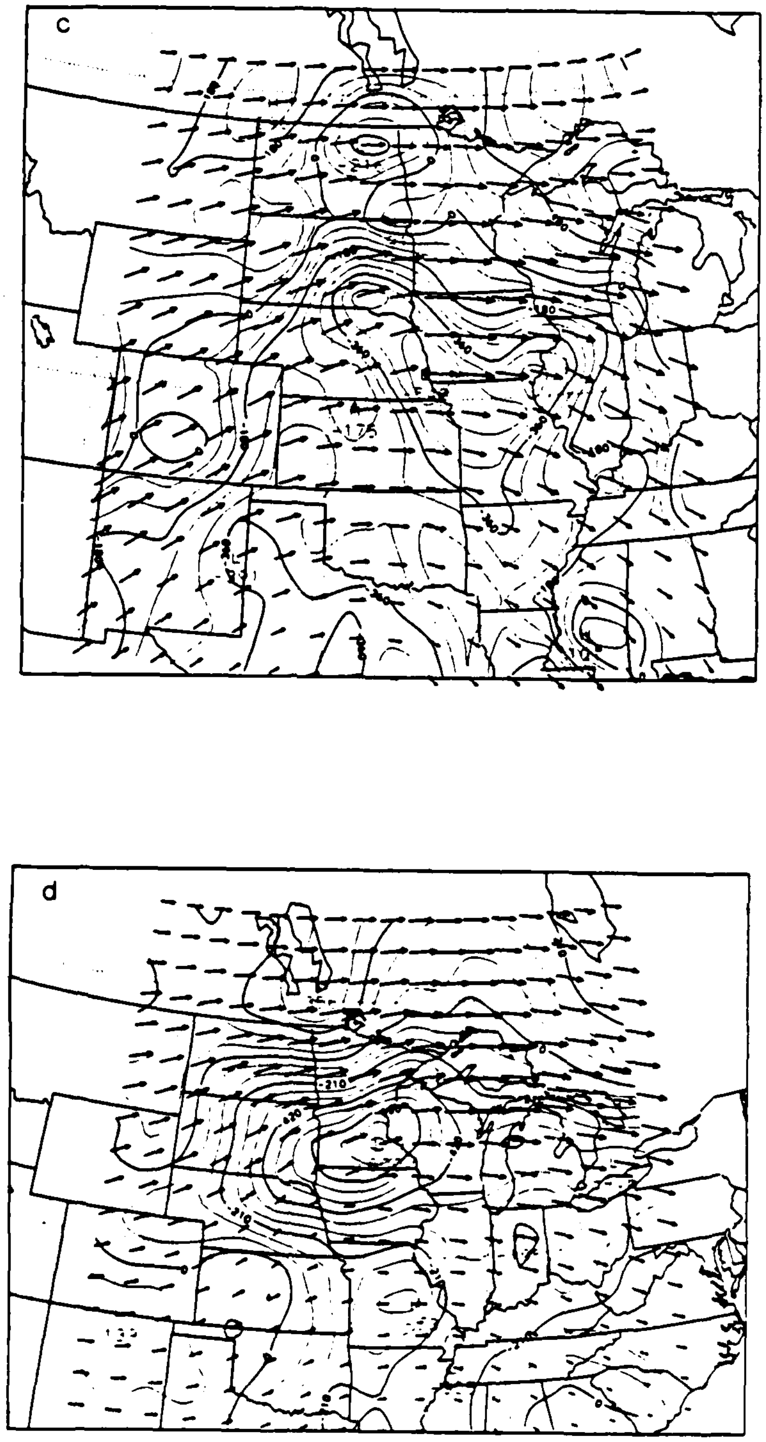

Figure 6. (continued)

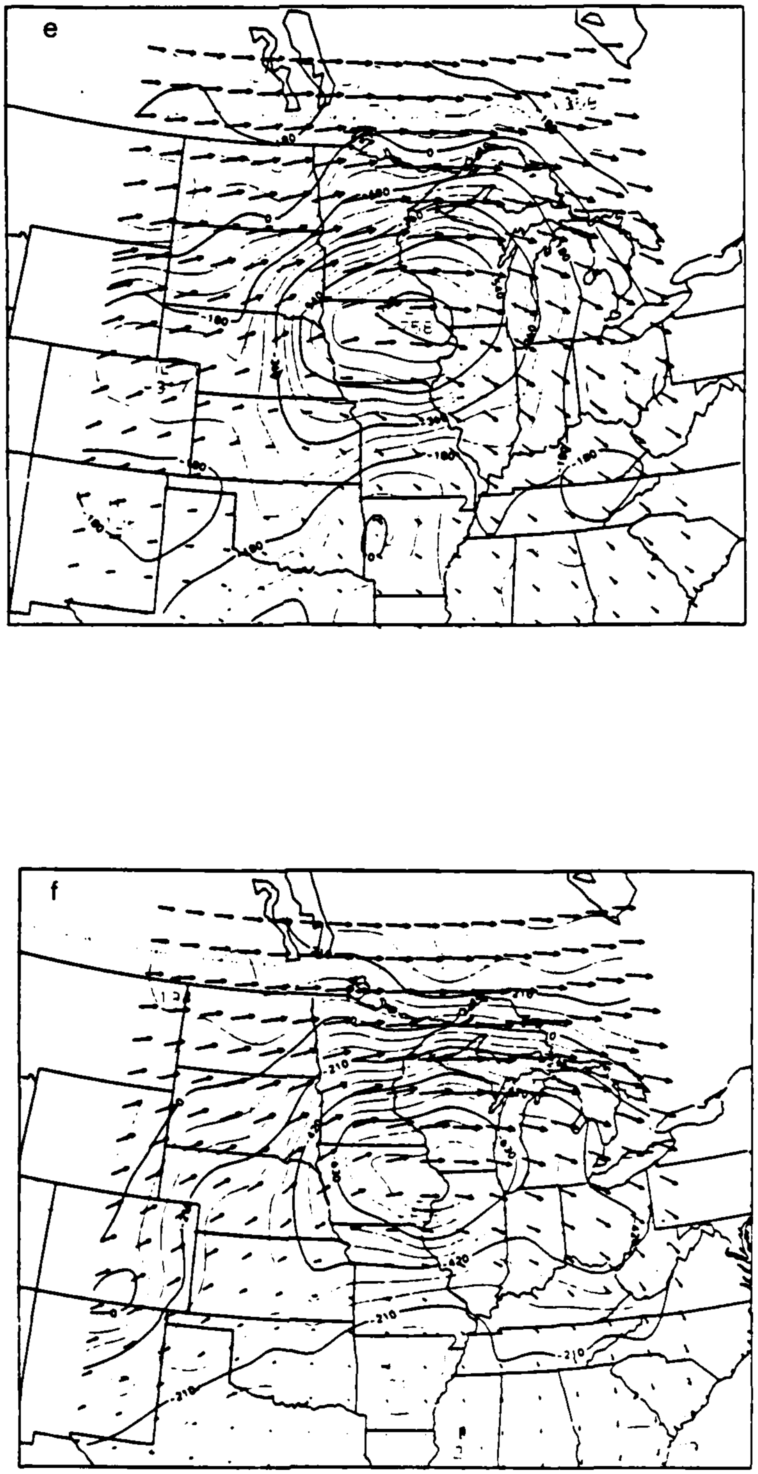

Figure 6. (continued)

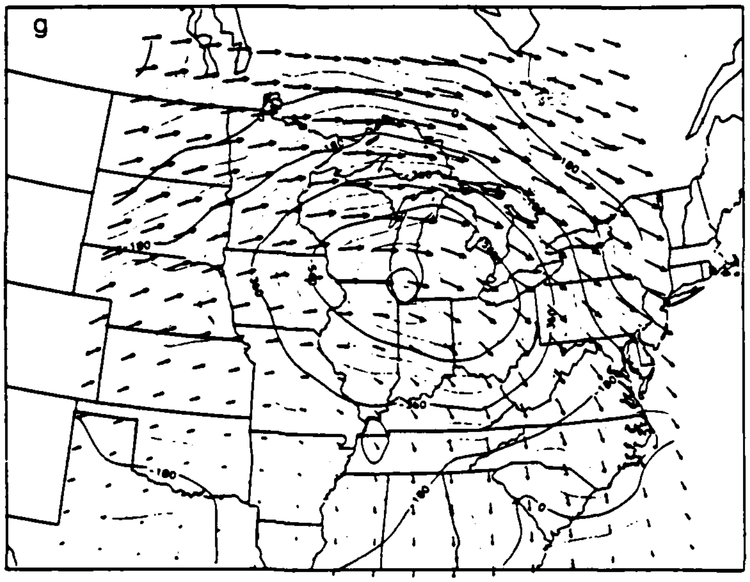

Figure 6. (continued)

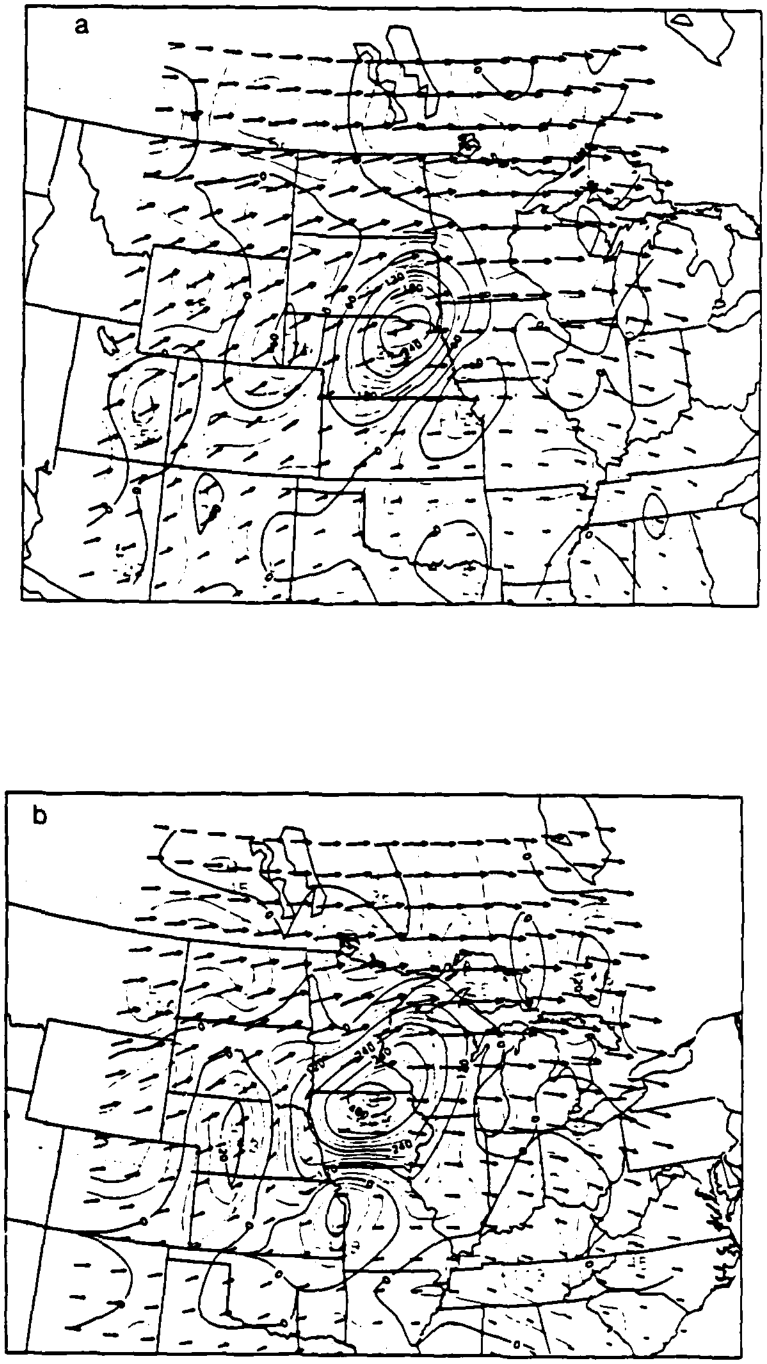

Figure 7. Composite 200 mb divergence field for a) subperiod 2 (MCC initiation), b) subperiod 4 (maximum size), and c) subperiod 6 (MCC dissipation).

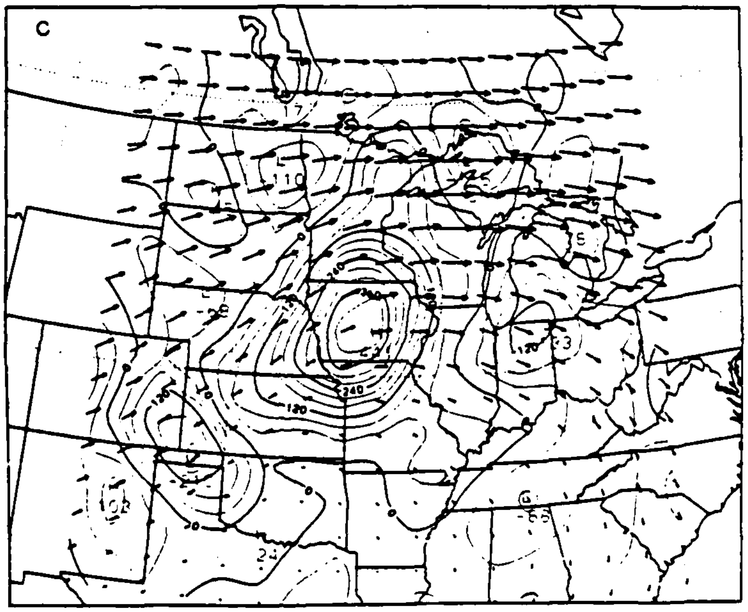

Figure 7. (continued)

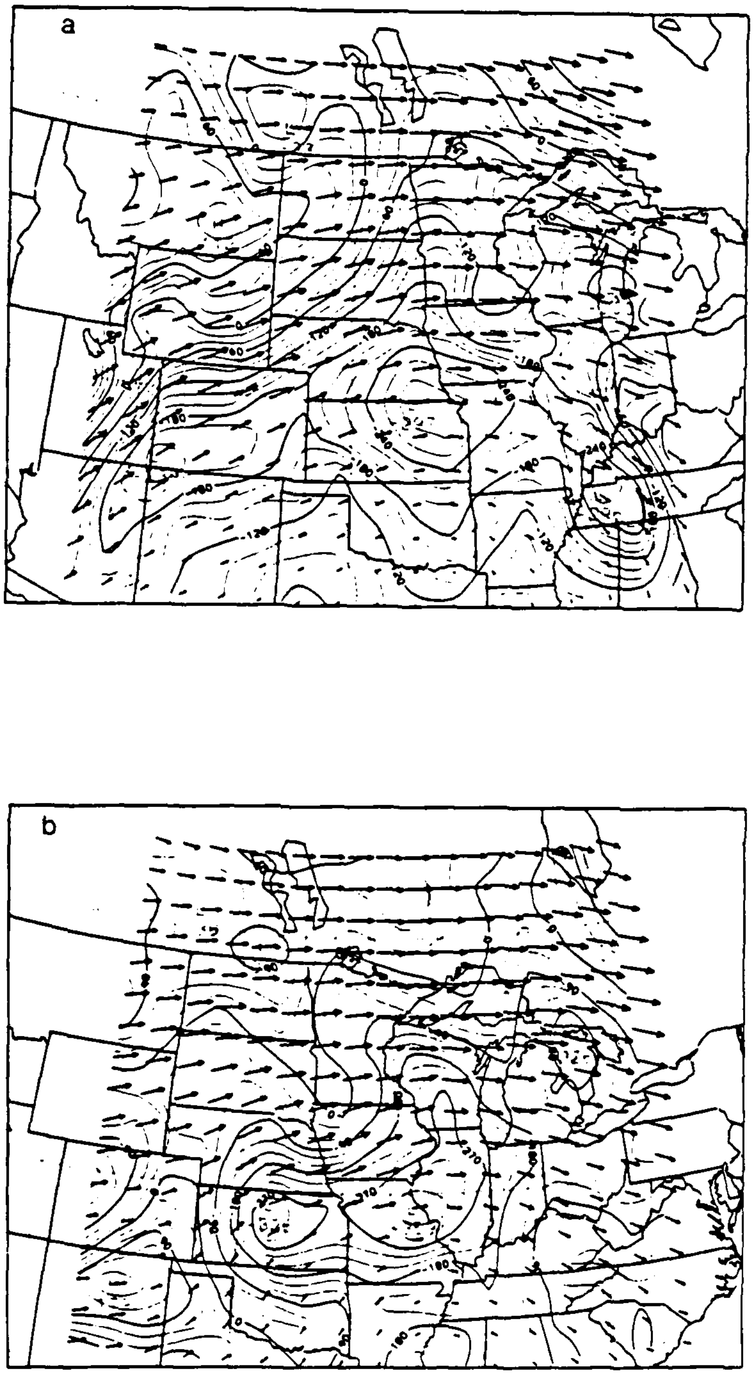

Figure 8. Compsite 500 mb vorticity field for a) subperiod 2 (MCC initiation), b) subperiod 4 (maximum size), and c) subperiod 6 (MCC dissipation).

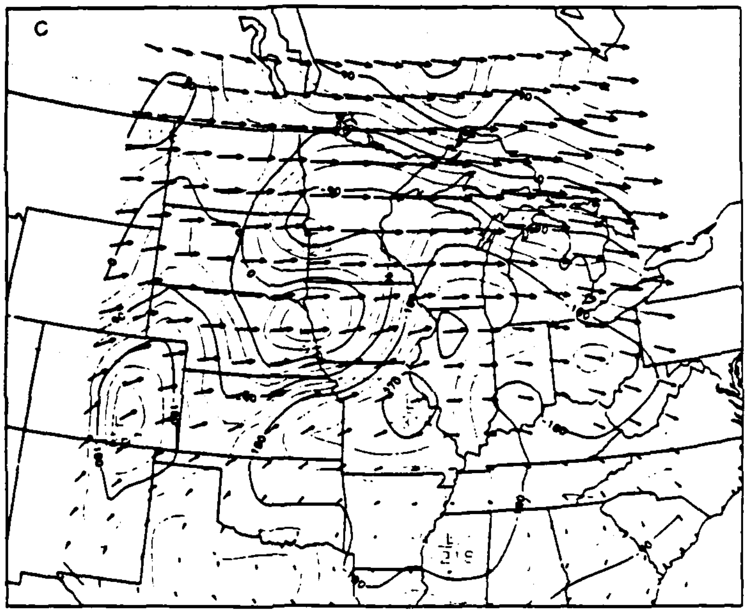

Figure 8. (continued)

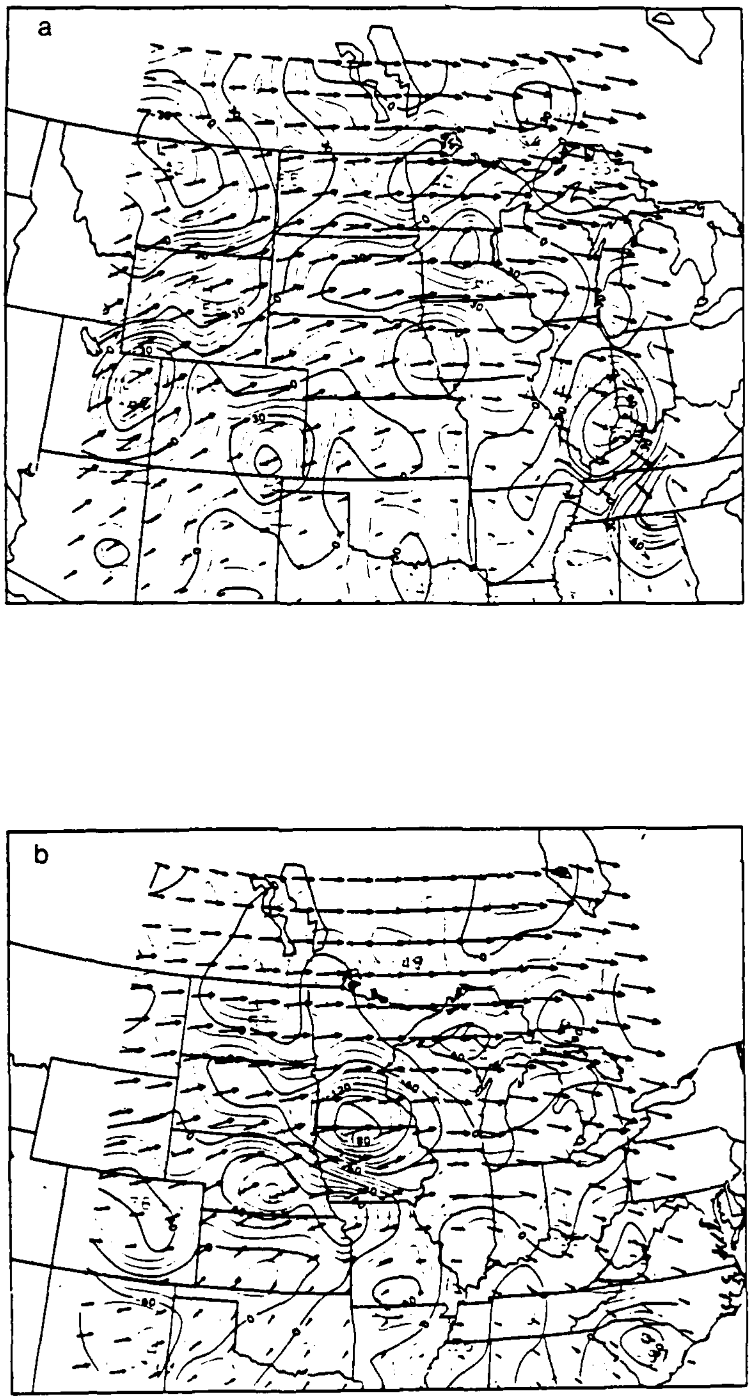

Figure 9. Composite 500 mb divergence field for a) subperiod 2 (MCC initiation), b) subperiod 4 (maximum size), and c) subperiod 6 (MCC dissipation).

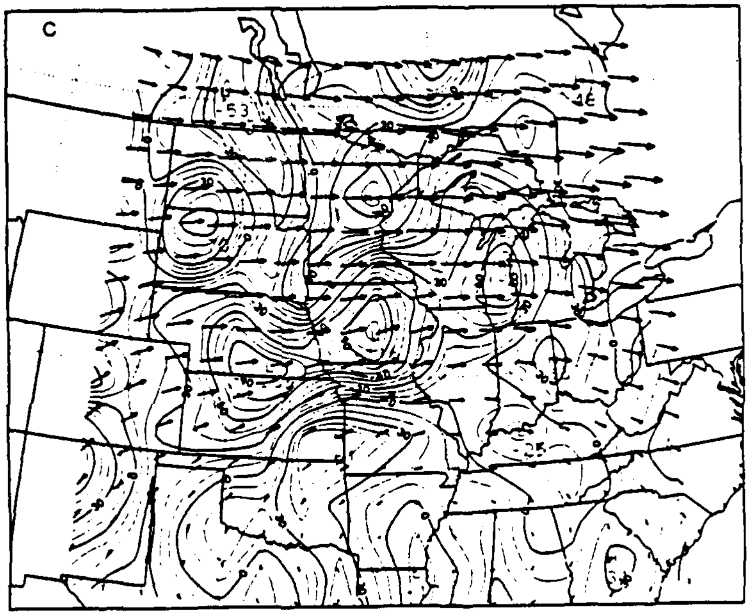

Figure 9. (continued)

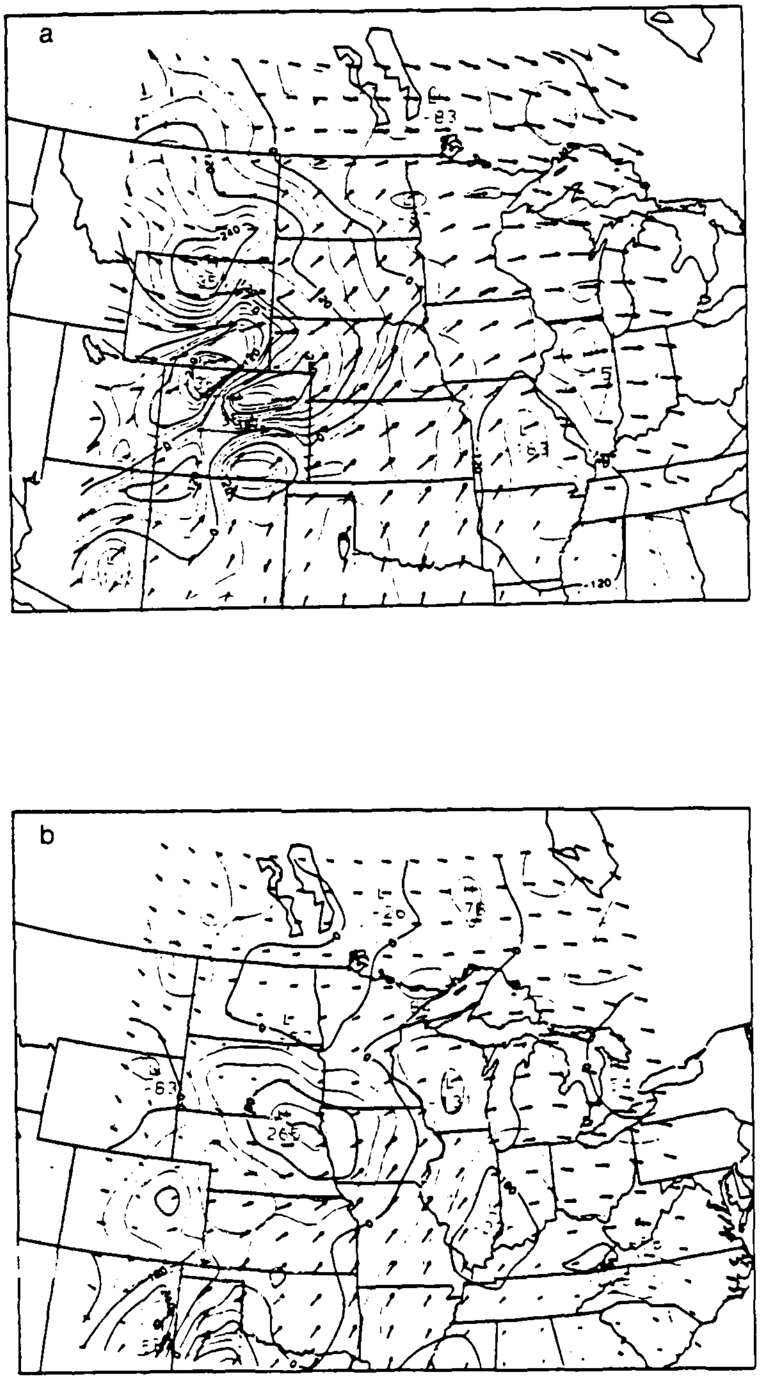

Figure 10. Composite 800 mb vorticity field for a) subperiod 2 (MCC initiation), b) subperiod 4 (maximum size), and c) subperiod 6 (MCC dissipation).

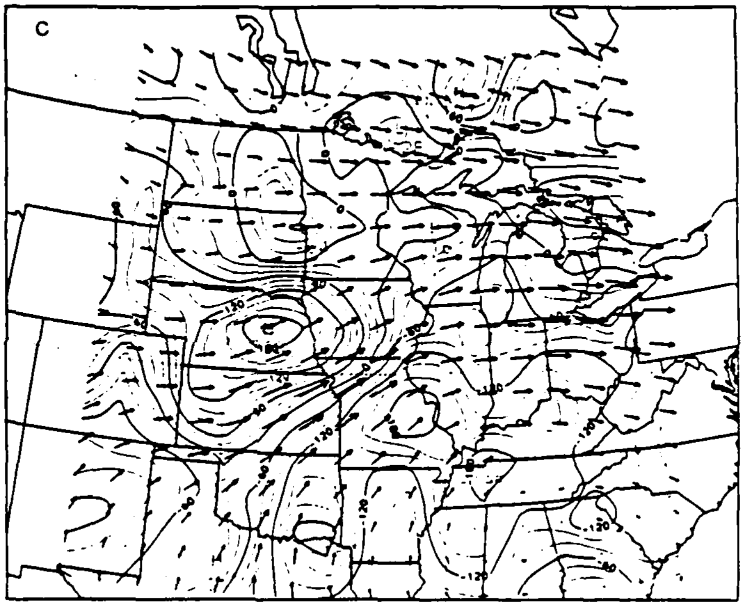

Figure 10. (continued)

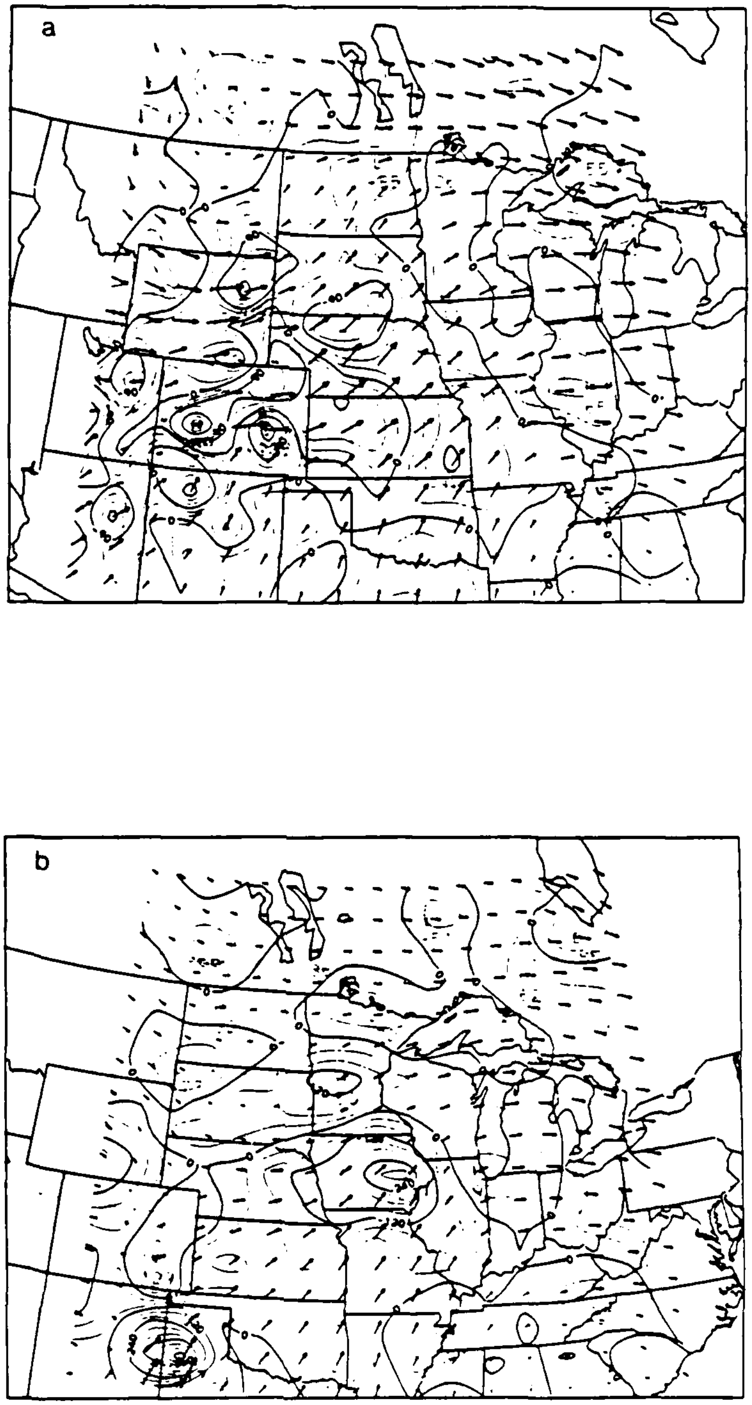

Figure 11. Composite 800 mb divergence field for a) subperiod 2 (MCC initiation), b) subperiod 4 (maximum size) and c) subperiod 6 (MCC dissipation).

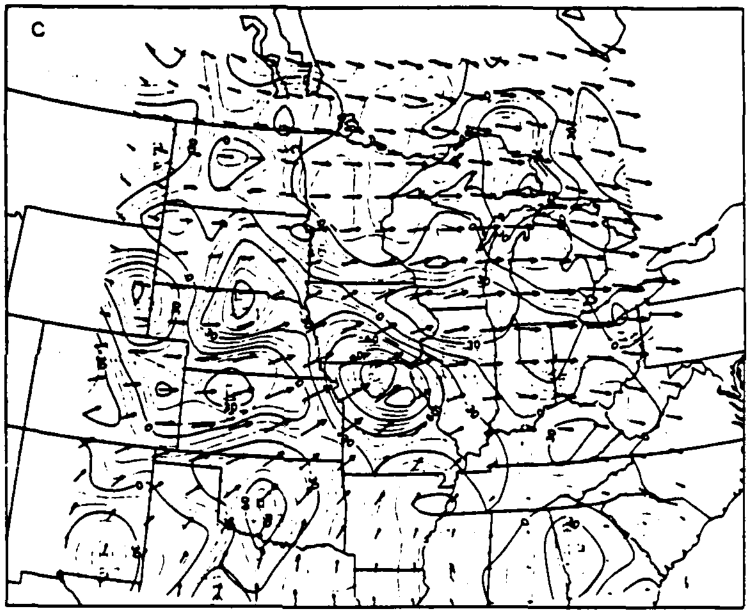

Figure 11. (continued)

APPENDIX D

THE PRECIPITATION LIFE CYCLE OF MESOSCALE CONVECTIVE COMPLEXES

by

Ray L. McAnelly and William R. Cotton

To appear in Pre-prints, Sixth
Conf. on Hydrometeorology, Amer.
Meteor. Soc., 28-31 October 1985,
Indianapolis, Indiana.

THE PRECIPITATION LIFE CYCLE OF MESOSCALE CONVECTIVE COMPLEXES

Ray L. McAnelly and William R. Cotton

Dept. of Atmospheric Science
Colorado State University
Fort Collins, CO 80523

1. INTRODUCTION

The mesoscale convective complex (MCC), defined by Maddox (1980), is a common and particularly well-organized class of meso-α-scale (200-2000 km, > 6h) storm systems over the central United States. A typical MCC has a ~12 h life-cycle, and produces ~1-10 x 10^{12} kg of rainfall over an area of ~1-10 x 10^5 km^2, at an average depth of 10-20 mm. Thus, the impact of MCCs on the convective season climatology of this region is very significant in terms of widespread beneficial rainfall (Fritsch et al., 1981), and also in terms of severe weather and local flooding (e.g., Maddox, 1981; Rodgers et al., 1985). However, the complex web of scale interactions that are involved in their formation and evolution is poorly understood, and they remain an elusive forecast problem (e.g., Fritsch and Maddox, 1981).

This paper presents the temporal nature of the MCC's precipitation characteristics, as generalized from an analysis of a limited number of systems. The results suggest that the MCC is characterized by a well-defind precipitation life-cycle signature relative to its satellite appearance. Significant lead-lag relationships in this life-cycle offer potential methods for improved short-range forecasts of these systems. A much larger sample of systems is being analyzed in order to test the generality of this life-cycle model.

2. DATA AND ANALYSIS METHODOLOGY

The MCCs selected for analysis occurred on successive evenings of an 8-day episode during August 1977 over the central United States. Fig. 1 shows the paths of the systems, which generally tracked eastward along a quasi-stationary frontal zone. Also evident are two distinct genesis regions, one along the High Plains to the lee of the Rockies, and another further east over the lower, flatter terrain of Iowa and Missouri. MCCs originating in these two regions are termed "western" and "eastern" systems, respectively. The 8-day total rainfall distribution in Fig. 2 clearly shows how the MCCs dominated the episode precipitation over the Central Plains and Midwest. A more complete account of the episode is given by Wetzel et al. (1983).

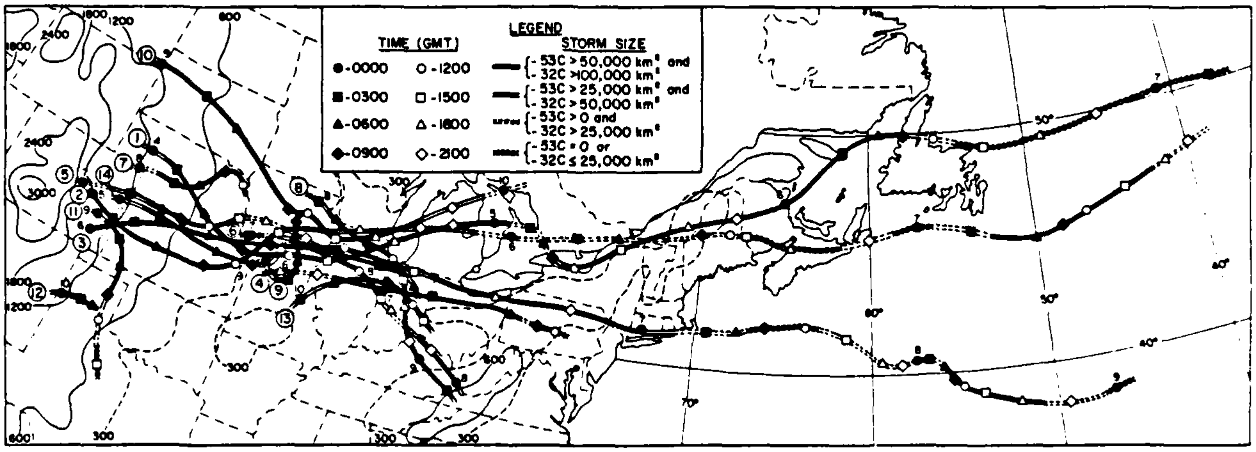

Fig. 1. Tracks of the centroids of the 14 mesoscale convective systems which attained MCC dimensions (darkened track) during the episode of 3-10 August 1977, based on 3-h interval analysis of geosynchronous, infrared satellite data. Circled system numbers indicate the chronological order of their initial appearances. The date is given near each 0000 GMT symbol. Smoothed terrain heights are indicated by solid contours at 600-m intervals and the dashed 300-m contour. [Adapted from Wetzel et al. (1983)].

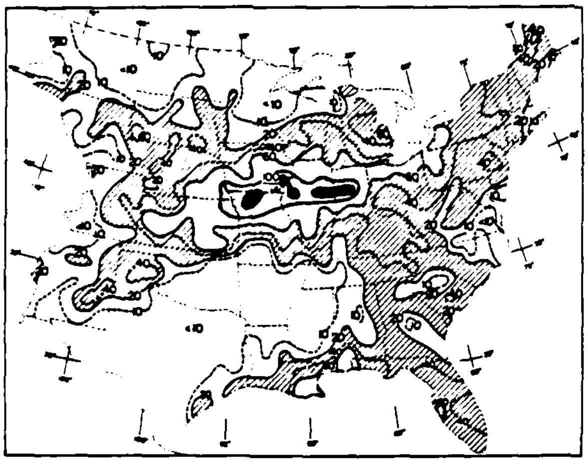

Fig. 2. Episode precipitation distribution for the United States east of the Continental Divide, with isohyets labeled in millimeters. Analysis is based on averaged station totals in each 1° latitude/longitude block, where all available stations reporting 24 h amounts (in Climatological Data, from the National Climatic Data Center) were used. Number of stations per block ranged from 5-25, with 10-15 being most common. End of all eight-day accumulations were on 11 August 1977 locally, most commonly from 0600-0800 local time.

In a study of the evolving sub-structure of several of the episode's MCCs, McAnelly and Cotton (1985) found that there was extreme structural variability from case to case, with most systems being dominated by multiple meso-β-scale (20-200 km, < 6h) convective clusters. Despite this sub-structural variability, however, the infra-red (IR) satellite evolution of most MCCs progresses through a consistent, well-defined sequence of events, as illustrated by the first MCC of the episode shown in Fig. 3. Evident in this system is the presence of multiple discrete meso-β thunderstorm clusters in the developing stages (Fig. 3a,b); the growth and merger of these clusters into a unified meso-α anvil system (Fig. 3b-d); the persistence of deep overshooting convection (interior white regions) within the organized meso-α-scale "cell" (Fig. 3d,e); and the eventual northeast/southwest elongation of the cloud system as its convective intensity weakens (Fig. 3f,g).

These characteristic IR features can be used to define several points within the MCC life-cycle. The MCC is defined to "start" when the contiguous area within the -53°C IR isotherm (dark-gray step) first exceeds 50,000 km^2, to reach its "maximum" when this area attains its largest size, and to "end" when this area first becomes less than 50,000 km^2 (02, 10 and 16 GMT, respectively, in Fig. 3). The mature duration of the MCC is defined as the time from "start" to "end". The meso-α "cellular" stage is defined more subjectively as the period after the system has unified and during which the -53°C IR contour is relatively smooth and circular (contrast the smooth "cellular" appearance at 07 and 09 GMT with the more jagged -53° appendages before, and more ragged -53°C edges afterward, in Fig. 3). Within the "cellular" stage, the time of maximum "overshooting" convective activity is defined subjectively as when the light-shaded anvil interior reaches its largest and coldest extent (07 GMT in Fig. 3).

Such IR-defined life-cycles were derived for twelve of the episode's MCCs listed in Table 1, and quantitative precipitation histories (based on "Hourly Precipitation Data", published by the National Climatic Data Center) were derived for each system relative to its IR life-cycle. Because of the hourly precipitation network's non-uniformity in station spacing, sparsity especially in the western plains, and inability to representatively sample convective-scale rainfall, a composite analysis approach was adopted in which the hourly precipitation information of the twelve MCCs was combined into composite categories.

As shown in Table 1, the MCCs were stratified according to genesis region and maximum anvil size into four composite groups of three similar systems each: western large (W-L), eastern large (E-L), western small (W-S) and eastern small (E-S) MCCs. The W-L and E-L MCCs had maximum anvil areas about 2.5 times larger, and had durations longer (by less than a factor of 2), then their smaller counterparts. In terms of total volumetric rainfall (from 2h prior to "start" to 1h after "end"), the W-L and E-L average systems produced 13.6 and 4.6 times more, respectively, than the average W-S and E-S systems (Table 1).

Since this difference in rainfall production can only be partly accounted for by the larger systems' greater anvil size and longer duration, there is evidence that large MCCs are more efficient precipitators than smaller systems. This is particularly evident for the western cases, where one would expect significant sub-cloud evaporation in this semi-arid region. A probable contributor to the larger systems' greater efficiency is that the area-to-circumference ratio of their precipitation producing cloud area is larger: a large ratio implies a correspondingly large ratio of protected "core" precipitation to "peripheral" precipitation, the latter being more susceptible to evaporation in the subsaturated air. Because the large systems are so much more significant rain producers, the remainder of this paper emphasizes the W-L and E-L MCC life-cycles.

The composite analysis approach is illustrated in Fig. 4, where the timing of the IR-defined life-cycle points is indicated along an hourly time axis for each MCC. In each composite category, the three individual MCCs are considered to have common composite times of "start" (MCC hour 0), "maximum" and "end". In addition to the similar characteristics listed in Table 1 for the MCCs in each category, Fig. 4 shows that they were also very similar in terms of other characteristics, including: the "start-to-maximum" and "maximum-to-end" durations; the timing of the "cellular" stage and the "overshooting-top maximum" within the "start-maximum-end" sequence; the timing of quartiles of accumulated rain volume; and the absolute GMT times of the entire life-cycle. Thus, realistic time scales for the composite MCCs could be derived, with the resultant composite precipitation analysis accurately reflecting the nature of the individual large systems.

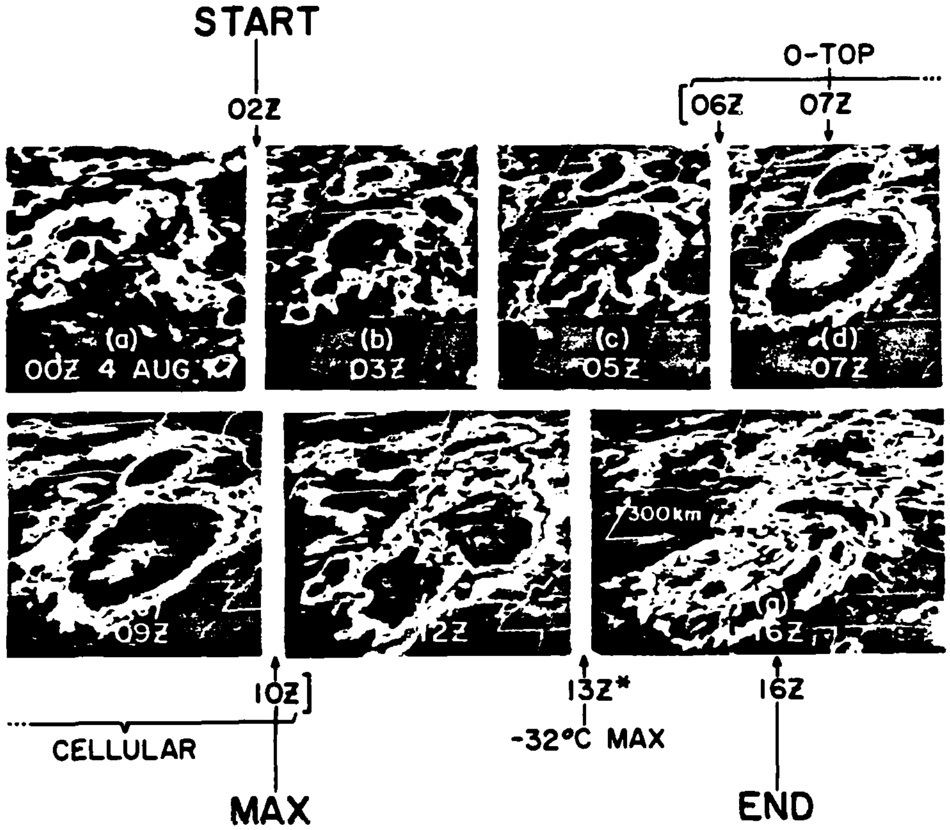

Fig. 3. Enhanced IR GOES-east satellite images spanning the life-cycle of the western MCC #1 through the night of 3-4 Aug 1977. Central Standard Time is 6 h earlier than the indicated GMT time. The stepped shades of medium gray, light gray, dark grey and black are thresholds for areas with apparent blackbody temperatures colder than -32, -42, -53 and -59°C, respectively. Temperatures progressively colder than -63°C appear as a gradual black-to-white shade. The grid in the 0900 GMT image is positioned about 150 km too far northward. A distance scale is indicated over Nebraska in (g). The life-cycle terminology is described in the text.

Table 1. Meso-α-scale statistics of the 12 MCCs studied quantitatively, stratified by genesis region and by maximum anvil size into four composite categories.

		LARGE MCCs					SMALL MCCs			
		Maximum IR Area ($10^3 km^2$)		Mature Duration (h)	Total Rainfall Volume ($10^{-3} km^3$)		Maximum IR Area ($10^3 km^2$)		Mature Duration (h)	Total Rainfall Volume ($10^{-3} km^3$)
		-53°C	-32°C				-53°C	-32°C		
WESTERN MCCs	#1	340	611	14	4867	#5a	101	218	9	109
	#2	252	383	16	6075	#11	86	155	7	289
	#3	238	386	13	6049	#12	138	208	8	855
	Western Large Average	277	460	14.3	5664	Western Small Average	108	194	8.0	418
EASTERN MCCs	#6	239	354	10	3540	#4	108	167	7	2516
	#8	307	562	13	8213	#5b	89	132	6	323
	#9/10	307	522	9	6964	#9	139	227	9	1221
	Eastern Large Average	284	479	10.7	6239	Eastern Small Average	112	175	7.3	1353

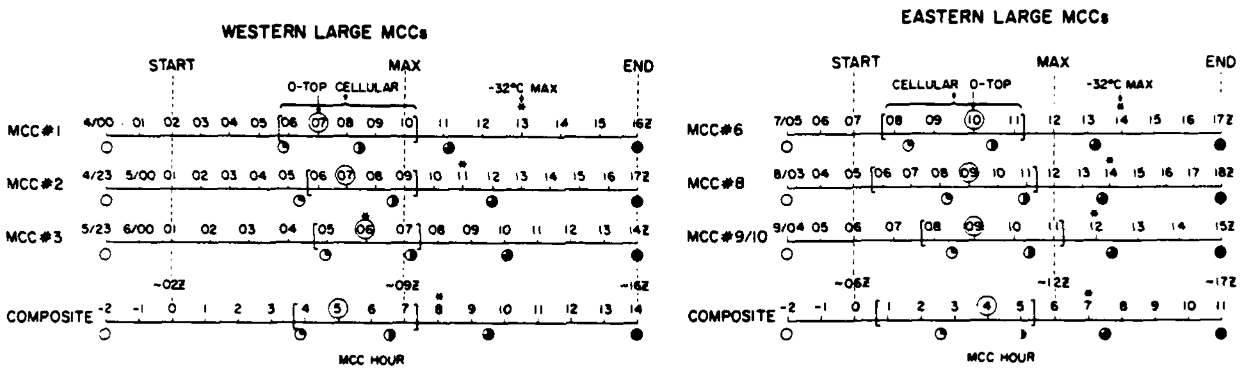

Fig. 4. Relation of the three Western-Large MCCs and the three Eastern-Large MCCs to their respective composit time scales. Each MCC is represented by a time scale labelled in GMT hours and is fitted to its composite time scale according to the IR-defined characteristics (defined in text) of "start", "maximum" and "end" (vertical dashed lines). Also indicated are the times of other IR-defined characteristics: a meso-α-scale "cellular" stage (in brackets); an "overshooting-top" maximum intensity (circled); and the maximum size of the -32°C IR area (asterisk). Based on a total accumulated hourly rainfall volume from 2 h prior to "start" to "end", the timing of the total's quartiles is indicated by the appropriately shaded circles under each MCC time scale. The composite MCC for each category, labelled with an hourly time scale "starting" at hour 0, is based on the average timing and durations of these IR and precipitation characteristics for the three individual MCCs. The timing of the composite IR features is rounded to the nearest whole MCC hour.

The composite analysis procedure consisted first of deriving hourly values of measurable rainfall area, average rain depth and rain volume for each individual MCC. These hourly values were smoothed with a 1-2-1 running filter and fitted or interpolated onto the appropriate composite hourly time scale. Finally, for each composite category, the three individual composite fits were arithmetically averaged hour-by-hour. Similar composite analyses were performed to derive quantitative histories of the IR areas, frequency distributions of hourly precipitation intensity, and frequency distributions of Manually Digitized Radar data (Moore, et al., 1974).

3. COMPOSITE LIFE-CYCLE

The growth/decay cycle of the IR cloud shield associated with the large composite MCCs is displayed in Fig. 5. For both composites, both -53 and -32°C areas expand monotonically to their maximum sizes, followed by monotonic decreases. The major difference between the two large composites is that the E-L system has a much larger expansion rate in its first several hours, and attains a meso-α "cellular" organization much sooner, than the slower developing W-L MCC. Comparing the large and small systems (not shown), both large composites have early growth rates exceeding those of their smaller counterparts. For example, over the organizational period from MCC hours -2 to 2, the growth rates of the -53°C area in the W-L and E-L systems are 159% and 195% of the W-S and E-S rates, respectively. This suggests a potential short-range forecasting technique whereby the maximim size and duration of an MCC and thus its total rainfall production, might be projected from its early growth trend.

For each composite, the expansion rates of the -32 and -53°C areas are fairly constant from "start-to-maximum", with the ratio of -53 to -32°C areas remaining relatively steady at about 0.6 to 0.8. After the "maximum", the -32°C area continues to expand for another hour, and the ratio decreases steadily to the "end". This single growth/decay cycle was characteristic of the individual MCCs, and supports the view that the mature MCC develops an organized meso-α-scale vertical circulation (Maddox, 1980); a system less organized on the meso-α-scale and more dominated by convective-scale circulations might be expected (if it could produce a large contiguous anvil at all) to produce a more pulsating anvil with multiple maxima of cold IR areas during its extended duration.

Just as the -53°C area attains a maximum 1 h prior to the maximum -32°C area in both composites, the "overshooting-top-maximum", with an extensive interior region of cloud-top temperatures considerably colder than -53°C, occurs about 2 h prior to the maximum -53°C area. Thus, to the extent that cloud-top temperatures represent the intensity of vertical motions, there is evidence that the MCC transforms steadily from a relatively small system dominated by intense convective circulations over small individual areas into a larger system of diminishing vertical motions over a larger area.

Fig. 6 depicts the precipitation trend for the composite MCCs in terms of average hourly rain rate, area and volume (R, A, and V, where V=AxR). The graphs indicate that maximum R occurs early in the intense growth phase of the MCC, followed by a steady decrease that tends to level off in the latter decaying stage. The area of measurable rain increases steadily until 1-2 h after the MCC "maximum" and near the -32°C maximum, followed by a steady decrease. The

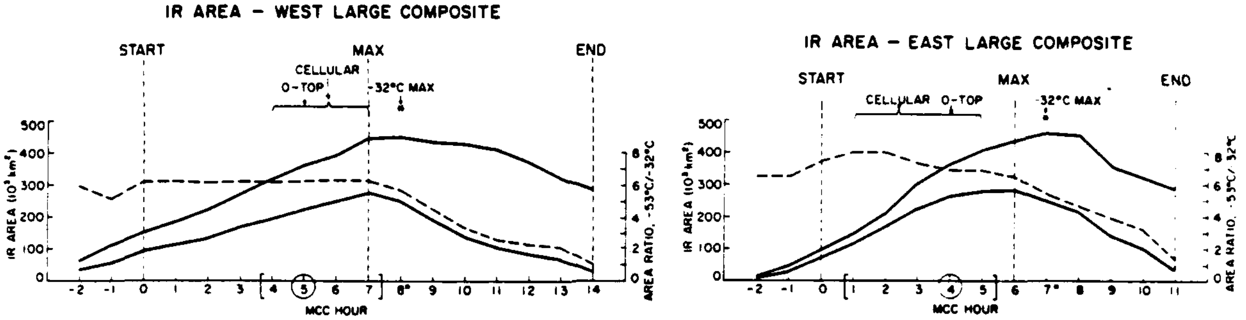

Fig. 5. Trends of composite MCC anvil size, as defined by areas of cloud-top IR temperature colder than -32 and -53°C (upper and lower solid curves, respectively). Ratio of -53 to -32°C areas is given by the dashed line. IR features of the composites are as in Fig. 4.

resultant V maximizes 1-2 h prior to the "maximum", towards the end of the "cellular" stage, and near or shortly after the "overshooting-top maximum". From the quartiles of total accumulated precipitation volume shown in Fig. 4, it can be seen that the peak in V occurs about 1 h prior to the 50% quartile.

The volumes, partitioned between "core" and "peripheral" precipitation, indicate that the great majority of the MCC's rainfall occurs within its "core" (-53°C) region. Note that the maximum rain area, about 12×10^4 km^2 for both large composites, is less than half the maximum -53°C area seen in Fig. 5, indicating that most of the MCC anvil is non-precipitating. It is only during the last few hours, as the -53°C area shrinks to sub-MCC dimensions, that the diminishing rainfall becomes appreciably "peripheral".

A more detailed examination of the average hourly rainfall rates depicted in Fig. 6 was made by deriving frequency distributions of reported rainfall intensities over various intensity categories. This analysis was carried out separately for both types of rain gages used in the hourly precipitation network: those with recording increments of 0.1 in (2.5 mm) and those with higher resolution increments of 0.01 in (0.25 mm). This provided two independent analyses for each composite MCC.

The resulting frequency distributions for the 0.1 in (2.5 mm) gages are illustrated in Fig. 7, where the percentage of measurable reports contributed by each intensity category is represented by the height of the appropriately shaded bar. For the large MCCs, the maximum average rates seen in the early growth stage in Fig. 6 are shown to be due to the relative maximum occurrence of the heavier hourly rates, including reports exceeding 51 mm (2.0 in). For example, the percentages of hourly reports $\geq$ 12.7 mm (0.5 in) reach maxima of 25% at MCC hour 5, and 43% at hour 1, for the W-L and E-L composites, respectively. After these maxima, the decreasing fraction of intense rainfall represents the weakening of the meso-β clusters that built the meso-α complex. The meso-α system nevertheless continues to expand for several more hours, becoming increasingly dominated by the lighter rainfall intensities.

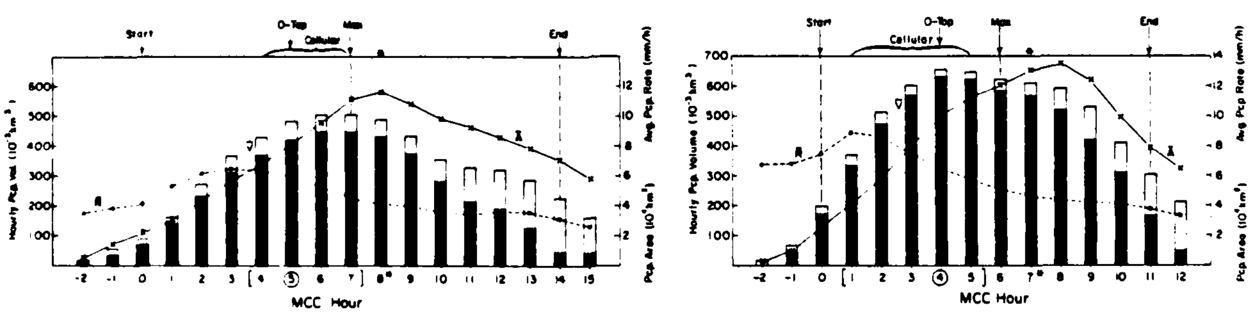

Fig. 6. Trends of composite MCC measurable hourly precipitation area ($\bar{A}$, solid line), average hourly precipitation rate ($\bar{R}$, dashed line) and hourly precipitation volume (V, bars). Precipitation volumes are partitioned between "core" and "peripheral" rainfall (dark and light shaded portions, respectively). 1-2-1 running averages of the individual MCCs' hourly values were used to compute the composite values. Hourly values are plotted at the end of the hour to which they apply. Noted IR features are as in Fig. 4.

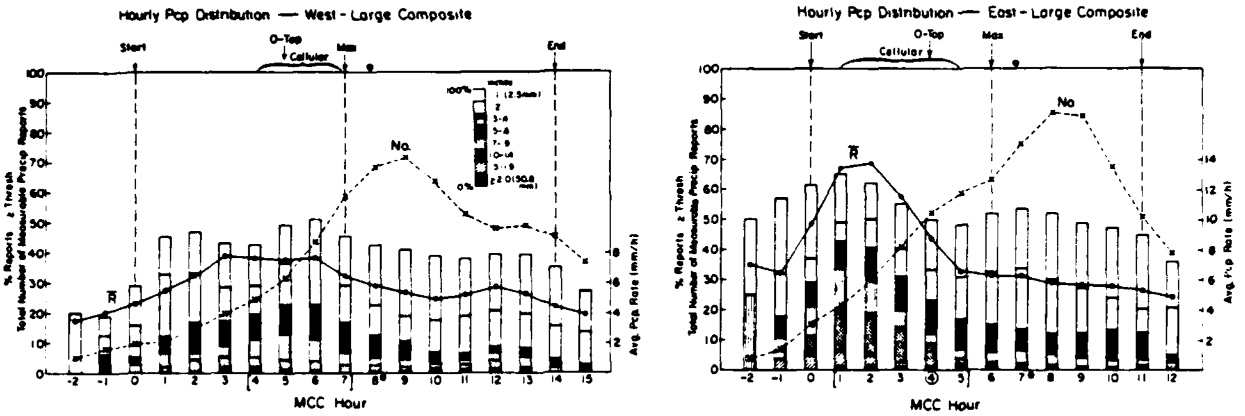

Fig. 7. Trends of composite MCC frequency distributions of measurable hourly precipitation reports over various intensity categories, utilizing raingages with increments of 0.1 inches (2.5 mm). Bars are partitioned into percentages of measurable reports contributed by each intensity category, shaded according to the key inset in the west-large composite. The contribution due to the lightest intensity category (reports of 0.1 inch) is represented by the distance from 100% line down to the top of the partitioned bars. The total sample size for each hour (No.) is the number of measurable reports summed over the three MCCs, and is plotted as the dashed line. The average hourly intensity of these reports (R) is plotted as the solid line. Other details are as in Fig. 6.

A similar frequency distribution analysis was performed utilizing Manually Digitized Radar (MDR) data. These data consist of an array of grid blocks, each about 84 km square, with code values assigned manually by radar observers according to the criteria in Table 2 (Moore et al., 1974). The analysis, shown in Fig. 8, corroborates the findings of the rainfall intensity distribution. For both composites, the relative frequencies of intense "convective" MDR values (code thresholds 6 and 8, representing VIP levels 4 and 5/6, respectively) are high through the initial developing stage of MCC growth, remaining high until or maximizing in the early "cellular" stage. The relative occurrence of these high values decreases thereafter, with an increasing proportion of MDR values less than 6.

Note that the areas of non-zero MDR coverage in Fig. 8, scaled to the number of non-zero blocks, are considerably larger than the hourly rainfall areas in Fig. 6, and are in fact much more comparable to the IR anvil areas in Fig. 5. Thus, while weak echo is distributed over an area on the scale of the meso-α anvil system, much of this light precipitation is lost to subcloud evaporation or falls at a rate less than the hourly measurable threshold.

Table 2: Manually Digitized Radar (MDR) data code

Code No.	Coverage in box	Maximum Reflectivity (dBZ)	Maximum Convective Rainfall Rate (mm/h), Category
0	No echo	N/A	0
1	Any VIP1	< 30	0-5, light
2	≤ 1/2 VIP2	30–40	6-27, moderate
3	> 1/2 VIP2		
4	≤ 1/2 VIP3	41–45	28-55, heavy
5	> 1/2 VIP3		
6	≤ 1/2 VIP3,4	46–49	56-114, very heavy
7	> 1/2 VIP3,4		
8	≤ 1/2 VIP3,4,5,6	50–56 or	115-180, intense or
9	> 1/2 VIP3,4,5,6	> 56	> 180, extreme

From the analyses presented in Figs. 4-8, a fairly clear picture of MCC precipitation evolution emerges for the large MCCs. The maximum relative occurrence of intense rainfall rates near the beginning of the organized "cellular" period and near the "overshooting-top maximum", and their subsequent decrease through the remainder of the "cellular" stage, imply that the intense early convection producing these intense rates is a necessary upscale forcing mechanism of the organized meso-α-scale circulation, which develops as a several-hour response to that forcing. During that response, the MCC is transformed into a larger precipitating system of increasingly lighter and more stratiform anvil rainfall, and then gradually decreases in size as it decays.

A similar evolution (not shown) was found for the small composite MCCs, but was not as well-defined or as representative of the individual systems making the composites. It is believed that this represents an inherent greater variability of these "smaller-scale" and less precipitation-efficient MCCs.

4.0 FORECASTING APPLICATIONS

The relationships between the IR cloud-top features and the concurrent rainfall characteristics of these MCCs are qualitatively consistent with empirical convective rainfall nowcasting techniques that rely on anvil expansion rates, cloud-top temperatures and cloud histories (Scofield and Oliver, 1977; Griffith et al., 1978). Moreover, inasmuch as these composites represent typical MCC life cycles, the relation of the IR

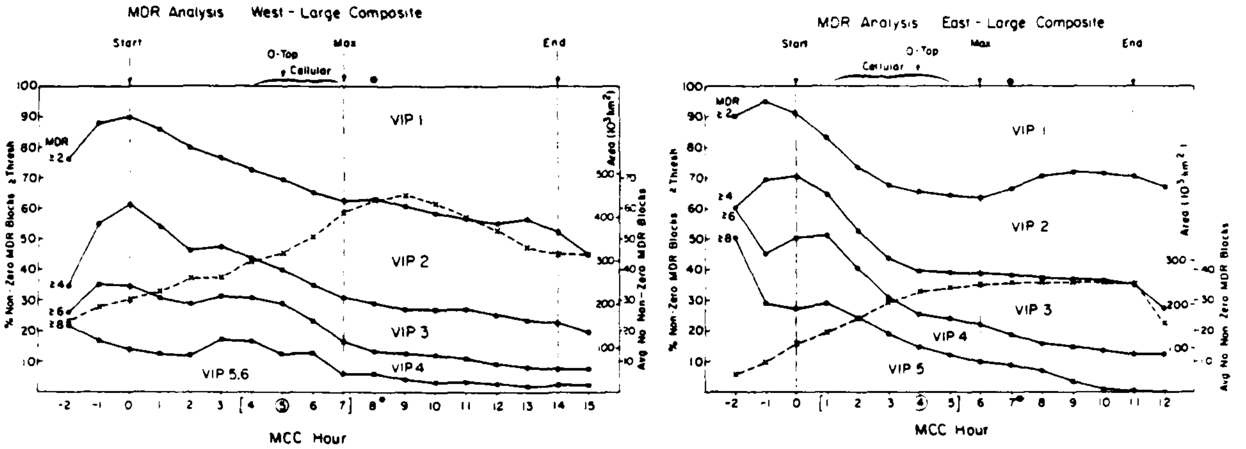

Fig. 8. Trends of composite MCC frequency distributions of non-zero Manually Digitized Radar (MDR) blocks over various intensity categories (Table 2). The dashed line gives the average number of non-zero MDR blocks, which is scaled to areal coverage on the right ordinate. Hourly values, applicable at about 30 min off the hour, are plotted at the end of that hour. The east-large composite includes data for MCC #6 and #9/10 only, as no data were available for MCC #8. Other details are as in Fig. 7.

and precipitation trends in Figs. 4-8 provides a potential tool for forecasting certain aspects of the latter 2/3 of the MCC's life cycle, especially for the "better-behaved" large systems.

For example, the real-time observation via satellite and radar (or raingages) of the formation of a growing, incipient MCC (MCC hour 0) would portend the increase or continuation of intense convective rainfall over the next 2-4 h, and a longer steady increase in both precipitation area and volumetric rainfall rate. Continuing into the life cycle, the observation of a decrease in relative frequency of intense convection within an organized, "cellular" MCC would signal that the system will expand and the "cellular" stage will persist for 2-3 h longer, then will gradually decay. From the standpoint of average precipitation intensity in Fig. 6, such decreasing trends might be reliably established in real time over the period of MCC hours 3 to 5 for the W-L MCC, and hours 1 to 3 for the E-L system. As a hydrological forecasting tool, that determination would permit the projections of maximum volumetric rain rate of the system to occur over the next 1-2 h and active precipitation area to increase over the next 3-5 h. Further precursory indicators of the projected precipitation area maximum would be the observed decrease in volumetric rain rate and the first signs of the IR cloud shield showing weakening in its "overshooting top" intensity (evident by MCC hours 6 and 5, respectively, for the W-L and E-L composites). After a decreasing trend is observed over a 1-2 h period following the maxima in any of the volume, area or average intensity trends, the curves suggest that simple extrapolation techniques could project these trends for several hours through the MCC's dissipation.

Since this analysis has not addressed the complex spatial characteristics of rainfall within the MCC, its application to hydrological forecasting would be most relevant for very large drainage basins.

5.0 DISCUSSION AND CONCLUSIONS

It must be recognized that these generalizations are drawn from an analysis of only a few MCCs occurring in a quasi-steady-state synoptic pattern, and thus may not be representative of MCCs that form under different synoptic conditions, in different geographical regions, or earlier or later in the convective season. For instance, Clark et al. (1980) and Merritt and Fritsch (1984) discussed several classes of organized mesoscale convection that can meet the satellite-defined MCC criteria, but each type was associated with a distinct synoptic pattern which exerted strong controls on the internal organization of the storm. Indeed, this episode's MCCs (McAnelly and Cotton, 1985) and those described by others (Leary and Rappaport, 1983; Rockwood et al., 1984) indicate that there is extreme variability in the internal structure and evolution of MCCs.

Nevertheless, the net result in each case is a long-lived meso-α-scale system that develops from more localized, intense convective forcing. By averaging through the internal complexity of the MCCs, an analysis of hourly precipitation statistics has shown that this evolution is characterized by a well-defined precipitation life-cycle relative to the satellite appearance, especially for the larger MCCs. Average precipitation rates, and the fraction of precipitation due to intense rainfall rates, increase through the initial developmental stage and reach their peak near the time that the MCC attains an organized, meso-α-scale "cellular" appearance. The essential upscale transformation into an intense MCC has thus occurred by this time, which is still early in the life-cycle. During the several-hour intense "cellular" stage, the volumetric rain rate of the MCC reaches a well-defined maximum, which may reflect the maximum intensity of its meso-α-scale circulation. Shortly after this maximum, the MCC reaches its maximum size (-53°C IR area) and loses its organized meso-α-scale "cellular" appearance. Though the active rain area continues to expand a while longer, it is characterized by increasingly lighter rain and is apparently indicative of a prolonged, weakening mesoscale circulation.

This life-cycle resembles closely that discussed by Leary (1984) and generalized by Houze and Betts (1981) for mesoscale precipitation features in the tropical Atlantic. The latter study hypothesized that the strong convective forcing maximizes about a third of the way through the feature's typical 12-h life-cycle, the latter 2/3 being a prolonged mesoscale response. It seems likely that useful hydrological forecasting techniques could be developed on the basis of this extended response to real-time observable events.

A much larger sample of MCCs, screened from several years of MCC climatology (e.g., Rodgers et al., 1985), is currently being analyzed in a similar composite manner. We thus hope to find the quantitative limits of such forecasting techniques, and to quantify the natural variability of the precipitation life-cycle as exhibited by various geographical, seasonal, and size classes of MCCs.

6.0 ACKNOWLEDGEMENTS

Dr. Peter J. Wetzel performed some of the preliminary analysis incorporated into this study. We thank Lucy McCall and Judy Sorbie for their drafting services and Brenda Thompson and Nancy Duprey for processing the manuscript. This research was supported under National Science Foundation Grants #ATM-7908297 and #ATM-8312077, by the National Aeronautics and Space Administration under Contract #NSG-5341, and by the Office of Naval Research under Contract #N00014-83-K-0321. It was also supported in part by the Air Force Office of Scientific Research under AFOSR Grant #82-0162 and by the National Oceanic and Atmospheric Administration under Grant #NA81RAH00001.

7.0 REFERENCES

Clark, J.D., A.J. Lindner, R. Borneman and R.E. Bell, 1980: Satellite observed cloud patterns associated with excessive precipitation outbreaks. Preprints, Eighth Conf. on Weather Forecasting and Analysis, Amer. Meteor. Soc., 28 June - 1 July, Denver, Colorado, 463-473.

Fritsch, J.M., R.A. Maddox and A.G. Barnston, 1981: The character of mesoscale convective complex precipitation and its contribution to warm season rainfall in the U.S. Preprints, Fourth Conf. on Hydrometeorology, Amer. Meteor. Soc., 7-9 October, Reno, Nevada, 94-99.

Fritsch, J.M., and R.A. Maddox, 1981: Convectively driven mesoscale weather systems aloft. Part I: Observations. Part II: Numerical simulations. J. Appl. Meteor., 20, 9-26.

Griffith, C.G., W.L. Woodley, P.G. Grube, D.W. Martin, J. Stout and D.N. Sikdar, 1978: Rain estimation from geosynchronous satellite imagery--Visible and infrared studies. Mon. Wea. Rev., 106, 1153-1171.

Houze, R.A., Jr., and A.K. Betts, 1981: Convection in GATE. Rev. of Geophysics and Space Physics, 19, 541-576.

Leary, C.A., 1984: Precipitation structure of the cloud clusters in a tropical easterly wave. Mon. Wea. Rev., 112, 313-325.

Leary, C.A., and E.N. Rappaport, 1983: Internal structure of a mesoscale convective complex. Preprints, 21st Conf. on Radar Meteorology, Amer. Meteor. Soc., 19-23 September, Edmonton, Alberta, 70-77.

Maddox, R.A, 1980: Mesoscale convective complexes. Bull. Amer. Meteor. Soc., 61, 1374-1387.

Maddox, R.A., 1981: The structure and life-cycle of midlatitude mesoscale convective complexes. Atmospheric Science Paper No. 336, Dept. of Atmospheric Science, Colorado State University, Fort Collins, Colorado, 80523, 311 pp.

McAnelly, R.L., and W.R. Cotton, 1985: Meso-β-scale characteristics of the meso-α-scale convective complex. Submitted for publication to Mon. Wea. Rev..

Merritt, J.H., and J.M. Fritsch, 1984: On the movement of the heavy precipitation areas of mid-latitude mesoscale convective complexes. Preprints, 10th Conf. on Wea. Forecasting and Analysis, Amer. Meteor. Soc., 25-29 June, Clearwater Beach, Florida, 529-536.

Moore, P.L., A.D. Cummings and D.L. Smith, 1974: The National Weather Service Manually Digitized Radar program and its application to precipitation probability forecasting. Preprints, Fifth Conf. on Wea. Forecasting and Anal., Amer. Meteor. Soc., 4-7 March, St. Louis, Missouri, 69-74.

Rockwood, A.A., D.L. Bartels and R.A. Maddox, 1984: Precipitation characteristics of a dual mesoscale convective complex. NOAA Tech. Memo. ERL ESG-6, Dept. of Commerce, National Oceanic and Atmospheric Administration, Environmental Resarch Laboratories, Environmental Sciences Group, Boulder, Colorado, 80303, 50 pp.

Rodgers, D.M., M.J. Magnano and J.H. Arns, 1985: Mesoscale convective complexes over the United States during 1983. Mon. Wea. Rev., 113, 888-901.

Scofield, R.A., and V.J. Oliver, 1977: A scheme for estimating convective rainfall from satellite imagery. NOAA Tech. Memo. NESS 86, U.S. Dept. of Commerce, National Oceanic and Atmospheric Administration, National Environmental Satellite, Data, and Information Service, 47 pp. [NTIS No. PB-270 762/8GI].

Wetzel, P.J., W.R. Cotton and R.L. McAnelly, 1983: A long-lived mesoscale convective complex. Part II: Evolution and structure of the mature complex. Mon. Wea. Rev., 111, 1919-1937.